Studies on Vibronic Coupling in Molecules

Naoya Iwahara

2012

Preface

Vibronic coupling or electron-vibration coupling is intrinsic to molecules and solids. The vibronic coupling has been considered to play an important role in many phenomena such as, for instance, the Jahn–Teller effect, absorption and emission spectra, superconductivity, chemical reaction, and so on. Therefore the vibronic coupling have been investigated extensively in molecules and solids. In this thesis, the author concentrates on the vibronic couplings in molecules.

In order to discuss the vibronic couplings in concrete systems, we must know the vibronic coupling constants. However, in many systems, the vibronic coupling constants have not been precisely determined. Sometimes several couplings have been proposed for one system. For example, fullerene (C_{60}) is one of such systems. Thereby it is desired to establish robust theoretical method to derive the vibronic coupling constants. The vibronic coupling density obtained from the electronic and vibrational structures has been proposed as a useful concept to explain the vibronic coupling. The vibronic coupling density gives us a local picture of the vibronic couplings, which allows us to control the vibronic couplings more easily.

This thesis aims to develop the theory of the vibronic coupling and to apply the theory to several molecules. In part I, two fundamental problems in the Jahn–Teller effect, the origin of the Jahn–Teller distortion and the isotope effect on the Jahn–Teller system, are studied. In part II, the vibronic coupling constants of C_{60}^{-} and C_{60} derivatives are evaluated and analyzed in terms of the vibronic coupling density. The vibronic coupling density of C_{60} for the reaction mode is proposed as a chemical reactivity index. In part III, from the view point of the vibronic coupling, several properties of molecules are discussed.

The author hopes that present thesis will contribute to development of the theory to deal with the vibronic couplings in molecules and solids.

Acknowledgments

The present thesis is the summary of the author's studies from 2006 to 2012 at the Department of Molecular Engineering, Graduate School of Engineering, Kyoto University.

The author would like to express his deepest gratitude to Professor Kazuyoshi Tanaka for his valuable comments and continuous encouragement throughout his studies. The author is also extremely grateful to Associate Professor Tohru Sato for his indispensable suggestions and discussions.

The author would like to thank Associate Professor Liviu F. Chibotaru (Katholieke Universiteit Leuven) for his kind advice and fruitful discussions in their collaborations. He wish to thank Professor Arnout Ceulemans (Katholieke Universiteit Leuven) for suggesting the study on the origin of the Jahn–Teller distortion. He is grateful to Professor Tsunehiro Tanaka (Kyoto University) for useful discussion on photocatalysis. He is thankful to Professor Hironori Kaji (Kyoto University) for helpful discussion on the fullerene derivatives in organic photovoltaics. It is pleasure to thank Professor Tatsuhisa Kato (Kyoto University) for his useful comments on the isotope effect. He would like to thank Professor Lai-Sheng Wang and Dr. Xue-Bin Wang (Washington State University) for sending us unpublished data. The author is grateful to Associate Professor Akihiro Ito and Mr. Daisuke Sakamaki (Kyoto University) for fruitful discussion on organic high-spin molecules. The author wishes to thank the Division of Quantum and Physical Chemistry at the Katholieke Universiteit Leuven for hospitality during his stay there.

Dr. Hiroyuki Fueno is sincerely acknowledged for his kind advice. The author wishes to express his acknowledge to the members of Associate Professor Sato's research group, Dr. Ken Tokunaga (Kogakuin University), Dr. Katsuyuki Shizu (Kyushu University), Dr. Guo Wang, Mr. Motoyuki Uejima, Mr. Kazuaki Kamiya, Mr. Keisuke Uegaito, Mr. Tomoharu Arai, Mr. Naoki Haruta, Mr. Kota Usui, and Mr. Takanobu Mimura for their kindness and valuable supports. He would like to thank other members of Tanaka Laboratory, and the secretaries, Ms. Yuko Otsuki, Ms. Ayako Tanaka, and Ms. Miya Kitao.

The author would like to thank the financial support by Grant-in-Aid for the Global COE Program, "International Center for Integrated Research and Advanced Education in Materials Science," from the Ministry of Education, Culture, Sports, Science and Technology of Japan. He would like to acknowledge the research fund for study abroad from the

Research Project of Nano Frontier, graduate school of engineering, Kyoto University. He would also like to acknowledge the financial support from Katholieke Universiteit Leuven for his research in Leuven.

Finally, the author would like to sincerely thank his parents, Juichi Iwahara and Setsue Iwahara, his sister, Mari Iwahara, and his brother, Kazuki Iwahara for their understanding, kindness, and support.

Kyoto, January 2012

Naoya Iwahara

List of Publications

Part I

Chapter 1

(1) "Origin of the Jahn-Teller distortions: Vibronic coupling density analysis for Jahn-Teller molecules",
T. Sato, K. Shizu, N. Iwahara, N. Haruta, and K. Tanaka, in preparation.

Chapter 2

(2) "Kinetic localization of the isotope substituted Jahn–Teller system",
N. Iwahara, T. Sato, K. Tanaka, and L. F. Chibotaru, in preparation.

Part II

Chapter 1

(3) "Vibronic coupling in C_{60}^{-} anion revisited: Precise derivations from photoelectron spectra and DFT calculations",
N. Iwahara, T. Sato, K. Tanaka, and L. F. Chibotaru, Phys. Rev. B **82**, 245409 1-10 (2010); (4) "Estimation of the vibronic coupling constants of fullerene monoanion: Comparison between experimental and simulated results",
N. Iwahara, T. Sato, K. Tanaka, and L. F. Chibotaru,
in: M. Atanasov, C. Daul, and P. L. W. Tregenna-Piggott (Eds.), Vibronic Interactions and the Jahn-Teller Effect: Theory and Applications, Springer-Verlag, Berlin, 2011.

Chapter 2

(5) "Effect of Coulomb interactions on the vibronic couplings in C_{60}^{-}",
N. Iwahara, T. Sato, and K. Tanaka, submitted.

Chapter 3

(6) "C_{60} bearing ethylene moieties",
T. Sato, N. Iwahara, N. Haruta, and K. Tanaka, submitted.

Chapter 4

(7) "Vibronic couplings in C_{60} derivatives for organic photovoltaics",
T. Sato, N. Iwahara, K. Tanaka, H. Kaji, in preparation.

Part III

Chapter 1

(8) "Active center induced by vibronic interactions in V_2O_5/SiO_2",
T. Sato, N. Iwahara, K. Tokunaga, K. Tanaka, and T. Tanaka, Top. Catal. **52**, 808-812 (2009).

Chapter 2

(9) "Molecular design for high-spin molecules in view of vibronic couplings",
N. Iwahara, T. Sato, and K. Tanaka, Polyhedron **30**, 3048-3053 (2011).

Chapter 3

(10) "Critical reinvestigation on vibronic couplings in picene from view of vibronic coupling density analysis",
T. Sato, N. Iwahara, and K. Tanaka, submitted.

The following publications are not included in this thesis.

(11) "Vibronic coupling constant and vibronic coupling density",
T. Sato, K. Tokunaga, N. Iwahara, K. Shizu, K. Tanaka,
in: H. Köppel, D.R. Yarkony, and H. Barentzen (Eds.), The Jahn–Teller-Effect–Fundamentals and Implications for Physics and Chemistry, Springer-Verlag, Berlin and Heidelberg, 2009.

(12) "Vibronic interactions in hole-transporting molecules:
An interplay with electron-hole interactions",
T. Sato, K. Shizu, K. Uegaito, N. Iwahara, K. Tanaka, and H. Kaji, Chem. Phys. Lett. **507**, 151-156 (2011).

Contents

General Introduction

0.1 Vibronic couplings in molecules

The vibronic (electron-vibration) coupling or electron-phonon coupling is one of the fundamental couplings in molecules and solids, and it plays an important role in the Jahn–Teller effect, absorption and emission spectra, charge transport, superconductivity, ferroelectricity, chemical reaction, and so on [1–7]. Therefore, insight into the vibronic couplings is crucial to understand these phenomena. The aim of this thesis is to develop the theory of vibronic coupling in molecules and to apply the vibronic coupling to several systems.

In this section, we introduce the vibronic coupling and vibronic Hamiltonian. The molecular Hamiltonian is written as

$$\mathcal{H} = \mathcal{T}_{\mathrm{n}}(\mathbf{Q}) + \mathcal{H}_{\mathrm{e}}(\mathbf{r}, \mathbf{Q}), \tag{1}$$

$$\mathcal{H}_{\mathrm{e}}(\mathbf{r}, \mathbf{Q}) = \mathcal{T}_{\mathrm{e}}(\mathbf{r}) + \mathcal{U}_{\mathrm{ee}}(\mathbf{r}) + \mathcal{U}_{\mathrm{en}}(\mathbf{r}, \mathbf{Q}) + \mathcal{U}_{\mathrm{nn}}(\mathbf{Q}), \tag{2}$$

where $\mathbf{r}$ is a set of electronic coordinates, $\mathbf{Q}$ a set of nuclear coordinates, $\mathcal{T}_{\mathrm{n}}$ the nuclear kinetic energy, $\mathcal{T}_{\mathrm{e}}$ the electronic kinetic energy, $\mathcal{U}_{\mathrm{ee}}$ the Coulomb interaction between electrons, $\mathcal{U}_{\mathrm{en}}$ the Coulomb interaction between electrons and nuclei, and $\mathcal{U}_{\mathrm{nn}}$ the Coulomb interaction between nuclei. In this thesis, we choose a closed-shell system with the equilibrium geometry as the reference system [8]. For the nuclear coordinates $\mathbf{Q}$, the mass-weighted normal coordinates of the reference system is used. The origin of the normal coordinates $\mathbf{Q} = \mathbf{0}$ indicates the equilibrium geometry of the reference system. Expanding the electronic Hamiltonian (2) with respect to the normal coordinates $\mathbf{Q}$ around the reference geometry $\mathbf{Q} = \mathbf{0}$ up to the second order, we obtain

$$\mathcal{H}_{\mathrm{e}}(\mathbf{r}, \mathbf{Q}) = \mathcal{H}_{\mathrm{e}}(\mathbf{r}, \mathbf{0}) + \sum_{i\Gamma\gamma} \mathcal{V}_{i\Gamma\gamma} Q_{i\Gamma\gamma} + \frac{1}{2} \sum_{i\Gamma'\gamma' j\Gamma''\gamma''} \mathcal{W}_{i\Gamma'\gamma' j\Gamma''\gamma''} Q_{i\Gamma'\gamma'} Q_{j\Gamma''\gamma''}, \tag{3}$$

where Γ is an irreducible representation of the point group of the reference system G, γ is a row of Γ, and i distinguishes the $\Gamma\gamma$ modes with different frequencies. The second

and the third terms in the right hand side are called the linear and the quadratic vibronic couplings, respectively [1–3, 8]. The electronic parts of the vibronic couplings, $\mathcal{V}_{i\Gamma\gamma}$ and $\mathcal{W}_{i\Gamma'\gamma'j\Gamma''\gamma''}$, are defined by

$$\mathcal{V}_{i\Gamma\gamma} = \left(\frac{\partial \mathcal{H}_{\rm e}(\mathbf{r},\mathbf{Q})}{\partial Q_{i\Gamma\gamma}}\right)_0, \tag{4}$$

$$\mathcal{W}_{i\Gamma'\gamma'j\Gamma''\gamma''} = \left(\frac{\partial^2 \mathcal{H}_{\rm e}(\mathbf{r},\mathbf{Q})}{\partial Q_{i\Gamma'\gamma'}\partial Q_{j\Gamma''\gamma''}}\right)_0. \tag{5}$$

The representations are assumed to be real. Since $\Gamma' \otimes \Gamma''$ is reducible in general, the electronic and vibrational parts of the quadratic terms can be symmetrized [1, 8].

$$\{\mathcal{W}_{i\Gamma' j\Gamma''}\}_{\Gamma\gamma} = \sum_{\Gamma'\gamma'\Gamma''\gamma''} \mathcal{W}_{i\Gamma'\gamma' j\Gamma''\gamma''} \langle \Gamma'\gamma'\Gamma''\gamma''|\Gamma\gamma\rangle, \tag{6}$$

$$\{Q_{i\Gamma'} \otimes Q_{j\Gamma''}\}_{\Gamma\gamma} = \sum_{\Gamma'\gamma'\Gamma''\gamma''} Q_{i\Gamma'\gamma'} Q_{j\Gamma''\gamma''} \langle \Gamma'\gamma'\Gamma''\gamma''|\Gamma\gamma\rangle, \tag{7}$$

where $\langle \Gamma'\gamma'\Gamma''\gamma''|\Gamma\gamma\rangle$ is a Clebsch–Gordan coefficient of G [9]. We assume that each irreducible representation Γ does not appear more than once in $\Gamma' \otimes \Gamma''$. Substituting Eqs. (6) and (7) into Eq. (3), we obtain

$$\mathcal{H}_{\rm e}(\mathbf{r},\mathbf{Q}) = \mathcal{H}_{\rm e}(\mathbf{r},\mathbf{0}) + \sum_{i\Gamma\gamma} \mathcal{V}_{i\Gamma\gamma} Q_{i\Gamma\gamma} + \frac{1}{2} \sum_{i\Gamma' j\Gamma''} \sum_{\Gamma\gamma} \{\mathcal{W}_{i\Gamma' j\Gamma''}\}_{\Gamma\gamma} \{Q_{i\Gamma'} \otimes Q_{j\Gamma''}\}_{\Gamma\gamma}. \tag{8}$$

Hereafter, Eq. (8) is used as the electronic Hamiltonian $\mathcal{H}_{\rm e}$ in the molecular Hamiltonian $\mathcal{H}$ (1).

The eigenstates of the molecular Hamiltonian (1), which are called vibronic states, are written by using the crude adiabatic approximation [6, 8, 10]. Within the crude adiabatic approximation, the set of the electronic eigenstates $\{|\psi_{\alpha\Gamma\gamma}\rangle\}$ of $\mathcal{H}_{\rm e}(\mathbf{r},\mathbf{0})$ is used as the basis set of the total wavefunction, which gives the relationship

$$\mathcal{H}_{\rm e}(\mathbf{r},\mathbf{0})|\psi_{\alpha\Gamma\gamma}\rangle = E_{\alpha\Gamma}|\psi_{\alpha\Gamma\gamma}\rangle, \tag{9}$$

where α distinguishes the $\Gamma\gamma$ electronic states. The vibronic states are represented by

$$|\Psi_{\mu\Lambda\lambda}\rangle = \sum_{\alpha\Gamma\gamma} |\psi_{\alpha\Gamma\gamma}\rangle |\chi^{\mu\Lambda\lambda}_{\alpha\Gamma\gamma}\rangle, \tag{10}$$

where Λ is an irreducible representation, λ is a row of the representation Λ, and μ distinguishes the $\Lambda\lambda$ states.

The Hamiltonian matrix with the electronic basis set $\{|\psi_{\alpha\Gamma\gamma}\rangle\}$ is expressed by

$$\begin{aligned}\left(\hat{H}\right)_{mn} &= E_m\delta_{mn} + T_{\rm n}(\mathbf{Q})\delta_{mn} + \sum_{i\Gamma\gamma} \left(\mathcal{V}_{i\Gamma\gamma}\right)_{mn} Q_{i\Gamma\gamma} \\ &+ \frac{1}{2} \sum_{i\Gamma' j\Gamma''} \sum_{\Gamma\gamma} \left(\{\mathcal{W}_{i\Gamma' j\Gamma''}\}_{\Gamma\gamma}\right)_{mn} \{Q_{i\Gamma'} \otimes Q_{j\Gamma''}\}_{\Gamma\gamma},\end{aligned} \tag{11}$$

where the electronic states $\alpha\Gamma\gamma$ are replaced by m, n for simplicity, $(\mathcal{V}_{i\Gamma\gamma})_{mn} = \langle\psi_m|\mathcal{V}_{i\Gamma\gamma}|\psi_n\rangle$ are the linear vibronic coupling constants (VCC), and $(\{\mathcal{W}_{i\Gamma' j\Gamma''}\}_{\Gamma\gamma})_{mn} = \langle\psi_m|\{\mathcal{W}_{i\Gamma' j\Gamma''}\}_{\Gamma\gamma}|\psi_n\rangle$ are the quadratic VCCs. The Hamiltonian matrix (11) does not have nonadiabatic terms which appear in the Born–Oppenheimer or Born–Huang approximations [6, 8, 10]. Moreover, the potential terms are written by simple polynomials of the normal coordinates. Therefore, physical meaning of each term in the Hamiltonian matrix (11) is clear and the Hamiltonian matrix is suitable for analytical treatment.

From the selection rule [9], we obtain the modes with nonzero vibronic couplings. When the electronic states $m = (\alpha\Gamma\gamma)$ and $n = (\beta\Gamma'\gamma')$ belong to different eigenenergies, the vibrational modes whose irreducible representations are included in the direct product $\Gamma \otimes \Gamma'$ are active. If the eigenstates m, n belong to the same eigenenergy ($m = (\alpha\Gamma\gamma)$, $n = (\alpha\Gamma\gamma')$), the electronic state couples to the modes whose irreducible representations are included in the symmetric product $[\Gamma^2]$. Applying the Wigner–Eckart theorem [9] to the vibronic coupling constants,

$$\left\langle \psi_{\alpha\Gamma\gamma} \left| \mathcal{V}_{i\bar{\Gamma}\bar{\gamma}} \right| \psi_{\beta\Gamma'\gamma'} \right\rangle = V_{i\bar{\Gamma}}^{\alpha\Gamma\beta\Gamma'} \langle \Gamma\gamma | \bar{\Gamma}\bar{\gamma}\Gamma'\gamma' \rangle, \tag{12}$$

$$\left\langle \psi_{\alpha\Gamma\gamma} \left| \{\mathcal{W}_{i\Gamma_1 j\Gamma_2}\}_{\bar{\Gamma}\bar{\gamma}} \right| \psi_{\beta\Gamma'\gamma'} \right\rangle = W_{ij\bar{\Gamma}}^{\alpha\Gamma\beta\Gamma'} \langle \Gamma\gamma | \bar{\Gamma}\bar{\gamma}\Gamma'\gamma' \rangle, \tag{13}$$

where $\bar{\Gamma}$ is an irreducible representation, and $\bar{\gamma}$ is a row of $\bar{\Gamma}$.

Next, the electronic eigenenergy of interest is assumed to be separated from other ones. For a nondegenerate electronic state $|\psi_{\alpha\Gamma}\rangle$, all of the totally symmetric modes are active. Thereby, the vibronic Hamiltonian is given by

$$\hat{H} = E_{\alpha\Gamma} + \sum_{i\bar{\Gamma}\bar{\gamma}} \frac{1}{2} \left(P_{i\bar{\Gamma}\bar{\gamma}}^2 + \omega_{i\bar{\Gamma}}^2 Q_{i\bar{\Gamma}\bar{\gamma}}^2 \right) + \sum_i V_{iA} Q_{iA}, \tag{14}$$

where the linear VCC $V_{iA}^{\alpha\Gamma}$ is expressed by V_{iA}, A indicates the totally symmetric representation, cross terms of the quadratic couplings are neglected, and $\omega_{i\bar{\Gamma}}^2 = W_{ii\bar{\Gamma}}^{\alpha\Gamma\alpha\Gamma}$. Eq. (14) is the Hamiltonian for the displaced oscillators.

For a degenerate electronic state $|\psi_{\alpha\Gamma\gamma}\rangle$, the vibronic Hamiltonian becomes

$$\begin{aligned} \hat{H} &= \left[E_{\alpha\Gamma} + \sum_{i\bar{\Gamma}\bar{\gamma}} \frac{1}{2} \left(P_{i\bar{\Gamma}\bar{\gamma}}^2 + \omega_{i\bar{\Gamma}}^2 Q_{i\bar{\Gamma}\bar{\gamma}}^2 \right) \right] \hat{C}_0 \\ &+ \sum_{i\bar{\Gamma}\bar{\gamma}} V_{i\bar{\Gamma}} Q_{i\bar{\Gamma}\bar{\gamma}} \hat{C}_{\bar{\Gamma}\bar{\gamma}} + \sum_{i\Gamma_1 j\Gamma_2} \sum_{\bar{\Gamma}\bar{\gamma}\neq A} W_{ij\bar{\Gamma}} \{ Q_{i\Gamma_1\gamma_1} \otimes Q_{j\Gamma_2\gamma_2} \}_{\bar{\Gamma}\bar{\gamma}} \hat{C}_{\bar{\Gamma}\bar{\gamma}}, \end{aligned} \tag{15}$$

where $\hat{C}_0 = \sum_\gamma |\psi_{\alpha\Gamma\gamma}\rangle\langle\psi_{\alpha\Gamma\gamma}|$ is the unit matrix, and $\hat{C}_{\bar{\Gamma}\bar{\gamma}}$ is the matrix whose elements

are the Clebsch–Gordan coefficients $\langle \Gamma\gamma | \bar{\Gamma}\bar{\gamma}\Gamma\gamma' \rangle$. This Hamiltonian is the starting point to discuss the Jahn–Teller effect.

0.2 The Jahn–Teller effect

In 1937, H. A. Jahn and E. Teller proved a theorem on the instability of the degenerate system (Jahn–Teller theorem) [11]:

> All non-linear nuclear configurations are therefore unstable for an orbitally degenerate electronic state.

More rigorous theorem is given elsewhere [1–3]. If the Jahn–Teller theorem is fulfilled, the system distorts and is stabilized. This distortion reduces the symmetry of the system and the degeneracy of the electronic state is lost. This phenomenon is called the Jahn–Teller effect.

As an example, we discuss a system with C_{3v} or D_{3h} symmetry. The electronic state is assumed to be doubly degenerate E. From the selection rule, the system couples to totally symmetric a_1 modes and doubly degenerate e modes. If the system has one e mode and does not have the couplings to the a_1 modes, the system is called $E \otimes e$ Jahn–Teller system [1, 3, 8]. The $E \otimes e$ Jahn–Teller Hamiltonian is written as

$$\hat{H} = \sum_{\gamma=\theta,\epsilon} \frac{1}{2}\left(P_\gamma^2 + \omega_E^2 Q_\gamma^2\right)\hat{\sigma}_0 + V_E \begin{pmatrix} Q_\theta & Q_\epsilon \\ Q_\epsilon & -Q_\theta \end{pmatrix} + W_E \begin{pmatrix} Q_\theta^2 - Q_\epsilon^2 & -2Q_\theta Q_\epsilon \\ -2Q_\theta Q_\epsilon & -(Q_\theta^2 - Q_\epsilon^2) \end{pmatrix} \quad (16)$$

where $\hat{\sigma}_0$ is the 2×2 unit matrix, and the electronic eigenenergy $E_{\alpha\Gamma}$ in Eq. (15) is removed since it is a constant.

The adiabatic potential energy surface clearly shows the reason of the instability of the degenerate system with high symmetry. The potential energy surface is obtained by diagonalizing the potential term of Eq. (16). Figure 1 shows the potential energy surface without the quadratic vibronic coupling, that is, with $W_E = 0$. This potential has a conical intersection at the origin of the coordinates where the symmetry of the system is high and consists of a one-dimensional trough in the lower sheet. Therefore, the system is not stable at the origin and has a distorted structure around the trough. The symmetry of the distorted structure is lower than that of the reference geometry $\mathbf{Q} = \mathbf{0}$. The gap between the conical intersection and the minima $E_{\mathrm{JT}} = V_E^2/(2\omega_E^2)$ (Fig. 1) is called

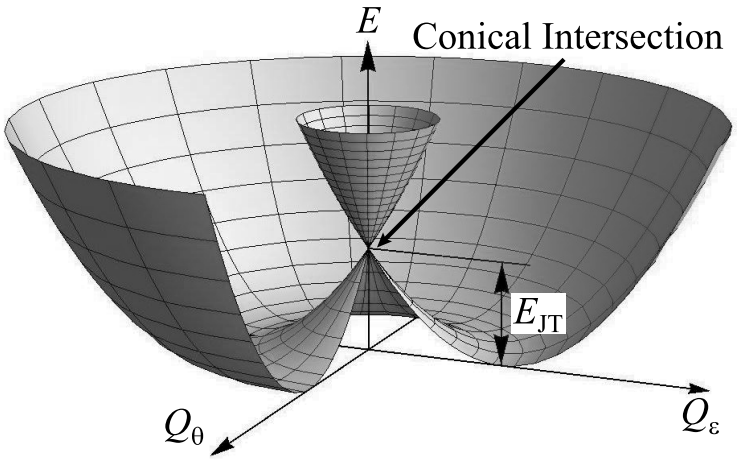

Figure 1: The adiabatic potential energy surface of the linear $E \otimes e$ Jahn–Teller system.

the Jahn–Teller stabilization energy. This distortion is generally called the Jahn–Teller distortion.

Figures 2(a) and (b) show the potential energy surface and contour of the lower sheet with finite W_E, respectively. The quadratic coupling generates the warping of the potential energy surface. The lower surface has three minima separated by saddle around the conical intersection (Fig. 2 (b)). With sufficiently large quadratic coupling, the system is localized at one of the three minima.

The Jahn–Teller distortion gives rise to the orbital mixing, which is caused by the off-diagonal vibronic couplings between these orbitals. The change of the orbital accompanied by the Jahn–Teller distortion is a key in the photoactivation process of a photocatalyst, V_2O_5/SiO_2. The study on the V_2O_5/SiO_2 is presented in chapter 1 in Part III.

Next, we take into account the kinetic energy in Eq. (16) (dynamic Jahn–Teller effect) and discuss the vibronic state (10). The vibronic state is governed by the structure of the adiabatic potential energy surface [1, 3]. Especially, existence of the conical intersection plays a crucial role in the dynamic Jahn–Teller problem. Longuet-Higgins *et al.* noted that the phase factor of the electronic wavefunction changes by π due to an adiabatic rotation around the conical intersection [12–14]. In order to keep the singlevaluedness of the vibronic state, the vibrational part also has to change the sign to cancel the phase change of the electronic part. This phase change turns out to be an example of the Berry phase [15] which appears in various areas and characterizes the phenomena [16]. Ham has established manifestation of the Berry phase in the Jahn–Teller effect [17]. With the

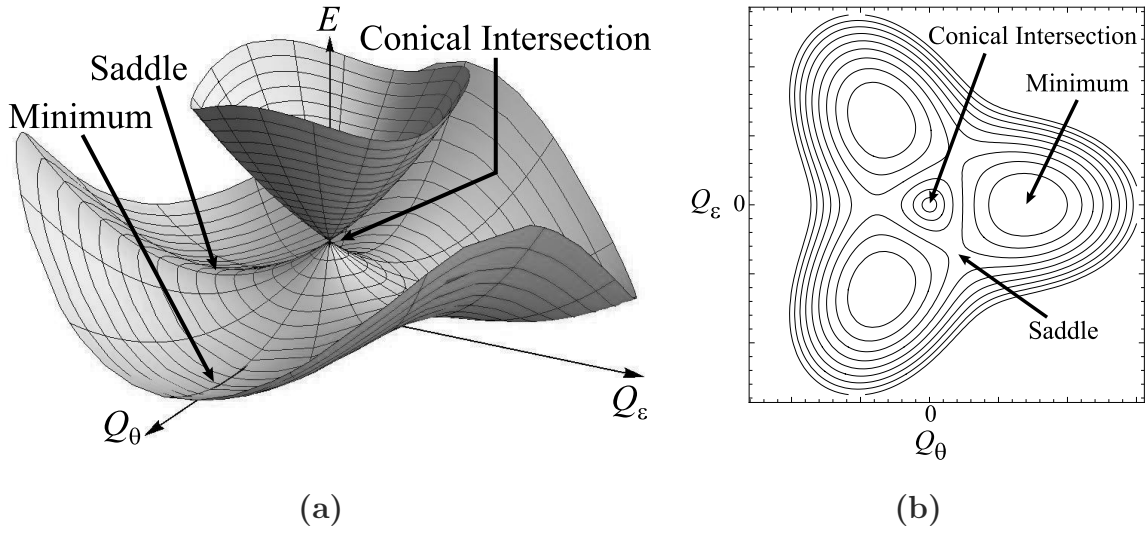

Figure 2: (a) Adiabatic potential energy surface of the quadratic $E \otimes e$ Jahn–Teller system. (b) Contour plot of the lower-sheet of the adiabatic potential energy surface of the quadratic $E \otimes e$ Jahn–Teller system.

Berry phase, the order of the vibronic levels of the $E \otimes e$ Jahn–Teller system is given as follows:

$$E, A_{1(2)}, A_{2(1)}, E, E, \cdots , \tag{17}$$

where A_1, A_2, and E are the irreducible representations. On the other hand, if the Berry phase is ignored, the order of the representations of the vibronic levels is given by

$$A_1, E, A_{1(2)}, A_{2(1)}, E, E, \cdots . \tag{18}$$

The role of the conical intersection or Berry phase in various Jahn–Teller systems has been extensively studied [18–22]. One of the purposes of this thesis is to give a new insight into the dynamics around the conical intersection.

From this point of view, isotope effect of the Jahn–Teller system is an interesting problem because the isotopic substitution retains the degeneracy of the electronic state. Due to the isotopic substitution, the kinetic energy should change, while the potential term does not. Therefore, as in the case of the original Jahn–Teller system, the isotopomer has a one-dimensional trough. The isotope-substituted system is regarded as a generalized Jahn–Teller system. Experimentally, isotope substituted system has been investigated by several authors [23–29]. The isotope effect has been discussed based on a preferred Jahn–Teller distortion in terms of the change in the zero-point energy. However, the origin of

such a distortion has not been revealed completely. Moreover, manifestation of the conical intersection in the isotope effect has not been fully understood hitherto. The isotope effect on the $E \otimes e$ Jahn–Teller system is analyzed and discussed in detail in chapter 2 in Part I.

0.3 Vibronic coupling density

Origin of the Jahn–Teller distortion is still an important topic in the Jahn–Teller effect [30, 31]. One naive explanation on the origin of the Jahn–Teller effect is given on the basis of the on-site Mulliken charge. In the case of a triangular molecule X_3, it seems possible to explain the Jahn–Teller distortion using the on-site charge because of the asymmetric distribution of the Mulliken charge. However, in the case of a cubic molecule X_8^+, the distribution of charge is symmetric and it is impossible to discuss the Jahn–Teller distortion based on the repulsion between on-site charge [30].

In order to reveal the origin of the Jahn–Teller distortion, the concept of the vibronic coupling density (VCD) [8, 32] is useful. First, we consider a diagonal element of vibronic coupling constants, $V_\alpha = \langle \psi_m | \mathcal{V}_\alpha | \psi_m \rangle$, where $\mathcal{V}_\alpha$ is the electronic part of the linear vibronic coupling operator (4), and $i\Gamma\gamma$ in Eq. (4) is replaced by α for simplicity. Integration of the VCD η_α over three-dimensional space $\mathbf{x}$ gives the vibronic coupling constant (VCC) V_α.

$$V_\alpha = \int d\mathbf{x} \eta_\alpha(\mathbf{x}). \tag{19}$$

The VCD η_α is given by the product of the electron density difference $\Delta\rho$ and the potential derivative v_α:

$$\eta_\alpha(\mathbf{x}) = \Delta\rho(\mathbf{x}) \times v_\alpha(\mathbf{x}), \tag{20}$$

where $\Delta\rho$ is defined by the difference between the electron densities of the system ρ and the reference system ρ_0,

$$\Delta\rho(\mathbf{x}) = \rho(\mathbf{x}) - \rho_0(\mathbf{x}), \tag{21}$$

and v_α by the derivative of the one-electron Coulomb potential $u(\mathbf{x}, \mathbf{Q})$ between an electron at $\mathbf{x}$ and all the nuclei at $\mathbf{Q}$ in the molecule with respect to the normal coordinate

Q_α,

$$v_\alpha(\mathbf{x}) \;=\; \left(\frac{\partial u(\mathbf{x},\mathbf{Q})}{\partial Q_\alpha}\right)_0. \tag{22}$$

The vibronic coupling density for an off-diagonal vibronic coupling, $V_\alpha = \langle\psi_{i\Gamma\gamma}|\mathcal{V}_\alpha|\psi_{i\Gamma\gamma'}\rangle$, is given by

$$\eta_\alpha(\mathbf{x}) \;=\; \rho_{\gamma\gamma'}(\mathbf{x}) \times v_\alpha(\mathbf{x}). \tag{23}$$

The overlap density $\rho_{\gamma\gamma'}$ is written as follows:

$$\rho_{\gamma\gamma'}(\mathbf{x}) \;=\; N \sum_{\sigma_1\cdots\sigma_N} \int d\mathbf{r}_2 \cdots d\mathbf{r}_N \psi_{i\Gamma\gamma}(\mathbf{x}\sigma_1, \mathbf{r}_2\sigma_2, \cdots \mathbf{r}_N\sigma_N)\psi_{i\Gamma\gamma'}(\mathbf{x}\sigma_1, \mathbf{r}_2\sigma_2, \cdots \mathbf{r}_N\sigma_N) \tag{24}$$

where N is the number of electrons in the molecule, $\mathbf{r}_i$ the coordinate of ith electron, σ the z component of the electron spin, and $\psi_{i\Gamma\gamma}(\mathbf{x}\sigma_1, \mathbf{r}_2\sigma_2, \cdots \mathbf{r}_N\sigma_N)$ the electronic wavefunction. Since the VCD is calculated from the electronic and vibrational structures, the VCD gives a local picture of the vibronic coupling, which enables us to discuss the origin or the strength of the vibronic couplings. Sato *et al.* have analyzed the vibronic couplings in hole-transporting materials of organic light-emitting device [33–36] and succeeded to design novel hole- or electron-transporting materials [37,38]. One of the aims in this thesis is to deepen the understandings of the physics of the vibronic couplings using the VCD.

The VCD analysis of Li_3 and Li_8^+ is presented in chapter 1 in Part I. The VCD analysis is also employed to explain the order of the vibronic couplings in C_{60}^- (chapter 2 in Part II), C_{60} derivatives used as electron-transporting materials of organic photovoltaic cells (chapter 4 in Part II), and picene anion (chapter 3 in Part III). The VCD is used to design high-spin organic amines in chapter 2 in Part III.

Moreover, based on the theory of Parr and Yang [39], Sato *et al.* has proposed the VCD for the reaction mode as a chemical reactivity index [8,32]. Application of the VCD for Diels–Alder reactions of C_{60} is presented in chapter 3 in Part II.

0.4 Vibronic couplings in C_{60}

Fullerene (C_{60}) is an interesting system in molecular science since it has the highest point group symmetry, I_h. In addition, C_{60} has been paid to much attention because of its various electronic properties, for instance, superconductivity and insulating property of

the alkali-doped fullerides [40–44], ferromagnetism of tetrakis(dimethylamine)ethylene-C_{60} [45]. Particularly, in connection with the electronic properties of the alkali-doped fullerides, the vibronic coupling constants (VCC) or electron-phonon couplings [46] in C_{60}^- anion has been intensively investigated. However, disagreement between the theoretical and experimental works have been pointed out.

The first work on the vibronic couplings of C_{60}^- was published by Varma *et al.* in 1991 [47], in which, they found that the electron-phonon couplings for the stretching $h_g(7)$ and $h_g(8)$ modes are strong, while that for the bending $h_g(2)$ mode weak. This order agrees with many theoretical results [48–52]. In 1995, Gunnarsson *et al.* evaluated the coupling constants from the photoelectron spectrum [53]. Contrary to many works described above, they concluded that the $h_g(2)$ mode has the largest electron-phonon coupling. This result has been supported by some theoretical calculations [54] and derivation from the experimental data [55, 56]. Moreover, the Jahn–Teller stabilization energy depends on the individual methods. The theoretical values are in the range of 33.6 meV to 51.0 meV. On the other hand, Gunnarsson's experimental value is 88.2 meV. Thus not only the order but also the absolute values of the vibronic coupling constants of C_{60}^- have not been determined so far. To solve this problem, both the agreement between theoretical and experimental vibronic constants and physical insight into the order of the couplings are necessary. One of the aims of this thesis is to determine the VCCs in C_{60}^-.

Recently, new photoelectron spectrum of C_{60}^- has been published by Wang *et al.* [57]. This spectrum is measured at lower temperature with higher resolution than the previous one by Gunnarsson *et al.* In the above spectrum [57], fine structures which originate from the vibronic couplings in C_{60}^- are seen. Therefore, this spectrum can be a candidate that gives an answer to the long standing problem.

Derivation from the photoelectron spectrum [57] and the density-functional theory (DFT) calculations are presented in chapter 1 in Part II. The order of the VCCs is explained in terms of the VCD in chapter 2 in Part II. The same DFT method is adopted for the derivation of the coupling constants of C_{60} derivatives used in organic photovoltaic cell as electron-transporting materials (chapter 4 in Part II).

0.5 Contents of the thesis

In this thesis, the author studies both fundamental vibronic problems and applications of the vibronic couplings in molecules.

Part I deals with two problems on the Jahn–Teller effect. The first one is concerned with the origin of the Jahn–Teller distortion. The second one is concerned with the isotope effect on the isotope-substituted Jahn–Teller system.

In chapter 1, the origin of the vibronic couplings in Jahn–Teller systems is discussed. We analyze the vibronic couplings in triangular and cubic molecules such as, Li_3 and Li_8^+. The nonzero vibronic couplings for the Jahn–Teller modes of Li_3 and Li_8^+ are explained in terms of the vibronic coupling density (VCD). In the case of Li_8^+, the electron density difference $\Delta\rho$ on the bonds and overlap density $\rho_{\gamma\gamma'}$ on the faces are crucial for the e_g and t_{2g} distortions, respectively. In the case of Li_3, $\Delta\rho$ on the bond is important for the Jahn–Teller distortion.

In chapter 2, isotope-substituted linear $E \otimes e$ Jahn–Teller model is analyzed. An isotopomer X_2Y of a triangular molecule X_3 (X = H, D, Li, etc.) is treated. Isotopic-substitution retains the one-dimensional trough in the adiabatic potential energy surface. However, due to change of the mass in the kinetic energy term, the potential for the pseudorotation is warped. This warped potential has two minima, which is in contrast to the three minima of the quadratic $E \otimes e$ Jahn–Teller system. As a result, the vibronic wavefunction is concentrated around the minima of the warped potential. Although the point group symmetry of the isotopomer X_2Y is no more than C_{2v}, each vibronic level is doubly degenerate. This degeneracy appears because of the additional parity symmetry of the Hamiltonian. These results were also obtained from numerical calculations. The vibronic coupling constants (VCC) of H_3 and Li_3 are calculated using the density-functional theory (DFT) calculations. The DFT calculations support the possibility of observation of the isotope effect on the isotopomers of these molecules.

Part II deals with the vibronic couplings in C_{60}^- and derivatives.

In chapter 1, the VCCs of C_{60}^- are evaluated from an experimental photoelectron spectrum of C_{60}^- and the DFT calculations. As a model Hamiltonian of C_{60}^-, we employ the linear $T_{1u} \otimes (2a_g \oplus 8h_g)$ Jahn–Teller Hamiltonian. The vibronic state is obtained diagonalizing the Jahn–Teller Hamiltonian numerically. Effect of the thermal excitation is taken into account assuming that each C_{60}^- is in the thermal equilibrium. The intensities

of the photoelectron spectrum is calculated within the sudden approximation. From the simulation of the photoelectron spectrum, it is clarified that the present stabilization energy is smaller than the previous experimental value by 30 %. The VCCs for the $h_g(7)$ and $h_g(8)$ modes turn out to be strong. On the other hand, the coupling for the $h_g(2)$ is so weak that the electron-phonon coupling for the mode cannot be the strongest. The coupling constants obtained from the DFT calculations agree well with the experimental ones.

In chapter 2, the order of the vibronic couplings in C_{60}^- are explained on the basis of the VCD analysis. The VCD for the bending $h_g(2)$ mode is localized around atoms, while that for the stretching $h_g(8)$ mode is delocalized on 6:6 C=C bonds. The localized VCD is canceled out, and thus the coupling for the bending mode becomes weak. The delocalized negative VCD contributes to the negative VCCs for the stretching modes. The delocalized VCD on the bonds originates from the polarized $\Delta\rho$. This polarized $\Delta\rho$ appears due to the orbital relaxation.

In chapter 3, the concept of the VCD is applied to the analysis of the Diels–Alder reaction of C_{60}. Following the theory of Parr and Yang, the strength of the vibronic coupling for the reactive mode can be regarded as an index of chemical reactivity. The distribution of the VCD of C_{60}^- is similar to that of ethylene monoanion. This result indicates that the reactivity of C_{60} is similar to that of ethylene in the Diels–Alder reaction. Considering the threefold degeneracy of the electronic state, C_{60} bears six ethylene moieties in its cage, which is consistent with the existence of hexakis adducts.

In chapter 4, the VCCs of several C_{60} derivatives which are used as electron-transport materials in organic photovoltaics are calculated. As the C_{60} derivatives, we treat [6,6]-phenyl-C-61-butyric acid methyl ether (PCBM) and C_{60} pyrrolidines. The vibronic couplings of C_{60} derivatives monoanions are close to the VCCs of C_{60}^-. The LUMOs of the C_{60} derivatives originate from the t_{1u} LUMO of a neutral C_{60}. The electron density differences $\Delta\rho$ of derivatives are localized on the C_{60} fragments. Consequently, the VCDs for the effective modes are close to that of C_{60}^-.

Part III deals with miscellaneous applications of the theory of the vibronic coupling.

In chapter 1, the initial photoactivation process of a photocatalyst, dispersed V_2O_5/SiO_2, is studied. The active species has been known to be VO_4 with C_{3v} symmetry. The a_2 HOMO and the e LUMO of the active species, VO_4, do not have large orbital coefficients

on the terminal oxygen in the ground state. Therefore, in the Franck–Condon state, it is difficult to explain the reactivity of VO_4. So far, a structural relaxation along the totally symmetric V=O stretching modes has been taken into account, while the Jahn–Teller distortion has not. In this work, the Jahn–Teller distortion of VO_4 in the excited state is considered. Accompanied with the Jahn–Teller distortion, the a_2 HOMO and the e HOMO-1 mix due to the vibronic coupling between these orbitals. Since the HOMO-1 has coefficients on the terminal oxygen, the HOMO has finite coefficients on the terminal oxygen after the Jahn–Teller distortion. Thereby, the active center of VO_4 is induced by the Jahn–Teller effect.

In chapter 2, the relationship between the vibronic coupling and spin multiplicity of the ground state of *m*-phenylene diamine derivative is discussed. The ground state of *m*-phenylene diamine dication is triplet. However, *m*-phenylene diamine with a methoxy group has a closed-shell singlet ground state. To recover the triplet state, the vibronic coupling in the singlet state must be reduced. The VCC of the singlet state can be controlled by introducing a substituent group. The reduction of the VCCs are discussed on the basis of the VCD analysis.

In chapter 3, the author presents the calculations of the vibronic coupling constants of picene in its anionic and the excited states and the VCD analysis. Using the theoretical VCCs of picene molecule in the excited state, the electron energy loss spectrum of the pristine picene is simulated at 20 K within the Franck–Condon approximation. The simulated spectrum is compared with the experimental spectrum. Similarly, the VCCs of picene molecule in the mono and the trianionic states are calculated. From our result, the vibronic coupling of the monoanion is the strongest for the C=C stretching mode. The VCC is analyzed in terms of the VCD. The coupling for the C=C stretching is strong because of considerable overlap between the electron density difference $\Delta\rho$ and the potential derivative v.

Bibliography

[1] I. B. Bersuker, and V. Z. Polinger, *Vibronic Interactions in Molecules and Crystals* (Springer–VerlagBerlin and Heidelberg, 1989).

[2] I. B. Bersuker, Chem. Rev. **101**, 1067 (2001).

[3] I. B. Bersuker, *The Jahn–Teller Effect* (Cambridge University PressCambridge, 2006).

[4] *The Dynamical Jahn–Teller Effect in Localized Systems*, edited by Y. E. Perlin, and M. Wagner (ElsevierAmsterdam, 1984).

[5] C. C. Chancey, and M. C. M. O'Brien, *The Jahn–Teller Effect in C_{60} and other Icosahedral Complexes* (Princeton University PressPrinceton, 1997).

[6] G. Fischer, *Vibronic Coupling: The interaction between the Electronic and Nuclear Motions* (Academic PressLondon, 1984).

[7] *The Jahn–Teller Effect: Fundamentals and Implications for Physics and Chemistry*, edited by H. Köppel, D. R. Yarkony, and H. Barentzen (Springer–VerlagBerlin and Heidelberg, 2009).

[8] T. Sato, K. Tokunaga, N. Iwahara, K. Shizu, and K. Tanaka, in *The Jahn–Teller Effect: Fundamentals and Implications for Physics and Chemistry*, edited by H. Köppel, D. R. Yarkony, and H. Barentzen (Springer–VerlagBerlin and Heidelberg, 2009), p. 99.

[9] T. Inui, Y. Tanabe, and Y. Onodera, *Group Theory and Its Applications in Physics, Springer Series in Solid-State Sciences* (SpringerBerlin, 1990), Vol. 78.

[10] T. Azumi, and K. Matsuzaki, Photochem. Photobiol. **25**, 315 (1977).

[11] H. A. Jahn, and E. Teller, Proc. R. Soc. A **161**, 220 (1937).

[12] H. C. Longuet-Higgins, U. Öpik, M. H. L. Pryce, and R. A. Sack, Proc. R. Soc. A **244**, 1 (1958).

[13] G. Herzberg, and H. C. Longuet-Higgins, Disc. Farad. Soc. **35**, 77 (1963).

[14] H. C. Longuet-Higgins, Proc. R. Soc. A **344**, 147 (1975).

[15] M. V. Berry, Proc. R. Soc. A **392**, 45 (1984).

[16] *Geometric Phases in Physics*, edited by A. Shapere, and F. Wilczek (World ScientificSingapore, 1989).

[17] F. S. Ham, Phys. Rev. Lett. **58**, 725 (1987).

[18] A. Auerbach, N. Manini, and E. Tosatti, Phys. Rev. B **49**, 12998 (1994).

[19] C. P. Moate, M. C. M. O'Brien, J. L. Dunn, C. A. Bates, Y. M. Lin, and V. Z. Polinger, Phys. Rev. Lett. **77**, 4362 (1996).

[20] H. Koizumi, and I. B. Bersuker, Phys. Rev. Lett. **83**, 3009 (1999).

[21] P. Garcia-Fernandez, I. B. Bersuker, and J. E. Boggs, Phys. Rev. Lett. **96**, 163005 (2006).

[22] H. J. Wörner, R. van der Veen, and F. Merkt, Phys. Rev. Lett. **97**, 173003 (2006).

[23] R. G. Lawler, J. R. Bolton, J. R. Fraenkel, and T. H. Brown, J. Am. Chem. Soc. **86**, 520 (1964).

[24] A. Carrington, H. C. Longuet-Higgins, R. E. Moss, and P. F. Todd, Mol. Phys. **9**, 187 (1965).

[25] L. Yu, D. W. Cullin, J. M. Williamson, and T. A. Miller, J. Chem. Phys. **98**, 2682 (1993).

[26] R. Bruckmeier, C. Wunderlich, and F. Figger, Phys. Rev. Lett. **72**, 2550 (1994).

[27] H.-G. Krämer, M. Keil, C. B. Suarez, W. Demtröder, and W. Meyer, Chem. Phys. Lett. **299**, 212 (1999).

[28] H. J. Wörner, and F. Merkt, J. Chem. Phys. **126**, 154304 (2007).

[29] D. G. Melnik, J. Liu, M.-W. Chen, T. A. Miller, and R. F. Curf, J. Chem. Phys. **135**, 094310 (2011).

[30] A. Ceulemans, and E. Lijnen, in *The Jahn–Teller Effect: Fundamentals and Implications for Physics and Chemistry*, edited by H. Köppel, D. R. Yarkony, and H. Barentzen (Springer–VerlagBerlin and Heidelberg, 2009), p. 25.

[31] A. Ceulemans, E. Lijnen, P. W. Fowler, R. B. Mallion, and T. Pisanski, Proc. R. Soc. A (2011).

[32] T. Sato, K. Tokunaga, and K. Tanaka, J. Phys. Chem. A **112**, 758 (2008).

[33] T. Sato, K. Shizu, T. Kuga, K. Tanaka, and H. Kaji, Chem. Phys. Lett. **458**, 152 (2008).

[34] K. Shizu, T. Sato, K. Tanaka, and H. Kaji, Chem. Phys. Lett. **486**, 130 (2010).

[35] K. Shizu, T. Sato, K. Tanaka, and H. Kaji, Org. Elec. **11**, 1277 (2010).

[36] T. Sato, K. Shizu, K. Uegaito, N. Iwahara, K. Tanaka, and H. Kaji, Chem. Phys. Lett. **507**, 151 (2011).

[37] K. Shizu, T. Sato, K. Tanaka, and H. Kaji, Appl. Phys. Lett. **97**, 142111 (2010).

[38] K. Shizu, T. Sato, A. Ito, K. Tanaka, and H. Kaji, J. Mater. Chem. **21**, 6375 (2011).

[39] R. G. Parr, and W. Yang, J. Am. Chem. Soc. **106**, 4049 (1984).

[40] O. Gunnarsson, Rev. Mod. Phys. **69**, 575 (1997).

[41] O. Gunnarsson, *Alkali-Doped Fullerides: Narrow-Band Solids with Unusual Properties* (World ScientificSingapore, 2004).

[42] Y. Iwasa, and T. Takenobu, J. Phys.: Condens. Matter **15**, R495 (2003).

[43] M. Capone, M. Fabrizio, C. Castellani, and E. Tosatti, Rev. Mod. Phys. **81**, 943 (2009).

[44] N. Manini, and E. Tosatti, *Jahn–Teller and Coulomb correlations in fullerene ions and compounds* (LAP Lambert Academic PublishingSaarbrücken, 2010).

[45] P. M. Allemand, K. C. Khemani, A. Koch, F. Wudl, K. holczer, S. Donovan, G. Grüner, and J. D. Thompson, Science **253**, 301 (1991).

[46] M. Lannoo, G. A. Baraff, M. Schlüter, and D. Tomanek, Phys. Rev. B **44**, 12106 (1991).

[47] C. M. Varma, J. Zaanen, and K. Raghavachari, Science **254**, 989 (1991).

[48] N. Manini, A. D. Carso, M. Fabrizio, and E. Tosatti, Philos. Mag. B **81**, 793 (2001).

[49] M. Saito, Phys. Rev. B **65**, 220508(R) (2002).

[50] T. Frederiksen, K. J. Franke, A. Arnau, G. Schulze, J. I. Pascual, and N. Lorente, Phys. Rev. B **78**, 233401 (2008).

[51] J. Laflamme Janssen, M. Côté, S. G. Louie, and M. L. Cohen, Phys. Rev. B **81**, 073106 (2010).

[52] C. Faber, J. Laflamme Janssen, M. Côté, E. Runge, and X. Blase, Phys. Rev. B **84**, 155104 (2011).

[53] O. Gunnarsson, H. Handschuh, P. S. Bechthold, B. Kessler, G. Ganteför, and W. Eberhardt, Phys. Rev. Lett. **74**, 1875 (1995).

[54] N. Breda, R. A. Broglia, G. Colò, H. E. Roman, F. Alasia, G. Onida, V. Ponomarev, and E. Vigezzi, Chem. Phys. Lett. **286**, 350 (1998).

[55] I. D. Hands, J. L. Dunn, and C. A. Bates, Phys. Rev. B **63**, 245414 (2001).

[56] I. D. Hands, J. D. Dunn, and C. A. Bates, in *Advances in Quantum Chemistry*, edited by J. R. Sabin, and E. Brändas (Elsevier Academic PressSan Diego, 2003), Vol. 44, p. 335.

[57] X. B. Wang, H. K. Woo, and L. S. Wang, J. Chem. Phys. **123**, 051106 (2005).

Part I

Fundamental Aspects of Vibronic Coupling

Chapter 1

Origin of the Jahn-Teller Distortions: Vibronic Coupling Density Analysis for Jahn-Teller Molecules

1.1 Why is a Jahn-Teller molecule distorted?

In 1937 Jahn and Teller stated a theorem that is known as Jahn-Teller theorem nowadays [1]:

> All non-linear nuclear configurations are therefore unstable for an orbitally degenerate electronic state.

This theorem is restated that a nonlinear molecule with a degenerate electronic state is distorted into a nuclear configuration without degeneracy. Since a molecule with a symmetry axis C_n or S_n ($n \geq 3$) can have an electronic degeneracy, such a molecule is distorted into a low symmetry structure. The symmetry-lowering distortion is called a Jahn-Teller distortion.

Jahn and Teller proved this theorem by making a thorough investigation for all the relevant point groups [1]. Recently Ceulemans and Lijnen have proved the theorem elegantly employing permutational groups [2, 3].

The vibrational mode Γ_v which is responsible for the Jahn-Teller distortion in a Jahn-Teller molecule with a degenerate electronic state Γ_e is predicted by the selection rule

$$\Gamma_v = \left[\Gamma_e^2\right] - A_1, \tag{1.1}$$

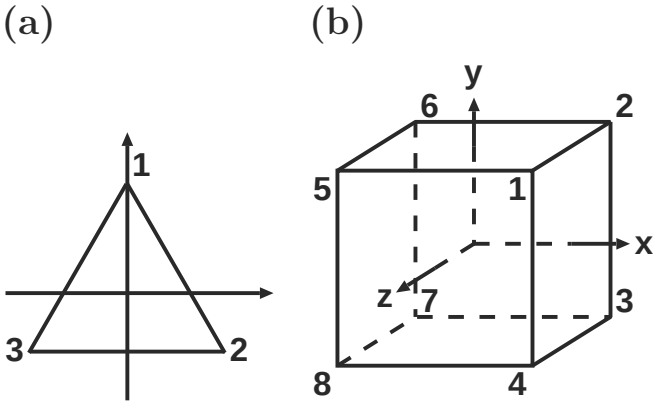

Figure 1.1: Structure of the model Jahn-Teller molecules.(a) Triangle and (b) cubic.

where $[\Gamma^2]$ denotes the symmetric product representation of the irreducible representation Γ, and A_1 the totally symmetric representation [4]. The selection rule is based on an integral of a vibronic coupling [5]

$$\left\langle \Psi_{\Gamma_e\gamma_e} \left| \left(\frac{\partial H}{\partial Q_{\Gamma_v\gamma_v}} \right)_{\mathbf{R}_0} \right| \Psi_{\Gamma_e\gamma'_e} \right\rangle, \tag{1.2}$$

where H is a molecular Hamiltonian, γ distinguishes the degenerate representation Γ, $Q_{\Gamma_v\gamma_v}$ denotes a mass-weighted normal coordinate of the Jahn-Teller active mode $\Gamma_v\gamma_v$, $\Psi_{\Gamma_e\gamma_e}$ degenerate electronic wavefunction, and $\mathbf{R}_0$ undistorted symmetric nuclear-configuration. The integral can be factorized as a product between a Clebsch-Gordan coefficient $\langle \Gamma_e\gamma_e | \Gamma_e\gamma'_e\Gamma_v\gamma_v \rangle$ and a reduced matrix element $\langle \Gamma_E || \Gamma_v || \Gamma_E \rangle$. Therefore, the vibronic coupling constant $V_{\Gamma_e\times\Gamma_v}$ depends on Γ_e and Γ_v, not on γ_e and γ_v.

The displacement of the Jahn-Teller distortion is expressed by $V_{\Gamma_e\times\Gamma_v}$. For a doubly degenerate electronic state E in a triangle molecule (Fig. 1.1(a)), doubly degenerate vibrational mode e couples with the electronic state. A Hamiltonian for the $E \times e$ Jahn-Teller molecule is given by

$$H_{E\times e} = V_{E\times e} \begin{pmatrix} Q_\theta & -Q_\epsilon \\ -Q_\epsilon & -Q_\theta \end{pmatrix} + \frac{1}{2}\omega^2 \left(Q_\theta^2 + Q_\epsilon^2\right) \begin{pmatrix} 1 & 0 \\ 0 & 1 \end{pmatrix}, \tag{1.3}$$

where Q_θ and Q_ϵ are the mass-weighted normal coordinates, and ω the vibrational frequency of the Jahn-Teller active mode [6, 7]. The eigen values of $H_{E\times e}$ is obtained as

$$E^{\pm}_{E\times e}(Q_\theta, Q_\epsilon) = \frac{1}{2}\omega^2 \left(Q_\theta^2 + Q_\epsilon^2\right) \pm V_{E\times e} \left|Q_\theta^2 + Q_\epsilon^2\right| = \frac{1}{2}\omega^2\rho^2 \pm |V_{E\times e}|\,\rho, \tag{1.4}$$

where $Q_\theta = \rho\cos\phi$ and $Q_\epsilon = \rho\sin\phi$. For the lower energy

$$E^{-}_{E\times e}(\rho) = \frac{1}{2}\omega^2 \left(\rho - \frac{|V_{E\times e}|}{\omega^2}\right)^2 - \frac{V^2_{E\times e}}{2\omega^2}, \tag{1.5}$$

the molecule relaxes by the Jahn-Teller distortion

$$\rho_{E\times e} = \frac{|V_{E\times e}|}{\omega^2}, \tag{1.6}$$

and the stabilization energy (Jahn-Teller energy) is

$$E_{E\times e} = \frac{V_{E\times e}^2}{2\omega^2}. \tag{1.7}$$

Accordingly the Jahn-Teller distortion is dominated by the vibronic coupling constant.

For a cubic X_8 cluster, when a three-fold degenerate electronic state T couples with a three-fold degenerate vibrational mode t_2, a Hamiltonian of the $T \times t_2$ Jahn-Teller molecule is written by

$$H_{T\times t_2} = V_{T\times t_2} \begin{pmatrix} 0 & Q_{xy} & Q_{zx} \\ Q_{xy} & 0 & Q_{yz} \\ Q_{zx} & Q_{yz} & 0 \end{pmatrix} + \frac{1}{2}\omega^2 \left(Q_{xy}^2 + Q_{zx}^2 + Q_{yz}^2\right) \begin{pmatrix} 1 & 0 & 0 \\ 0 & 1 & 0 \\ 0 & 0 & 1 \end{pmatrix}, \tag{1.8}$$

where $V_{T\times t_2}$ is a vibronic coupling constant, Q_{xy}, Q_{zx}, and Q_{yz} are mass-weighted normal coordinates of the t_2 mode [6].

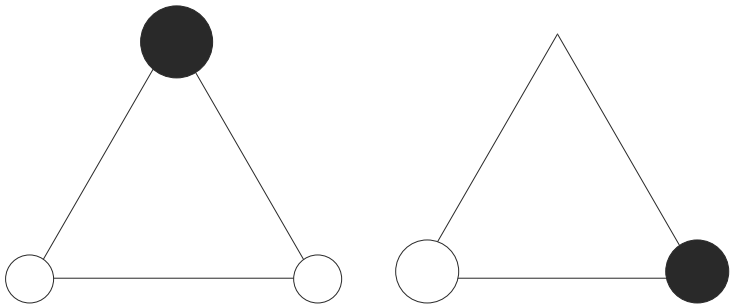

Figure 1.2: Symmetry adapted molecular orbitals of the triangle molecule.

From Eq. (1.2), the vibronic coupling constant corresponds to a force acting on the molecular framework. We consider the simplest model Jahn-Teller molecule X_3 in which an s atomic orbital $|i\rangle$ $(i = 1, 2, 3)$ is located on each site. What is the origin of the driving force of the Jahn-Teller distortion? A naïve explanation would be as follows: since degenerate frontier orbitals are

$$|\theta\rangle = \frac{1}{\sqrt{6}}\left(2\,|1\rangle - |2\rangle - |3\rangle\right), \tag{1.9}$$

$$|\epsilon\rangle = \frac{1}{\sqrt{2}}\left(|3\rangle - |2\rangle\right), \tag{1.10}$$

and the on-site density is not totally symmetric, the resulting positive and negative Mulliken charges are responsible for the Jahn-Teller distortion.

However, there is a counter example for which such an explanation cannot be valid. In the case of a cubic X_8 cluster with an s atomic orbital $|i\rangle \quad (i = 1, 2, \cdots, 8)$ on each site, since three-fold degenerate orbitals are

$$|x\rangle = \frac{1}{2\sqrt{2}} \left(|1\rangle + |2\rangle + |3\rangle + |4\rangle - |5\rangle - |6\rangle - |7\rangle - |8\rangle \right), \tag{1.11}$$

$$|y\rangle = \frac{1}{2\sqrt{2}} \left(|1\rangle + |2\rangle - |3\rangle - |4\rangle + |5\rangle + |6\rangle - |7\rangle - |8\rangle \right), \tag{1.12}$$

$$|z\rangle = \frac{1}{2\sqrt{2}} \left(|1\rangle - |2\rangle - |3\rangle + |4\rangle + |5\rangle - |6\rangle - |7\rangle + |8\rangle \right), \tag{1.13}$$

and all the on-site density are equal to 1/8, there occurs no charge polarization in spite of the orbital degeneracy.

The Mulliken population analysis fails to explain the driving force of the Jahn-Teller distortion in the X_8 molecule.

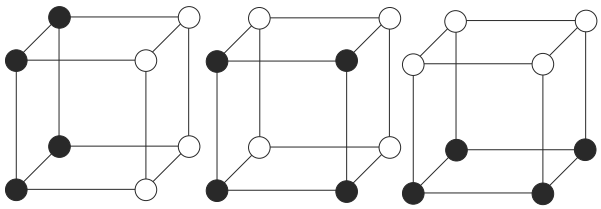

Figure 1.3: Symmetry adapted molecular orbitals of the cubic molecule.

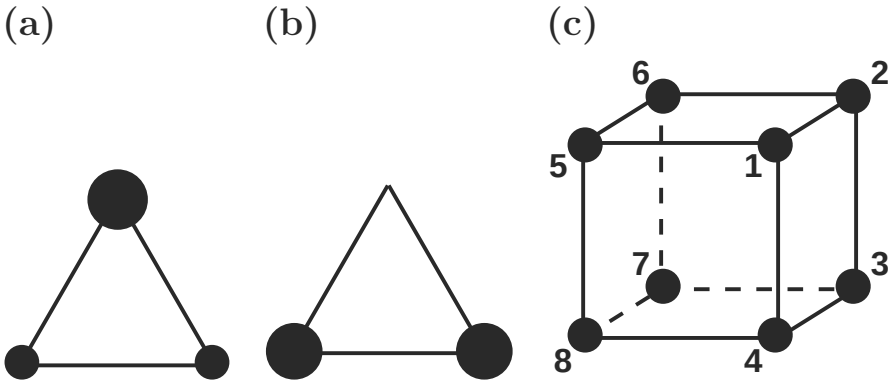

Figure 1.4: On-site charge distributions of the model Jahn-Teller molecules. (a) (b) of the triangle molecule, and (c) cubic.

1.2 Vibronic coupling density analysis

1.2.1 Definitions

Vibronic coupling density η [7–11] for a $E \times e$ Jahn-Teller molecule and non Jahn-Teller molecule (diagonal vibronic interaction, see Eq.(1.3)) is defined by

$$\eta(\mathbf{r}) = \Delta\rho_{\gamma_e}(\mathbf{r}) \times v(\mathbf{r}), \tag{1.14}$$

where $\Delta\rho$ is the electron density difference between the degenerate electronic state Ψ and a non-degenerate (neutral or ionic) reference electronic state. The reference configuration $\mathbf{R}_0$ in Eq.(1.2) is defined by an equilibrium configuration for the reference electronic state Ψ_0.

$$\Delta\rho(\mathbf{r}) = \rho(\mathbf{r}) - \rho_0(\mathbf{r}), \tag{1.15}$$

where $\rho(\mathbf{r})$ and $\rho_0(\mathbf{r})$ are one-electron densities for Ψ and Ψ_0, respectively. $v(\mathbf{r})$ is one-electron part of the potential derivative with respect to $Q_{\Gamma_v\gamma_v}$:

$$\left(\frac{\partial U_{ne}}{\partial Q_{\Gamma_v\gamma_v}}\right)_{\mathbf{R}_0} = \sum_i^N v(\mathbf{r}_i) = \sum_i^N \sum_{A=1}^M v_A(\mathbf{r}_i), \tag{1.16}$$

where U_{ne} is the nuclear-electronic potential, M and N are the numbers of the nuclei and electrons, respectively.

For a $T \times t_2$ Jahn-Teller molecule (off-diagonal vibronic interaction, see Eq.(1.8)),

$$\eta(\mathbf{r}) = \rho_{\gamma_e\gamma'_e}(\mathbf{r}) \times v(\mathbf{r}), \tag{1.17}$$

where $\rho_{\gamma_e\gamma'_e}(\mathbf{r})$ is a overlap density defined by

$$\rho_{\gamma_e\gamma'_e}(\mathbf{r}) = \int \cdots \int d\mathbf{r}_2 \cdots d\mathbf{r}_N \Psi^*_{\gamma_e}(\mathbf{r}, \mathbf{r}_2, \cdots, \mathbf{r}_N)\Psi_{\gamma'_e}(\mathbf{r}, \mathbf{r}_2, \cdots, \mathbf{r}_N). \tag{1.18}$$

Vibronic coupling constant and vibronic coupling density has the following relation:

$$V_{\Gamma_e\times\Gamma_v} = \int d\mathbf{r}\eta(\mathbf{r}). \tag{1.19}$$

Therefore, η describes a local picture of the vibronic coupling in terms of the electronic and vibrational structures through Eqs. (1.14) and (1.17). Moreover, atomic vibronic coupling density η_A is obtained by replacing v by v_A in Eqs. (1.14) and (1.17). Atomic vibronic coupling constant is defined by

$$V_A = \int d\mathbf{r}\eta_A(\mathbf{r}), \tag{1.20}$$

and

$$V_{\Gamma_e \times \Gamma_v} = \sum_{A=1}^{M} V_A. \tag{1.21}$$

Derivation of vibronic coupling density is discussed in detail in Ref. [7].

Vibronic coupling density η contains zero component η' which yield no contribution to V because of the symmetry of v and ρ around each atom [12]. Reduced vibronic coupling density (RVCD) $\bar{\eta}$ is defined by

$$\bar{\eta}(\mathbf{r}) = \eta(\mathbf{r}) - \eta'(\mathbf{r}), \tag{1.22}$$

and

$$V = \int d\mathbf{r}\eta(\mathbf{r}) = \int d\mathbf{r}\bar{\eta}(\mathbf{r}). \tag{1.23}$$

1.2.2 Li_8^+

As a real system for X_8, we calculated a cluster ion Li_8^+. Geometry optimization and vibrational analysis of Li_8 was performed at RHF/6-31G(d) level of theory. Electronic state of Li_8^+ was calculated at state-averaged CAS(5,3)/6-31G(d) level of theory. The geometry is constrained in a cubic structure. For the optimizations, vibrational analysis, and force calculations, we used Gaussian 09 [13].

Table 1.1: Vibronic coupling constants of Li_8^+.

	Frequency(cm^{-1})	VCC(10^{-4} a.u.)
$a_{1g}(1)$	224.5	-11.3209
$e_g(1)$	272.1	-8.7535
$t_{2g}(1)$	$46.4i$	-2.2199
$t_{2g}(2)$	232.9	-3.4048

The VCCs of Li_8^+ are tabulated in Table 1.2.2. We discuss the $t_{2g}(2)$ and $e_g(1)$ modes.

Figures 1.5 shows the VCD η, zero component η', and RVCD $\bar{\eta}$. There are on-site symmetric negative and positive regions in the distribution of the VCD and RVCD, as well as large negative regions on the bonds. Although the on-site symmetric VCD cancels out, the negative VCD on the bonds contributes to the negative V of the $t_{2g}(2)$ mode.

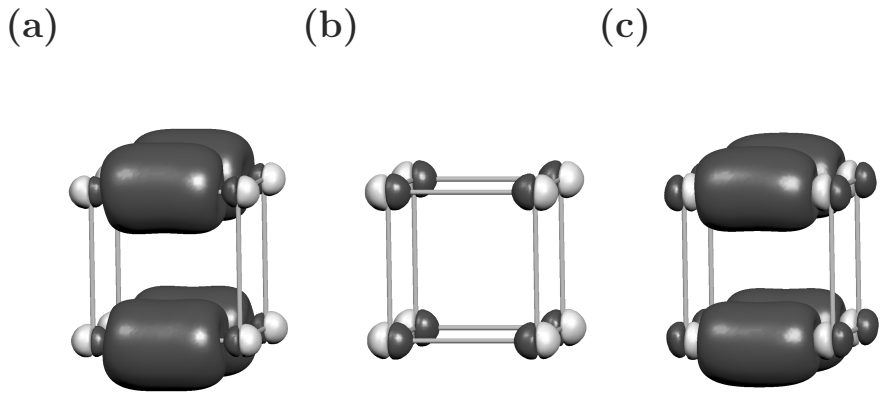

Figure 1.5: Vibronic coupling density for $t_{2g}(2)$ mode of Li_8^+ (isovalue:1.0×10^{-6} a.u.). (a) VCD $\eta(\mathbf{r})$, (b) zero component $\eta^{'}(\mathbf{r})$, and (c) RVCD $\bar{\eta}(\mathbf{r})$. Light grey is positive, and dark gray is negative.

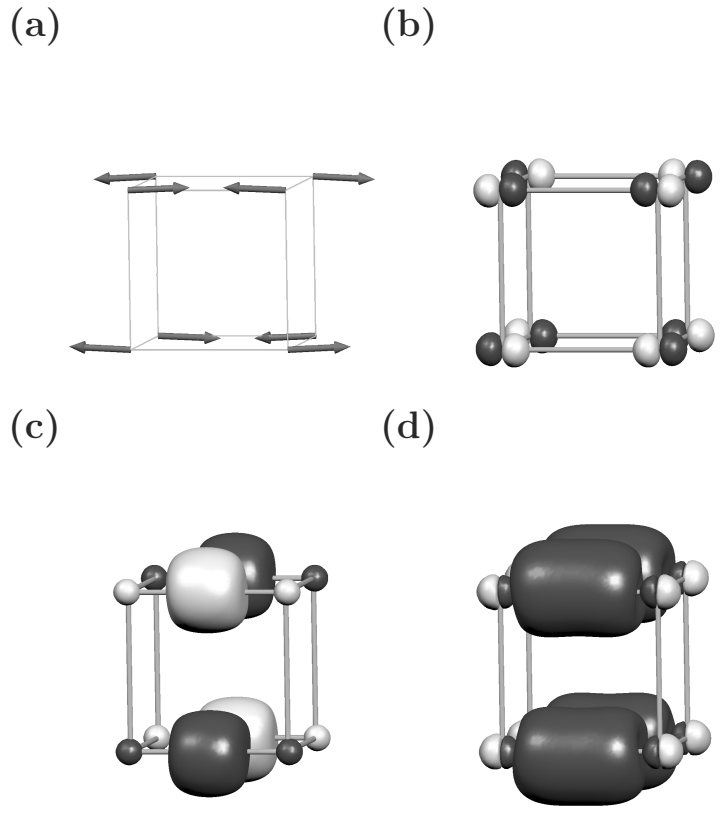

Figure 1.6: Vibronic coupling density analysis for $t_{2g}(2)$ mode of Li_8^+. (a) $t_{2g}(2)$ mode, (b) potential derivative $v(\mathbf{r})$ (isovalue:1.0×10^{-2} a.u.), (c) overlap density $\rho_{x,y}(\mathbf{r})$ (isovalue:1.0×10^{-3} a.u.), and (d) VCD $\eta(\mathbf{r})$ (isovalue:1.0×10^{-6} a.u.).

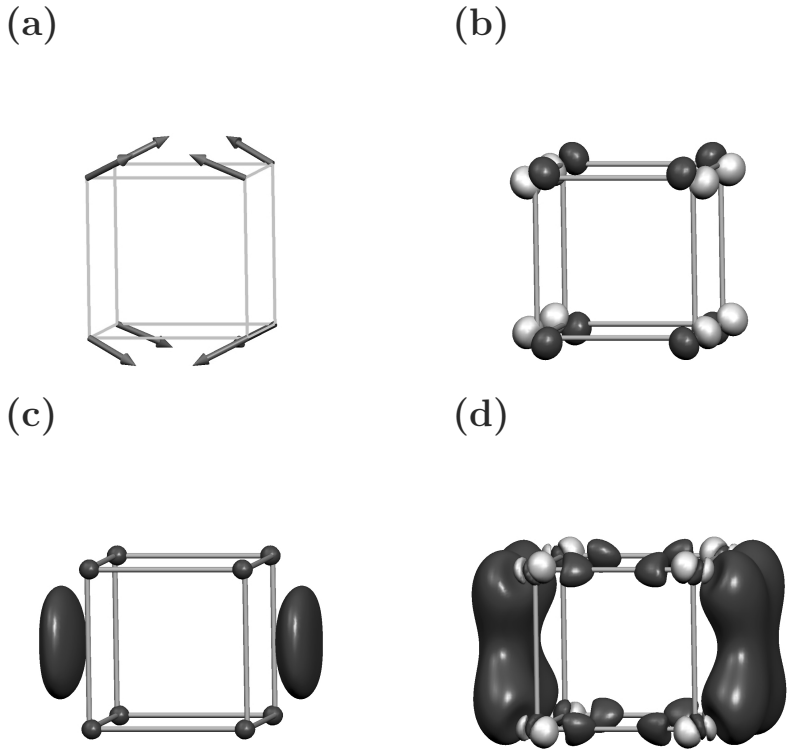

Figure 1.7: Vibronic coupling density analysis for $e_g(\theta)$ mode of Li_8^+. (a) $e_g(\theta)$ mode, (b) potential derivative $v(\mathbf{r})$ (isovalue:1.0×10^{-2} a.u.), (c) electron density difference $\Delta\rho(\mathbf{r})$ (isovalue:5.0×10^{-3} a.u.), and (d) VCD $\eta(\mathbf{r})$ (isovalue:2.0×10^{-6} a.u.).

The negative VCD on the bonds originate from the distribution of the overlap density. In Fig. 1.6(b), the potential derivative v has a symmetric on-site distribution, while the overlap density $\rho_{x,y}$ (Fig. 1.6(c)) has a spherically-symmetric on-site distribution as well as a distribution on the bonds. The spherically symmetric $\rho_{x,y}$ does not contribute to V because of the on-site symmetry of v.

Therefore the vibronic coupling originates from the on-bond distributions of the overlap density. Mulliken population analysis smears these effects. As in the case of the $t_{2g}(2)$ mode,

the potential derivative for the e_g mode has symmetric on-site distribution (Fig. 1.7 (b)). The electron density difference $\Delta\rho$ (Fig. 1.7 (c)) has a symmetrical on-site distribution and a distribution on the face of the cube. This density on the face couples to the potential derivative v. Consequently the vibronic coupling density has large negative distribution on the face which contribute to the negative V for the e_g mode.

1.2.3 Li_3

As a real system for X_3, we took a triangle cluster Li_3. Geometry optimization and vibrational analysis of Li_3^+ was performed at RHF/6-31G(d) level of theory. Electronic state of Li_3 was calculated at state-averaged CAS(1,2)/6-31G(d) level of theory.

Table 1.2: Vibronic coupling constants of Li_3.

	Frequency(cm^{-1})	VCC(10^{-4} a.u.)
a_1'(1)	298.0	-8.3947
e'(1)	240.8	-5.2665

In Table 1.2 and 1.3, the VCCs and AVCC for $e'(1)$ mode of Li_3 are summarized, respectively.

We focus on the Jahn-Teller-active e' θ mode. Figures 1.8 shows the VCD analysis of the Li_3. Apparently Mulliken population analysis for this case appears to be succeeded. However, this is not the case also. Because of the on-site symmetry of v, the on-site distribution of the electron density difference $\Delta\rho$ does not contribute to the VCC. It is clear that the on-bond distributions of the electron density difference does contribute to the VCC.

Table 1.3: Atomic vibronic coupling constants of Li_3.

	AVCC(10^{-4} a.u.)
Li(1)	-1.57163693
Li(2)	-3.41907866
Li(3)	-3.41907866

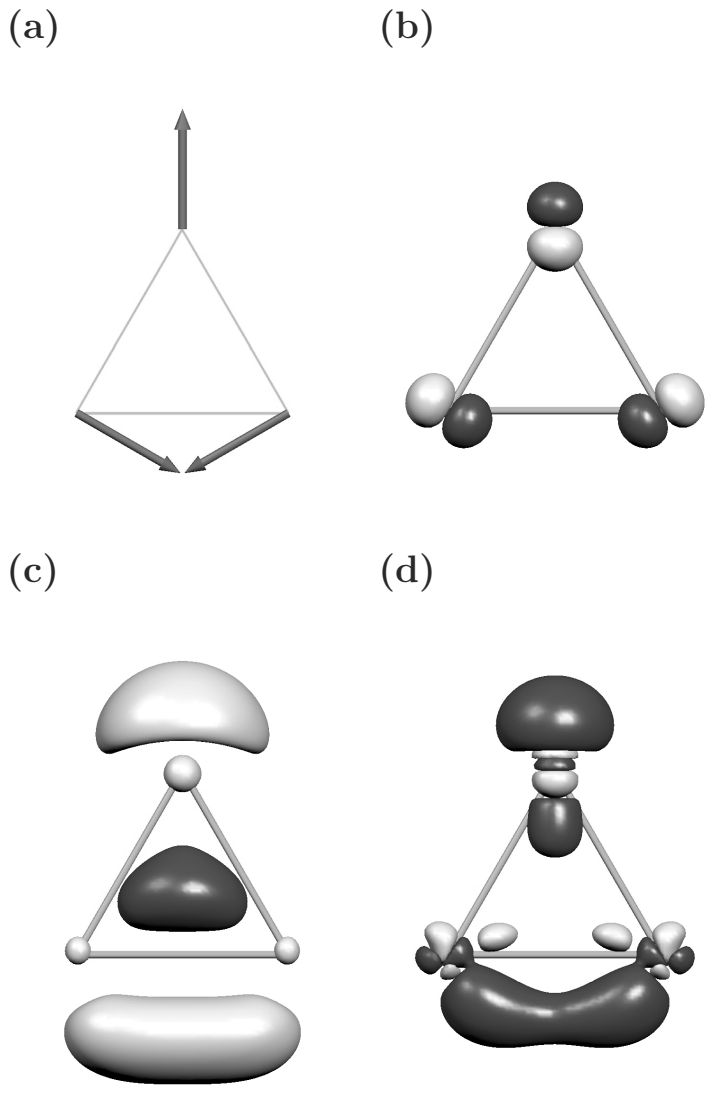

Figure 1.8: Vibronic coupling density analysis for $e'\theta$ mode of Li_3. (a) $e'\theta$ mode, (b) potential derivative $v(\mathbf{r})$ (isovalue:1.0×10^{-2} a.u.), (c) electron density difference between Li_3^+ $\Delta\rho_\theta(\mathbf{r})$
(isovalue:2.0×10^{-3} a.u.), and (d) VCD $\eta(\mathbf{r})$ (isovalue:5.0×10^{-6} a.u.).

1.3 Non-Jahn-Teller molecules

When the electronic state of a molecule changes, there occurs vibronic interactions with totally symmetric modes even for non-Jahn-Teller molecules, since the symmetric representation of any irreducible representation contains a totally symmetric irreducible representation.

The VCD analysis has been applied for a naphthalene anion [11]. It has been found that orbital relaxation is crucial in the vibronic couplings.

Vibronic couplings play an important role in a carrier-transporting molecule for organic light-emitting diodes. They inhibit carrier transports, and give rise to a reduction of the mobility and an energy dissipation due to the inelastic scattering of a carrier with phonons. In order to investigate carrier-transporting molecules, the VCD analysis has been applied for hole-transporting molecules, TPD [14], TPA [12], and CBP [15]. It has been found that strong localization of the electron density difference on atoms give rise to weak vibronic couplings. On-bond density gives rise to increase of vibronic couplings. Based on this finding, a novel electron-transporting molecule has been designed [16]. The VCD analysis has been also applied for other fields, a single electron transport through molecular wires, oligothiophenes [17], the simulation of an inelastic electron tunneling spectra [18], and well-known organic donor, BEDT-TTF [19].

Pseudo Jahn-Teller molecules in which vibronic couplings with excited electronic configurations give rise to a distortion or red shift in frequency are another important class of non-Jahn-Teller molecules [6]. An application of the VCD analysis for pseudo Jahn-Teller molecules will be discussed in the future.

Bibliography

[1] H. A. Jahn, and E. Teller, Proc. R. Soc. A **161**, 220 (1937).

[2] A. Ceulemans, and E. Lijnen, Bull. Chem. Soc. Jpn. **80**, 1229 (2007).

[3] A. Ceulemans, and E. Lijnen, in *The Jahn–Teller Effect: Fundamentals and Implications for Physics and Chemistry*, edited by H. Köppel, D. R. Yarkony, and H. Barentzen (Springer–VerlagBerlin and Heidelberg, 2009), p. 25.

[4] T. Inui, Y. Tanabe, and Y. Onodera, *Group Theory and Its Applications in Physics, Springer Series in Solid-State Sciences* (SpringerBerlin, 1990), Vol. 78.

[5] G. Fischer, *Vibronic Coupling: The interaction between the Electronic and Nuclear Motions* (Academic PressLondon, 1984).

[6] I. B. Bersuker, and V. Z. Polinger, *Vibronic Interactions in Molecules and Crystals* (Springer–VerlagBerlin and Heidelberg, 1989).

[7] T. Sato, K. Tokunaga, N. Iwahara, K. Shizu, and K. Tanaka, in *The Jahn–Teller Effect: Fundamentals and Implications for Physics and Chemistry*, edited by H. Köppel, D. R. Yarkony, and H. Barentzen (Springer–VerlagBerlin and Heidelberg, 2009), p. 99.

[8] T. Sato, K. Tokunaga, and K. Tanaka, J. Chem. Phys. **124**, 024314 (2006).

[9] T. Sato, K. Tokunaga, and K. Tanaka, J. Chem. Phys. **124**, 154303 1 (2006).

[10] K. Tokunaga, T. Sato, and K. Tanaka, J. Mol. Struct. **838**, 116 (2007).

[11] T. Sato, K. Tokunaga, and K. Tanaka, J. Phys. Chem. A **112**, 758 (2008).

[12] K. Shizu, T. Sato, K. Tanaka, and H. Kaji, Chem. Phys. Lett. **486**, 130 (2010).

[13] M. J. Frisch, G. W. Trucks, H. B. Schlegel, G. E. Scuseria, M. A. Robb, J. R. Cheeseman, G. Scalmani, V. Barone, B. Mennucci, G. A. Petersson, H. Nakatsuji, M. Caricato, X. Li, H. P. Hratchian, A. F. Izmaylov, J. Bloino, G. Zheng, J. L. Sonnenberg, M. Hada, M. Ehara, K. Toyota, R. Fukuda, J. Hasegawa, M. Ishida, T. Nakajima, Y. Honda, O. Kitao, H. Nakai, T. Vreven, J. J. A. Montgomery, J. E. Peralta, F. Ogliaro, M. Bearpark, J. J. Heyd, E. Brothers, K. N. Kudin, V. N. Staroverov, T. Keith, R. Kobayashi, J. Normand, K. Raghavachari, A. Rendell, J. C. Burant, S. S. Iyengar, J. Tomasi, M. Cossi, N. Rega, J. M. Millam, M. Klene, J. E. Knox, J. B. Cross, V. Bakken, C. Adamo, J. Jaramillo, R. Gomperts, R. E. Stratmann, O. Yazyev, A. J. Austin, R. Cammi, C. Pomelli, J. W. Ochterski, R. L. Martin, K. Morokuma, V. G. Zakrzewski, G. A. Voth, P. Salvador, J. J. Dannenberg, S. Dapprich, A. D. Daniels, O. Farkas, J. B. Foresman, J. V. Ortiz, J. Cioslowski, and D. J. Fox, *Gaussian 09, Revision B.01*, Wallingford CT, 2010.

[14] T. Sato, K. Shizu, T. Kuga, K. Tanaka, and H. Kaji, Chem. Phys. Lett. **458**, 152 (2008).

[15] T. Sato, K. Shizu, K. Uegaito, N. Iwahara, K. Tanaka, and H. Kaji, Chem. Phys. Lett. **507**, 151 (2011).

[16] K. Shizu, T. Sato, K. Tanaka, and H. Kaji, Appl. Phys. Lett. **97**, 142111 (2010).

[17] K. Shizu, T. Sato, and K. Tanaka, Chem. Phys. **369**, 108 (2010).

[18] K. Shizu, T. Sato, and K. Tanaka, Nanoscale **2**, 2186 (2010).

[19] K. Shizu, T. Sato, and K. Tanaka, Chem. Phys. Lett. **491**, 65 (2010).

Chapter 2

Kinetic Localization in an Isotope-Substituted Jahn–Teller System

The Jahn–Teller effect has attracted much attention because it is not only one of the intriguing topics in molecular physics but also crucial to the optical and magnetic properties of point defects, electronic properties of fullerides, and so on [1, 2]. Therefore, an insight into a vibronic state is a key to reveal the properties of molecules and solids. The structure of the adiabatic potential energy surface plays a crucial role in studies on the Jahn–Teller effect. For instance, a warping of the potential surface gives rise to the localization of a vibronic wavefunction. The warping of the potential surface can originate from quadratic vibronic couplings [1]. In this chapter, we propose a different mechanism of the localization of kinetic origin in isotope-substituted Jahn–Teller systems. Substituting some of the nuclei by their isotopes, the degeneracy of the vibrational states is lifted. On the other hand, the electronic states remain degenerate. In other words, the isotopic substitution affects not on the potential energy term but on the kinetic energy term. The isotope effect on the kinetic energy may play a role as the quadratic vibronic coupling in the potential energy term in a Jahn-Teller system.

Isotope effects on Jahn–Teller systems have been observed in spectroscopic studies [3–9]. In these investigations, the isotope effects have been explained on the basis of the preferable Jahn–Teller distortion which arises through the zero-point energy [4, 8, 9]. However, the mechanism of the distortion induced by an isotope substitution has not

been established. Moreover, in previous treatments, the role of the Berry phase in the Jahn–Teller system [10] with an isotope substitution has not been fully discussed.

As an example of the Jahn-Teller system, we adopt a trimer X_3 (X = H, D, Li, Na, etc.) with D_{3h} symmetry. In the Cartesian coordinates, the vibronic Hamiltonian which incorporates the linear $E \otimes e$ Jahn–Teller interaction is written as

$$\hat{H} = \left(\sum_{i=1}^{9} \frac{\hat{p}_i^2}{2m_0} + \sum_{i,j=1}^{9} \frac{K_{ij}}{2} x_i x_j \right) \hat{\sigma}_0 - \sum_{i=1}^{9} x_i \left(\mathbf{F}_{\theta,i} \hat{\sigma}_z + \mathbf{F}_{\epsilon,i} \hat{\sigma}_x \right), \tag{2.1}$$

where x_i and $\hat{p}_i$ are the nuclear displacements and the conjugated momenta, K_{ij} the Hessian, $\mathbf{F}_{\gamma,i} (\gamma = \theta, \epsilon)$ the vibronic coupling for x_i, m_0 the mass of nucleus X, $\hat{\sigma}_0$ the 2×2 unit matrix, and $\hat{\sigma}_x$ and $\hat{\sigma}_z$ the Pauli matrices. $\mathbf{F}_\gamma$'s are chosen so that the vibronic coupling constants to the mass-weighted a_1' and e' modes are 0 and V_E, respectively.

The vibronic Hamiltonian for the isotopomer X_2Y is obtained replacing one of the mass of X with that of an isotope Y in the kinetic energy term. The electronic state is unaffected by the substitution, and the Hessian K_{ij} and vibronic coupling $\mathbf{F}_\gamma$ do not change. The symmetry of the substituted system is reduced from D_{3h} to C_{2v}. Therefore the a_1' and e' modes in the original system are mixed since $a_1' \downarrow C_{2v} = a_1$ and $e' \downarrow C_{2v} = a_1 \oplus b_1$. Consequently, the doubly degenerate electronic state couples to the two a_1 modes and b_1 mode. Passing from Eq. (2.1) to the vibronic Hamiltonian for the substituted system in the mass-weighted normal coordinate,

$$\hat{H} = \sum_{\alpha} \frac{1}{2} \left(\hat{P}_\alpha^2 + \omega_\alpha^2 Q_\alpha^2 \right) \hat{\sigma}_0 + \sum_{i=1}^{2} V_{a_1(i)} Q_{a_1(i)} \hat{\sigma}_z + V_{b_1} Q_{b_1} \hat{\sigma}_x, \tag{2.2}$$

where $\alpha = a_1(1), a_1(2), b_1$, Q_α and $\hat{P}_\alpha$ are the mass-weighted normal coordinates and the conjugated momenta, respectively, ω_α the frequency of the mode α, and V_α the vibronic coupling constants. The Hamiltonian has one-dimensional trough (Fig. 2.1). The stabilization energy is the same as that of Eq. (2.1) E_{JT} because the potential terms do not change upon the isotope substitution.

Although the vibronic Hamiltonian (2.2) lose the rotational symmetry $SO(2)$ in the linear $E \otimes e$ Jahn–Teller Hamiltonian (2.1), each eigenstate of Hamiltonian (2.2) is doubly degenerate. To prove the degeneracy, we introduce a unitary operator $\hat{\pi}$ defined by

$$\hat{\pi} = \hat{\sigma}_y \exp\left[i\pi \left(\hat{N}_{a_1(1)} + \hat{N}_{a_1(2)} + \hat{N}_{b_1} \right) \right], \tag{2.3}$$

where $\hat{N}_\alpha$ is the number operator of the vibrational quanta of the mode α, and $\hat{\sigma}_y$ the Pauli matrix. $\hat{\pi}$ is analogous to the operators $\mathcal{P}$ of Leung and Kleiner [11] and $\hat{P}$ of

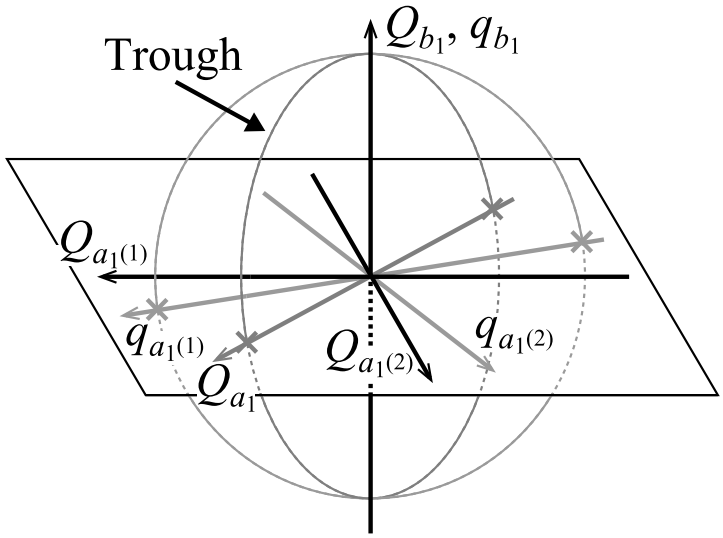

Figure 2.1: Mass-weighted normal coordinates $(Q_{a_1(1)}, Q_{a_1(2)}, Q_{b_1})$, effective coordinates $(q_{a_1(1)}, q_{a_1(2)}, q_{b_1})$, and the trough.

Bersuker and Polinger [1] for the linear $E \otimes e$ Jahn–Teller problem. $\hat{\pi}$ commutes with $\hat{\sigma}_y$ and anticommutes with $\hat{P}_\alpha$, Q_α, $\hat{\sigma}_x$, and $\hat{\sigma}_z$. Thus, $\hat{H}$ and $\hat{\pi}$ commute, $[\hat{H}, \hat{\pi}] = 0$. When $|\Psi\rangle$ is one of the eigenstates of $\hat{H}$, $|\hat{\pi}\Psi\rangle$ is also the eigenstate which belongs to the same eigenenergy of $\hat{H}$. $|\Psi\rangle$ and $|\hat{\pi}\Psi\rangle$ are different from each other because the irreducible representation of $\hat{\pi}$ is b_1. If $|\Psi\rangle$ is $a_1(b_1)$, then $|\hat{\pi}\Psi\rangle$ is $b_1(a_1)$. Thereby, $|\Psi\rangle$ and $|\hat{\pi}\Psi\rangle$ are degenerate eigenstates which are orthogonal to each other. The eigenvalue of $\hat{\pi}$ is ± 1 and the eigenstate is written as $|\Psi_\pm\rangle = (|\Psi_{a_1}\rangle \pm i|\Psi_{b_1}\rangle)/\sqrt{2}$, where $|\Psi_{a_1}\rangle$ and $|\Psi_{b_1}\rangle$ are degenerate vibronic states whose representations are a_1 and b_1, respectively. Therefore, we can regard $\hat{\pi}$ as a parity operator.

The two-fold degeneracy of each vibronic level is lifted in some cases in which some perturbations exist. First, the existence of the conical intersection is necessary for the degeneracy. If we add $\hat{V} = \Delta\hat{\sigma}_z$ (Δ is real) to $\hat{H}$ to remove the conical intersection, the degeneracy of the vibronic state is lost because $[\hat{\pi}, \hat{\sigma}_z] \neq 0$ and the Hamiltonian does not have the parity symmetry. Second, quadratic Jahn–Teller coupling removes the degeneracy. The quadratic coupling is not invariant by the operation $\hat{\pi}$ because $[\hat{\pi}, Q_\alpha Q_\beta] = 0$, $[\hat{\pi}, \hat{\sigma}_x] \neq 0$, and $[\hat{\pi}, \hat{\sigma}_z] \neq 0$. Finally, zero coupling of the a_1' mode in the Hamiltonian of X_3 is necessary. If Eq. (2.1) has a nonzero coupling to the a_1' mode, the Hamiltonian of the isotopomer has a term of $\hat{V} = \sum_i V'_{a_1(i)} Q_{a_1(i)} \hat{\sigma}_0$ which does not commute with $\hat{\pi}$. $V'_{a_1(i)}$ comes from the vibronic coupling to the a_1' mode of X_3, and

$V'_{a_1(i)} \neq V_{a_1(i)}$. Note that the coupling to the totally symmetric mode can be removed by appropriate choice of the reference structure of X_3.

Towards a better understanding of the properties of the vibronic state described above, we derive the ground and low-lying vibronic levels and wavefunctions analytically in the strong coupling limit [12, 13]. Following Ref. [13], we introduce the effective coordinates: two of them, $q_{a_1(1)}$ and q_{b_1}, vibronically couple to the electronic state, and the other one $q_{a_1(2)}$ does not. Then, we use the cylindrical coordinates, $(q_{a_1(1)}, q_{b_1}, q_{a_1(2)}) = (\rho\cos\phi, \rho\sin\phi, z)$. In the strong coupling limit, we use the adiabatic approximation and treat the Hamiltonian for the lower-sheet. Replacing the vibronic state Ψ with $\Phi/\sqrt{\rho}$, the vibronic Hamiltonian for Φ is

$$\begin{aligned}\hat{H}_{\rm LS} &= -\frac{1}{2}\left(\frac{\partial^2}{\partial\rho^2}+\frac{\partial^2}{\partial z^2}+\frac{1}{\rho^2}\frac{\partial^2}{\partial\phi^2}\right)+\frac{\omega_\rho^2}{2}\rho^2+\frac{\omega_z^2}{2}z^2 \\ &- |V_E|\sqrt{\frac{2\delta+3}{3\delta+3}}\rho-\omega_z^2\gamma\rho z\cos\phi+\frac{\omega_z^2}{2}\gamma^2\rho^2\cos^2\phi, \end{aligned} \tag{2.4}$$

where $\delta = (m-m_0)/m_0$, $\gamma = \delta/\sqrt{(3\delta+3)(\delta+3)}$, $\omega_\rho = \omega_E\sqrt{(2\delta+3)/(3\delta+3)}$, $\omega_z = \omega_A\sqrt{(\delta+3)/(2\delta+3)}$, and ω_E and ω_A are the frequencies of the e' and a_1' modes of X_3, respectively. Furthermore, we treat the radial and longitudinal vibrations (ρ, z) and the pseudorotation (ϕ) separately since the former are fast, and the latter is slow.

First, we solve the vibrational state at a fixed ϕ. We divide $\hat{H}_{\rm LS}$ into the Hamiltonian for the harmonic oscillators around $\rho = \rho_0 = |g_E|\sqrt{(3\delta+3)/[\omega_E(2\delta+3)]}$ and $z = 0$, $\hat{H}_{\rm F}^{(0)}$, and last two terms in Eq. (2.4), $\hat{V}_{\rm F}$, where $g_E = V_E/\sqrt{\omega_E^3}$ is the dimensionless constant. When $|g_E\delta| = \epsilon$ is small ($\epsilon \ll 1$), $\hat{V}_{\rm F}$ can be regarded as a perturbation to $\hat{H}_{\rm F}^{(0)}$. Applying the second order perturbation theory, we obtain the ground vibrational level $E_0^{\rm F}(\phi)$ and the ground state $|\psi_0^{\rm F}(\phi)\rangle$ of $\hat{H}_{\rm F}^{(0)}$.

Next, we obtain the pseudorotational state. The rotational Hamiltonian is obtained averaging $\hat{H}_{\rm LS}$ by $|\psi_0^{\rm F}(\phi)\rangle$. Neglecting the terms of $o(\epsilon^2/g_E^2)$ and removing the constants, we obtain the pseudorotational Hamiltonian with a potential:

$$\hat{H}_{\rm rot} = -\frac{1}{2\rho_0^2}\frac{\partial^2}{\partial\phi^2}+\frac{\kappa}{\rho_0^2}\cos 2\phi, \tag{2.5}$$

where $\kappa = -\gamma^2\rho_0^2\omega_\rho\omega_z/[8(\omega_\rho+\omega_z)]$ ($\kappa < 0$). Although there is no barrier in the trough of the vibronic Hamiltonian (2.2), we obtain a warped potential. The warping is a consequence of the mixing of the vibrational states induced by the change of the mass in the kinetic energy.

The eigenvalue problem of $\hat{H}_{\rm rot}$ is equivalent to the Mathieu's equation [14]. The rotational states $\psi^{\rm S}(\phi)$ have to satisfy the boundary condition $\psi^{\rm S}(\phi+2\pi)=-\psi^{\rm S}(\phi)$ to fulfil the single-valuedness of the total vibronic wavefunction. This sign change comes from the Berry phase of the electronic state of the Jahn–Teller system [10]. In this case, each eigenstate is characterized by a half-integer ν, $\psi^{\rm S}_{\nu}$. In addition, each level of $\hat{H}_{\rm rot}$ is doubly degenerate, $E_{\nu}=E_{-\nu}$, which is consistent with the two-fold degeneracy of each vibronic level of Eq. (2.2).

In the case of the linear $E\otimes e$ Jahn–Teller system, the pseudorotational level and its eigenstate are written as $\nu^2/2\rho_0^2$ and $e^{i\nu\phi}$, respectively [1]. The pseudorotational state of the original Jahn–Teller system is delocalized along the trough. On the other hand, for finite ϵ, using the perturbation theory, we obtain corrections for the pseudorotational level,

$$E_{\nu} \;=\; \frac{\nu^2}{2\rho_0^2}+\frac{\kappa^2}{4\rho_0^2(\nu^2-1)}, \tag{2.6}$$

and the eigenfunction which belongs to E_{ν},

$$\psi^{\rm S}_{\nu}(\phi) \;=\; e^{i\nu\phi}\left[1+\frac{|\kappa|}{4}\left(\frac{e^{2i\phi}}{\nu+1}-\frac{e^{-2i\phi}}{\nu-1}\right)\right]. \tag{2.7}$$

The densities of the ground ($|\nu|=1/2$) and first excited ($|\nu|=3/2$) rotational wavefunctions $|\psi^{\rm S}_{\nu}(\phi)|^2$ are concentrated at $\phi=0$, π and $\phi=\pm\pi/2$, respectively. One should note that this localization (kinetic localization) is generated by the modification of the kinetic energy.

Here, we see the role of the Berry phase. In the case of the $E\otimes e$ Jahn–Teller system, if the Berry phase is ignored, $\psi^{\rm S}(\phi+2\pi)=\psi^{\rm S}(\phi)$, the representations of the ground and first excited levels are A and E, respectively [10]. Due to the isotopic substitution, the first excited E level splits. One should note that each level is doubly degenerate when the Berry phase exists. The ground state is written as $1+(|\kappa|\cos 2\phi)/2$. The second term is obtained as a result of the constructive interference of the excited states $e^{\pm i2\phi}$. On the other hand, $e^{i(\nu\pm2)\phi}$ partly cancel each other in Eq. (2.7). Therefore, the localization is quenched by the Berry phase. The first and second excited states are approximately written as $\cos\phi$ and $\sin\phi$, respectively. Therefore, the density of the first excited rotational state has maxima at $\phi=0$ and π, which is the opposite of the correct one.

Next, we consider the effect of the quadratic vibronic coupling. Weak quadratic coupling is written as $\eta\rho_0^2 \cos 3\phi$ [1,2]. We assume that the coupling is the same order as the potential in Eq. (2.5). Owing to the quadratic coupling, one of the minima of the potential of $\hat{H}_{\rm rot}$ is deeper than the other. One of the ground vibronic states is localized around lower minimum and the other around the higher one. Consequently, the degeneracy of the level is lifted.

To confirm our analytical result, we calculated the vibronic states by diagonalizing the Hamiltonian (2.2) numerically. The vibronic basis employed here is a set of the products of the electronic states $|\gamma\rangle$ and vibrational states $|n_{a_1(1)}, n_{a_1(2)}, n_{b_1}\rangle$, $\{|\gamma\rangle|n_{a_1(1)}, n_{a_1(2)}, n_{b_1}\rangle; \gamma = \theta, \epsilon, 0 \leq n_{a_1(1)} + n_{a_1(2)} + n_{b_1} \leq 30\}$. The zero-point vibrational energy is chosen as the zero of energy. Parameters for the calculations are as follows: g_E is varied from 0 to 3 by 0.1, $\omega_E = 1$, $\omega_A = 1.3$, and $\delta = 1$. The ratio ω_A/ω_E is close to those of H_3 (1.26) and Li_3 (1.27) (see Table 2.1). The density of the wavefunction is calculated as $\rho(\mathbf{Q}) = |\langle \mathbf{Q}|\Psi_\pm\rangle|^2$, where $\mathbf{Q} = (Q_{a_1(1)}, Q_{a_1(2)}, Q_{b_1})$.

The vibronic levels of the $E\otimes(a\oplus e)$ Jahn–Teller system (dotted and dashed lines) and the isotopomer (solid lines) are shown in Fig. 2.2. The stabilization energy $E_{\rm JT} = g_E^2\omega_E/2$ is added to each vibronic level. The behavior of the vibronic levels of the isotopomer is similar to that of the Jahn–Teller system. Nonetheless, contrary to the Jahn–Teller system, the vibronic levels of the isotopomer avoid each other because each level is doubly degenerate and the irreducible representations of the degenerate states are a_1 and b_1. The kinetic localization is clearly seen as the increase of g_E. The densities $\rho(\mathbf{Q})$ of the ground and first excited vibronic states on the plane of the trough (Fig. 2.1) at $g_E = 3$ are shown in Fig. 2.3. The densities of the ground and the first excited states are localized around $\phi = 0, \pi$ and $\phi = \pm\pi/2$, respectively. These distributions agree with analytical results.

In order to see the possibility of observation of the isotope effect in molecules, we evaluated the vibronic coupling constants of H_3 and Li_3 (Table 2.1). The coupling constants of X_3 were obtained from the gradient of the adiabatic potential energy surface at the equilibrium geometry of X_3^+. The equilibrium geometries, frequencies, and gradients were obtained performing the density functional calculations (B3LYP/6-311G(d,p)) [15]. The frequencies are scaled by 0.9619 [16].

In both systems, the coupling to the a_1' mode is weaker than that to the e' mode. The vibronic coupling constant for the e' mode is sufficiently strong for the localization.

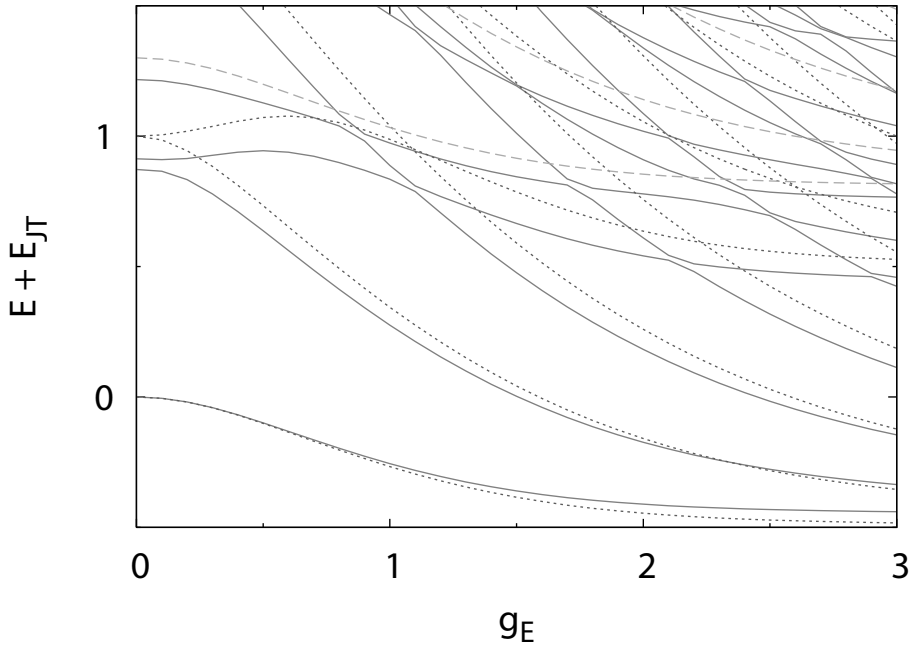

Figure 2.2: Ground and low-lying vibronic levels of X_2Y (solid line) and X_3 (dotted and dashed lines). Dotted and dashed lines indicate the levels of the $E \otimes e$ Jahn–Teller system with zero and one a vibrational excitation, respectively. $E_{\mathrm{JT}} = g_E^2 \omega_E / 2$ is added to each level. g_E is varied from 0 to 3 by 0.1. $\omega_E = 1$, $\omega_A = 1.3$, and $\delta = 1$.

Therefore, the kinetic localization could be observed in the isotopomers of H_3 and Li_3. The shapes of the UV spectra of H_3 and the isotopomers depend on the system [6], which should reflect the structure of the vibronic states. In the case of Li_3, $|\delta|$ is relatively small. However, there are differences in the rovibronic spectra [7], which may be a result of the kinetic localization.

Table 2.1: The absolute values of the dimensionless vibronic coupling constants $g_\Gamma (\Gamma = a_1', e')$ and frequencies (cm^{-1}) of H_3 and Li_3.

	H_3		Li_3	
Irrep.	Freq.	g_Γ	Freq.	g_Γ
E'	2589	2.63	235	2.27
A_1'	3266	1.16	298	0.64

In this chapter, we studied the Jahn–Teller problem of an isotopomer of trimer X_3. Within the linear coupling model, each vibronic level is doubly degenerate because of

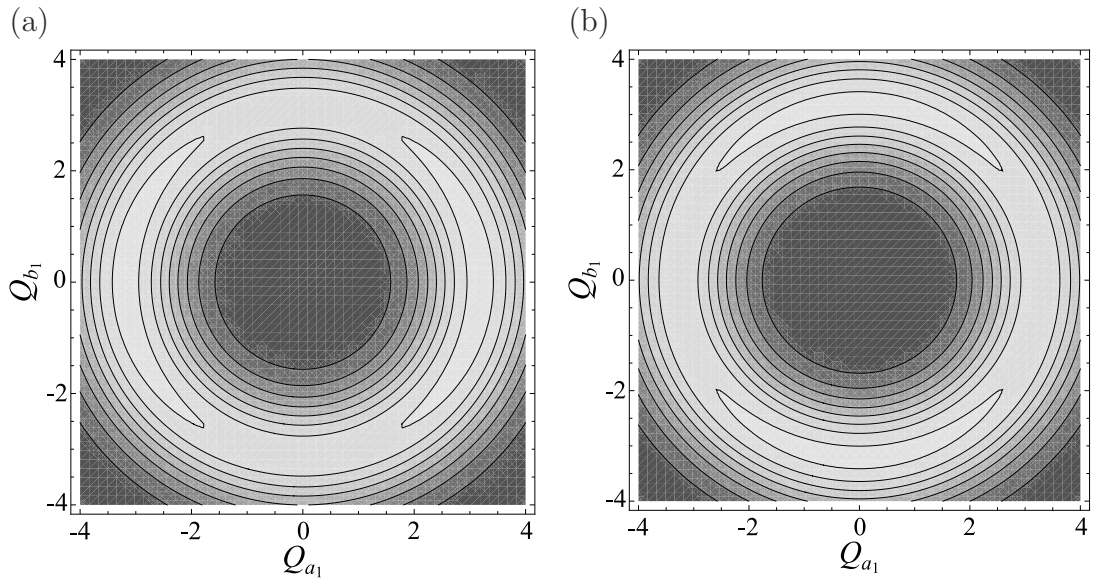

Figure 2.3: The densities of the (a) ground and (b) first excited vibronic states calculated with $g_E = 3$, $\omega_E = 1$, $\omega_A = 1.3$, and $\delta = 1$. The cross section corresponds to the plane of the trough (see Fig. 2.1). The densities of the light gray area is the largest and that of the dark gray the smallest. The values of the smallest, largest, and spacing of the contours are 0.002, 0.016, and 0.002, respectively.

the parity. For the degeneracy, existence of the conical intersection is necessary. In the analytical treatment, we found that the potential for the pseudorotation is warping. Consequently, the vibronic state is localized around the minima (kinetic localization). The degeneracy of the vibronic level and the kinetic localization are confirmed performing the exact diagonalization of the vibronic Hamiltonian. Moreover, with finite quadratic vibronic coupling, the degeneracy of each vibronic level is lifted. The origin of the splitting is explained from view of both the symmetry and the structure of the potential. Density functional calculations supports the possibility of experimental observation of the kinetic localization. Present result and concept could be useful to not only the analysis of the vibronic states of the trimers but also investigations on other dynamic Jahn–Teller systems.

Bibliography

[1] I. B. Bersuker, and V. Z. Polinger, *Vibronic Interactions in Molecules and Crystals* (Springer–VerlagBerlin and Heidelberg, 1989).

[2] I. B. Bersuker, *The Jahn–Teller Effect* (Cambridge University PressCambridge, 2006).

[3] R. G. Lawler, J. R. Bolton, J. R. Fraenkel, and T. H. Brown, J. Am. Chem. Soc. **86**, 520 (1964).

[4] A. Carrington, H. C. Longuet-Higgins, R. E. Moss, and P. F. Todd, Mol. Phys. **9**, 187 (1965).

[5] L. Yu, D. W. Cullin, J. M. Williamson, and T. A. Miller, J. Chem. Phys. **98**, 2682 (1993).

[6] R. Bruckmeier, C. Wunderlich, and F. Figger, Phys. Rev. Lett. **72**, 2550 (1994).

[7] H.-G. Krämer, M. Keil, C. B. Suarez, W. Demtröder, and W. Meyer, Chem. Phys. Lett. **299**, 212 (1999).

[8] H. J. Wörner, and F. Merkt, J. Chem. Phys. **126**, 154304 (2007).

[9] D. G. Melnik, J. Liu, M.-W. Chen, T. A. Miller, and R. F. Curf, J. Chem. Phys. **135**, 094310 (2011).

[10] F. S. Ham, Phys. Rev. Lett. **58**, 725 (1987).

[11] C. H. Leung, and W. H. Kleiner, Phys. Rev. B **10**, 4434 (1974).

[12] M. C. M. O'Brien, Proc. R. Soc. A **281**, 323 (1964).

[13] V. Z. Polinger, and G. I. Bersuker, Phys. Status Solidi (B) **95**, 403 (1979).

[14] F. W. J. Olver, D. W. Lozier, R. f. Boisvert, and C. W. Clark, *NIST Handbook of Mathematical Functions* (Cambridge University PressNew York, 2010).

[15] M. J. Frisch, G. W. Trucks, H. B. Schlegel, G. E. Scuseria, M. A. Robb, J. R. Cheeseman, G. Scalmani, V. Barone, B. Mennucci, G. A. Petersson, H. Nakatsuji, M. Caricato, X. Li, H. P. Hratchian, A. F. Izmaylov, J. Bloino, G. Zheng, J. L. Sonnenberg,

M. Hada, M. Ehara, K. Toyota, R. Fukuda, J. Hasegawa, M. Ishida, T. Nakajima, Y. Honda, O. Kitao, H. Nakai, T. Vreven, J. J. A. Montgomery, J. E. Peralta, F. Ogliaro, M. Bearpark, J. J. Heyd, E. Brothers, K. N. Kudin, V. N. Staroverov, T. Keith, R. Kobayashi, J. Normand, K. Raghavachari, A. Rendell, J. C. Burant, S. S. Iyengar, J. Tomasi, M. Cossi, N. Rega, J. M. Millam, M. Klene, J. E. Knox, J. B. Cross, V. Bakken, C. Adamo, J. Jaramillo, R. Gomperts, R. E. Stratmann, O. Yazyev, A. J. Austin, R. Cammi, C. Pomelli, J. W. Ochterski, R. L. Martin, K. Morokuma, V. G. Zakrzewski, G. A. Voth, P. Salvador, J. J. Dannenberg, S. Dapprich, A. D. Daniels, O. Farkas, J. B. Foresman, J. V. Ortiz, J. Cioslowski, and D. J. Fox, *Gaussian 09, Revision B.01*, Wallingford CT, 2010.

[16] M. P. Andersson, and P. Uvdal, J. Phys. Chem. A **109**, 2937 (2005).

Part II

Vibronic Couplings in Fullerenes

Chapter 1

Vibronic Coupling in C_{60}^{-} Anion Revisited: Precise Derivations from Photoelectron Spectra and DFT Calculations

1.1 Introduction

Much attention has been paid to the Jahn–Teller effect of fullerene (C_{60}) in various electronic states not only because the Jahn–Teller effect is an interesting problem in molecular physics [1] but also because it is expected to play an important role in the mechanism of the superconductivity in alkali-doped fullerides [2]. Thus, the strength of the electron-vibration coupling (vibronic coupling) of C_{60} which characterizes the Jahn–Teller effect has been one of the important topics. The vibronic coupling constants (VCCs) have been estimated experimentally [3–5] and theoretically [6–14].

In the experimental studies of vibronic coupling in fullerene, a landmark is the photoelectron spectroscopy (PES) of C_{60}^{-} in gas phase by Gunnarsson *et al* [3]. As C_{60}^{-} is one of the most studied systems, in addition to this experimental work, computational works have been performed by many authors. However, discrepancy between the coupling constants of the experimental and theoretical works have been reported [3, 11, 12]. The theoretical stabilization energies as estimated by density functional theory (DFT) calculation were always obtained smaller than that derived from the experiment of Gunnarsson

et al. Besides uncertainties intrinsic to the DFT method, whose predictions depend on the used exchange-correlation functional, one should note that the derivation of vibronic coupling constants in Ref. [3] is not perfect either. First, the thermal excitations were not included in the simulation, although the vibrational temperature of C_{60}^- was estimated about 200 K in the experiment. Second, not all vibronic coupling constants have been estimated from the spectrum because of the low resolution. For the same reason, the computed VCCs of totally symmetric modes were used to simulate the PES.

Recently, Wang *et al.* remeasured photoelectron spectra of C_{60}^- [15]. In their experiment, the vibrational temperature of C_{60}^- is between 70 K and 90 K and the resolution is about 16 meV, i.e., much smaller than the resolution of 40 meV in the experiment of Gunnarsson *et al.* Accordingly, the spectrum of Wang *et al.* is narrower and has more structures, therefore, it is expected to yield more reliable coupling constants.

In this work, we simulate the photoelectron spectra of Wang *et al.* [15] and Gunnarsson *et al.* [3] and give new derivations of the VCCs of C_{60}^-. We also compute the VCCs of C_{60}^- using the DFT method and compare them with the experimental values.

1.2 The solution of the Jahn–Teller problem of C_{60}^-

The equilibrium geometry of neutral fullerene is taken as the reference nuclear configuration. At this reference structure, the ground electronic state of C_{60}^- is T_{1u}. According to the selection rule, the T_{1u} electronic state couples with two a_g and eight h_g vibrational modes:

$$\left[T_{1u}^2\right] = a_g \oplus h_g. \tag{1.1}$$

We consider the linear $T_{1u} \otimes (2a_g \oplus 8h_g)$ Jahn–Teller Hamiltonian. The Hamiltonian is written as follows:

$$\begin{aligned} H &= \sum_{i=1}^{2} \left[\frac{1}{2} \left(P_{a_g(i)}^2 + \omega_{a_g(i)}^2 Q_{a_g(i)}^2 + V_{a_g(i)} Q_{a_g(i)} \right) \right] \hat{I} \\ &+ \sum_{\mu=1}^{8} \sum_{m=-2}^{2} \left[\frac{1}{2} \left(P_{h_g(\mu)m}^2 + \omega_{h_g(\mu)}^2 Q_{h_g(\mu)m}^2 \right) \hat{I} + \sqrt{\frac{5}{2}} (-1)^m V_{h_g(\mu)} Q_{h_g(\mu)m} \hat{C}_{-m} \right] \end{aligned} \tag{1.2}$$

where $Q_{\Gamma(\mu)m}$ is the mass-weighted normal coordinate of m element of the $\Gamma(\mu)$ mode ($\Gamma = a_g, h_g$), $P_{\Gamma(\mu)m}$ is the conjugate momentum of the normal coordinate $Q_{\Gamma(\mu)m}$, $\omega_{\Gamma(\mu)}$ is the frequency of the $\Gamma(\mu)$ mode, $V_{\Gamma(\mu)}$ is the VCC of the $\Gamma(\mu)$ mode, and $\hat{I}$ and $\hat{C}_{-m}$

are the 3×3 unit matrix and a matrix whose elements are Clebsch–Gordan coefficients, respectively. The normal modes and frequencies of C_{60} are used for C_{60}^{-} , so the higher vibronic terms which mix the normal modes of fullerene are neglected. As a T_{1u} electronic basis set $\{|m_{\rm el}\rangle; m_{\rm el} = -1, 0, 1\}$ and normal coordinates of the h_g modes $\{Q_{h_g(\mu)m}; m = -2, -1, 0, 1, 2\}$, we use complex basis which transform as spherical harmonics $\{Y_{1m_{\rm el}}; m_{\rm el} = -1, 0, 1\}$ and $\{Y_{2m}; m = -2, -1, 0, 1, 2\}$, respectively, under the rotations [16, 17]. Then $\hat{I}$ and $\hat{C}_{-m}$ are written as [18]

$$
\begin{aligned}
\hat{I} &= \begin{pmatrix} 1 & 0 & 0 \\ 0 & 1 & 0 \\ 0 & 0 & 1 \end{pmatrix}, \quad \hat{C}_{-2} = \begin{pmatrix} 0 & 0 & \sqrt{\frac{3}{5}} \\ 0 & 0 & 0 \\ 0 & 0 & 0 \end{pmatrix}, \\
\hat{C}_{-1} &= \begin{pmatrix} 0 & -\sqrt{\frac{3}{10}} & 0 \\ 0 & 0 & \sqrt{\frac{3}{10}} \\ 0 & 0 & 0 \end{pmatrix}, \quad \hat{C}_{0} = \begin{pmatrix} \frac{1}{\sqrt{10}} & 0 & 0 \\ 0 & \frac{-2}{\sqrt{10}} & 0 \\ 0 & 0 & \frac{1}{\sqrt{10}} \end{pmatrix}, \\
\hat{C}_{1} &= \begin{pmatrix} 0 & 0 & 0 \\ \sqrt{\frac{3}{10}} & 0 & 0 \\ 0 & -\sqrt{\frac{3}{10}} & 0 \end{pmatrix}, \quad \hat{C}_{2} = \begin{pmatrix} 0 & 0 & 0 \\ 0 & 0 & 0 \\ \sqrt{\frac{3}{5}} & 0 & 0 \end{pmatrix}.
\end{aligned} \tag{1.3}
$$

This type of the Jahn–Teller problem was investigated by O'Brien [19] and the vibronic coupling constants defined by her are often used. Thus we introduce the coefficient $\sqrt{5/2}$ in front of the vibronic term to make V_{h_g} the same as O'Brien's coupling constants.

Since the linear $T_{1u} \otimes (2a_g \oplus 8h_g)$ Jahn–Teller Hamiltonian (1.2) commutes with squared vibronic angular momentum $\mathbf{J}$ and the z component of $\mathbf{J}$ [20], the eigenstate of the Hamiltonian (1.2) is the simultaneous eigenstate of the vibronic angular momentum J, the z component of the vibronic angular momentum M, where the vibronic angular momentum $\mathbf{J}$ is the sum of the vibrational angular momentum $\mathbf{L}$ and the "energy spin" $\mathbf{S}$ describing the threefold orbital degeneracy ($S = 1$) [20]. In the case of linear vibronic coupling, the eigenstate of H is the product of the $T_{1u} \otimes (8h_g)$ Jahn–Teller part and the a_g vibrational part. As a vibronic basis a set of the products of electronic states and vibrational states of the a_g and h_g modes is used:

$$
\left\{ |m_{\rm el}\rangle | \cdots \mathbf{n}_\mu \cdots \rangle |v_1 v_2\rangle_{a_g} \right\}, \tag{1.4}
$$

where $\mathbf{n}_\mu$ means a set of vibrational quantum numbers of the $h_g(\mu)$ mode, $\mathbf{n}_\mu = \{n_{\mu m}\}$, v_1, v_2 are vibrational quantum numbers of the $a_g(1)$ mode and the $a_g(2)$ mode respec-

tively. Then the eigenstate $|\Psi_{v_1v_2kJM}\rangle$ of the Hamiltonian (1.2) which belongs to the eigenvalue $\sum_{i=1}^{2}\left[\hbar\omega_{a_g(i)}v_i - V_{a_g(i)}^2/(2\omega_{a_g(i)}^2)\right] + E_{kJ}$ is represented as a linear combination of the vibronic basis with constants $C^{\rm JT}_{m_{\rm el},\mathbf{n}_1\cdots\mathbf{n}_8;kJM}$.

$$
\begin{aligned}
|\Psi_{v_1v_2kJM}\rangle &= \sum_{m_{\rm el}=-1}^{1}\sum_{\mathbf{n}_1}\cdots\sum_{\mathbf{n}_8}|m_{\rm el}\rangle|\mathbf{n}_1\cdots\mathbf{n}_8\rangle C^{\rm JT}_{m_{\rm el},\mathbf{n}_1\cdots\mathbf{n}_8;kJM} \\
&\times \sum_{v_1'=0}^{\infty}\sum_{v_2'=0}^{\infty}|v_1'v_2'\rangle_{a_g} S_{v_1'v_1}(g_{a_g(1)})S_{v_2'v_2}(g_{a_g(2)}),
\end{aligned}
\tag{1.5}
$$

where E_{kJ} is an eigenvalue of the $T_{1u}\otimes(8h_g)$ Jahn–Teller Hamiltonian, k distinguishes energy levels with the same J and M, the dimensionless VCC of the $\Gamma(\mu)$ mode $g_{\Gamma(\mu)}$ ($\Gamma = a_g, h_g$) is defined as

$$
g_{\Gamma(\mu)} = \frac{V_{\Gamma(\mu)}}{\sqrt{\hbar\omega_{\Gamma(\mu)}^3}},
\tag{1.6}
$$

the Franck–Condon factor of the a_g mode $S_{v'v}(g)$ is written as

$$
S_{v'v}(g) = \sqrt{\frac{v'!v!}{2^{v'-v}}}e^{-\frac{1}{4}g^2}\sum_{l=l_{\rm min}}^{v}\left(-\frac{1}{2}\right)^l\frac{g^{2l+v'-v}}{l!(v-l)!(v'-v+l)!},
\tag{1.7}
$$

$l_{\rm min} = 0$ for $v \le v'$, and $l_{\rm min} = v - v'$ for $v > v'$. The origin of the energy is the lowest energy of C_{60}^- without vibronic couplings.

To obtain the vibronic states, we diagonalize the linear $T_{1u}\otimes 8h_g$ Jahn–Teller Hamiltonian numerically using Lanczos method. We use a truncated vibronic basis set,

$$
\left\{|m_{\rm el}\rangle|\cdots\mathbf{n}_\mu\cdots\rangle; \sum_{\mu=1}^{8}\sum_{m=-2}^{2}n_{\mu m} \le N\right\},
\tag{1.8}
$$

where N is the maximum number of the vibrational excitations in the vibronic basis set (1.8). We treat the vibronic states which Js are from 0 to 7. Frequencies $\omega_{a_g(i)}, \omega_{h_g(\mu)}$ are taken from the experimental frequencies of Raman scattering in solid state C_{60} [21].

Lastly, we introduce stabilization energies which we use to show our results. The stabilization energy of each mode is defined as

$$
E_{s,i} = \frac{V_{a_g(i)}^2}{2\omega_{a_g(i)}^2},
\tag{1.9}
$$

$$
E_{{\rm JT},\mu} = \frac{V_{h_g(\mu)}^2}{2\omega_{h_g(\mu)}^2},
\tag{1.10}
$$

and the total stabilization energies of the a_g modes and h_g modes are

$$E_s = \sum_{i=1}^{2} E_{s,i}, \tag{1.11}$$

$$E_{\mathrm{JT}} = \sum_{\mu=1}^{8} E_{\mathrm{JT},\mu}. \tag{1.12}$$

They represent the depth of the potential energy surface from the energy of undistorted fullerene monoanion.

1.3 Simulation of the photoelectron spectrum

The photoelectron spectrum is simulated within the sudden approximation [22]. We assume that each C_{60}^{-} is in a thermal equilibrium state, hence we use a Boltzmann's distribution to calculate the statistical weight. With these assumptions, the intensity of the transition which appears at the binding energy $\hbar\Omega$ is written as follows:

$$\begin{aligned} I(\Omega) \propto & \sum_{k,J} \sum_{v_1',v_2'} p_{v_1'} p_{v_2'} p_{kJ} \sum_{m_{\mathrm{el}}=-1}^{1} \left| C^{\mathrm{JT}}_{m_{\mathrm{el}},\mathbf{n}_1\cdots\mathbf{n}_8;kJ0} S_{v_1'v_1}(g_{a_g(1)}) S_{v_2'v_2}(g_{a_g(2)}) \right|^2 \\ & \times \delta\left[\frac{E_0 + E_s - E_{kJ}}{\hbar} + \sum_{\mu=1}^{8} \sum_{m=-2}^{2} \omega_{h_g(\mu)} n_{\mu m} + \sum_{i=1}^{2} \omega_{a_g(i)} (v_i - v_i') - \Omega \right], \end{aligned} \tag{1.13}$$

where p_{v_i} and p_{kJ} are the statistical weights of the $a_{g(i)}$ mode and the Jahn–Teller part, respectively,

$$p_{v_i} = \frac{1}{Z_{a_g}} \exp\left(-\hbar\omega_{a_g(i)} v_i \beta\right), \tag{1.14}$$

$$p_{kJ} = \frac{2J+1}{Z_{\mathrm{JT}}} \exp\left(-E_{kJ}\beta\right), \tag{1.15}$$

Z_{a_g} and Z_{JT} are corresponding statistical sums, and E_0 is the gap between the ground electronic energies of C_{60} and C_{60}^{-}. The envelope function is represented by using the Gaussian function with the standard deviation σ:

$$F(\Omega) = \int_{-\infty}^{\infty} I(\Omega') \exp\left[\frac{-(\Omega - \Omega')^2}{2\sigma^2} \right] d\Omega'. \tag{1.16}$$

For a decent simulation of experimental PES one should include in Eq. (1.16), in principle, also the contributions from the rotational spectrum of C_{60}^{-}. However, due to a large momentum of inertia of fullerene and restrictive selection rules for the transitions between different rotational levels [23] our estimations gave an expected enlargement of

the transition band of only several wave numbers. This is negligible compared the full width at half maximum (FWHM) given by the envelope function (1.16).

To evaluate the agreement between the simulated spectrum and the experimental spectrum, we calculate the residual of theoretical spectrum $F_{\mathrm{calc}}(\Omega)$ and the experimental spectrum $F_{\mathrm{exp}}(\Omega)$. The residual R is defined by the equation:

$$R = \min_{f,\Omega_{\mathrm{shift}}} \left\{ \frac{\sum_{i=0}^{M} \left[F_{\mathrm{calc}}(\Omega_i) - f F_{\mathrm{exp}}(\Omega_i - \Omega_{\mathrm{shift}})\right]^2}{\sum_{j=0}^{M} F_{\mathrm{calc}}^2(\Omega_j)} \right\}, \tag{1.17}$$

where f is the parameter to vary the height, Ω_{shift} is the parameter to shift the experimental spectrum, Ω_i is a sampling point. The minimum and maximum of Ω_i is Ω_{min} and Ω_{max}, and the gap between adjacent sampling points $\Delta\Omega$ is constant. Then M is represented as $M = (\Omega_{\mathrm{max}} - \Omega_{\mathrm{min}})/\Delta\Omega$ and $\Omega_i = \Omega_{\mathrm{min}} + i\Delta\Omega$. In the calculation of the residual R, Ω_{min}, Ω_{max}, and $\Delta\Omega$ are -200 cm^{-1}, 1600 cm^{-1}, and 0.5 cm^{-1} respectively. We avoid the truncation of the zero phonon line of Gunnarsson *et al.* [3]. VCCs are varied in order to make R as small as possible within the accuracy of the experiment. The accuracy is determined from the range of the vibrational temperature of C_{60}^- in the experiment of Wang *et al.* [15]. In their experiment, the vibrational temperature is between 70 K and 90 K. Although the shapes of the simulated spectra at 70 K and 90 K are different from each other, we cannot distinguish them from the experiment of Wang *et al.* In terms of the residual R, the difference between R at 70 K and R at 90 K is practically indistinguishable.

1.4 DFT calculation of vibronic coupling constants

The linear vibronic coupling constant of the $a_g(i)$ mode is a diagonal matrix element of the first derivative of the electronic Hamiltonian with respect to the normal coordinate at the reference geometry [20].

$$V_{a_g(i)} = \langle\psi| \left(\frac{\partial H_{\mathrm{el}}(\mathbf{R})}{\partial Q_{a_g(i)}} \right)_{\mathbf{R}_0} |\psi\rangle, \tag{1.18}$$

where ψ is the ground electronic state. By applying the Hellmann–Feynman theorem [24] to Eq. (1.18) and then transforming it into the formula with the vibrational vector, we obtain

$$V_{a_g(i)} = \left(\frac{\partial E(\mathbf{R})}{\partial Q_{a_g(i)}} \right)_{\mathbf{R}_0} \tag{1.19}$$

$$= \sum_{A=1}^{60} \left(\frac{\partial E(\mathbf{R})}{\partial \mathbf{R}_A} \right)_{\mathbf{R}_0} \cdot \frac{\mathbf{u}_A^{a_g(i)}}{\sqrt{M}}, \tag{1.20}$$

where A indicates a carbon atom in C_{60}, $\mathbf{R}_A$ is the Cartesian coordinate of A, $\mathbf{R}$ is the set of all $\mathbf{R}_A$, $H_{\rm el}(\mathbf{R})$ is the electronic Hamiltonian at the structure $\mathbf{R}$, $\mathbf{R}_0$ is the reference nuclear configuration, $E(\mathbf{R})$ is the ground electronic energy $\langle\psi|H_{\rm el}(\mathbf{R})|\psi\rangle$, M is the mass of carbon atom, $\mathbf{u}_A^{a_g(i)}$ is the vibrational vector of the $a_g(i)$ mode. Similarly, absolute value of the coupling constant of the $h_g(\mu)$ mode is written as

$$V_{h_g(\mu)} = \sqrt{\sum_{m=-2}^{2}\left(\frac{\partial E(\mathbf{R})}{\partial Q_{h_g(\mu)m}}\right)^2_{\mathbf{R}_0}} \tag{1.21}$$

$$= \sqrt{\sum_{m=-2}^{2}\left[\sum_{A=1}^{60}\left(\frac{\partial E(\mathbf{R})}{\partial \mathbf{R}_A}\right)_{\mathbf{R}_0}\cdot\frac{\mathbf{u}_A^{h_g(\mu)m}}{\sqrt{M}}\right]^2}. \tag{1.22}$$

The equilibrium geometry $\mathbf{R}_0$, the vibrational vectors $\mathbf{u}^{a_g(i)}$, $\mathbf{u}^{h_g(\mu)m}$, and the gradient of the electronic energy $(\partial E(\mathbf{R})/\partial\mathbf{R}_A)_{\mathbf{R}_0}$, entering the Eqs. (1.20) and (1.22), are obtained from *ab initio* calculations. Note that the vibronic coupling constants (1.19), (1.21) are not equal to the gradients of the frontier levels (see Appendix).

We compute the VCCs of C_{60}^- using the DFT method. As exchange-correlation functional, the hybrid functional of Becke [25] (B3LYP) is used. To find VCCs which are close to the experimental results the fraction of the Hartree–Fock exchange energy are varied from the original fraction 20% to 30% by 5%. We use the triple zeta basis sets, 6-311G(d), 6-311+G(d), and cc-pVTZ.

The structure optimization and the calculation of the vibrational modes are performed for the neutral fullerene. The electronic wavefunction of C_{60}^- are obtained from the variational calculation of an unrestricted Slater determinant. As far as the method based on the single determinant is used, the spatial symmetry of the wavefunction is broken and the degeneracy of the singly occupied degenerate level is lifted [26, 27]. However, in the case of the cyclopentadienyl radical, it was demonstrated that the splitting of the total electronic energies estimated by the unrestricted B3LYP method is only 0.4 meV [26, 27]. It is expected that the splitting of the T_{1u} ground electronic energies of C_{60}^- is tiny and the symmetry of the electronic state may not be broken significantly. Thus we treat the wavefunction as a T_{1u} wavefunction. We calculate the energy gradient $\partial E(\mathbf{R})/\partial\mathbf{R}_A|_{\mathbf{R}\to\mathbf{R}_0}$ with the coupled perturbed Kohn–Sham method. In the calculation of the dimensionless VCCs (1.6) and the stabilization energies (1.10), we use the experimental frequencies [21]. To compute electronic structures we use the Gaussian 03 program [28].

1.5 Derivation of the vibronic coupling constants of a_g modes from the structures of C_{60} and C_{60}^-

We also derive the stabilization energies of the a_g modes from the experimental bond lengths of C_{60} and C_{60}^-. The structures of C_{60} and C_{60}^- with I_h symmetry are determined by the C-C bond lengths of the edges between two hexagons (6:6) and a hexagon and pentagon (6:5). We use average 6:6 and 6:5 C-C bond lengths of TDAE-C_{60} for C_{60}^- and fullerite for C_{60}. The data of TDAE-C_{60} are obtained from the results of X-ray diffraction at 7K by Narymbetov *et al.* [29] and at 25K and 90K by Fujiwara *et al.* [30]. The average bond lengths of fullerite are taken from the results of neutron diffraction at 5K by David *et al.* [31] and X-ray diffraction at 110K by Bürgi *et al.* [32]. To remove the thermal expansion of the C-C bond lengths, we use sets of bond lengths of C_{60} and C_{60}^- which are measured at close temperature. That is, the bond lengths of C_{60} measured at 5K is used with the bond lengths of C_{60}^- measured at 7K and 25K, and the bond lengths of C_{60} at 110K is used with the bond lengths of C_{60}^- at 90K. The vibronic coupling constants of the a_g modes $V_{a_g(i)} (i = 1, 2)$ are obtained from the equation

$$V_{a_g(i)} = -\sum_{A=1}^{60} (\mathbf{R}_A - \mathbf{R}_{0,A}) \cdot \frac{\mathbf{u}_A^{a_g(i)}}{\sqrt{M}}. \tag{1.23}$$

To perform the calculation, we use the vibrational vector defined in the calculations with the B3LYP method and the cc-pVTZ basis.

1.6 Results and discussion

1.6.1 Simulation of the PES of Wang *et al.*

We simulate the photoelectron spectrum measured by Wang *et al.* [15] at 70 K. The basis set in Eq. (1.5) includes up to 6 vibrational excitations ($N = 6$). The experimental and simulated spectra are shown in Fig. 1.1. The transition between the ground states of C_{60}^- and C_{60} (the 0–0 line) [33] is chosen as the origin of these spectra. From the spectrum of Wang *et al.*, we obtain several sets of VCCs listed as (1), (2), and (3) in Tables 1.1 and 1.2. We extract $\sigma = 80$ cm^{-1} by fitting the FWHM of the 0–0 line (188 cm^{-1}). The increase or decrease of the σ makes the agreement between the simulated and experimental spectra worse.

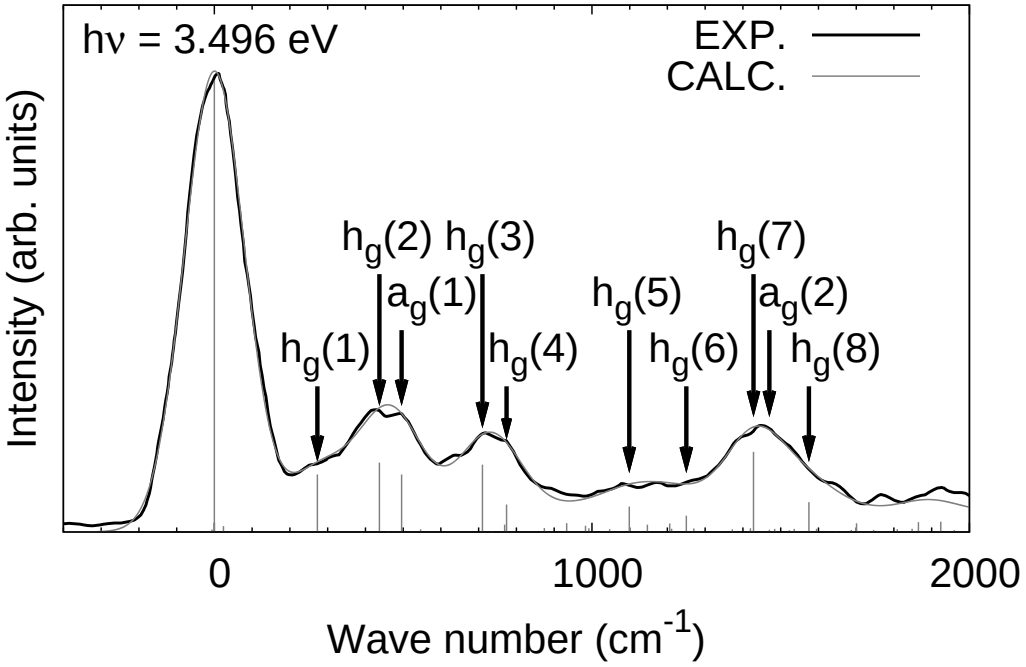

Figure 1.1: The photoelectron spectrum measured by Wang *et al.* (black line) and the simulated spectrum (gray line). The simulation is performed at 70 K with $\sigma = 80$ cm^{-1}.

Table 1.1: Absolute values of dimensionless vibronic coupling constants obtained in the present chapter. (1),(2),and (3) are derived from the PES of Wang *et al.* [15]. (4),(5) are derived from the PES of Gunnarsson *et al.* [3]. The percentage 20 %, 25 %, and 30 % indicate fractions of the Hartree–Fock exact exchange taken in the exchange-correlation functional.

	Frequency	PES					B3LYP					
	(cm^{-1})	Wang		Gunnarsson			6-311G(d)			6-311+G(d)	cc-pVTZ	
							20 %	25 %	30 %	20 %	20 %	25 %
		(1)	(2)	(3)	(4)	(5)	(6)	(7)	(8)	(9)	(10)	(11)
$a_g(1)$	496	0.505	0.505	0.500	0.141	0.505	0.287	0.272	0.269	0.346	0.289	0.286
$a_g(2)$	1470	0.100	0.200	0.300	0.424	0.200	0.415	0.445	0.460	0.455	0.430	0.450
$h_g(1)$	273	0.500	0.500	0.490	0.740	0.820	0.436	0.437	0.444	0.426	0.442	0.452
$h_g(2)$	437	0.525	0.520	0.515	0.860	0.690	0.498	0.504	0.508	0.479	0.498	0.494
$h_g(3)$	710	0.465	0.460	0.455	0.390	0.350	0.418	0.464	0.476	0.412	0.403	0.414
$h_g(4)$	774	0.310	0.310	0.300	0.490	0.490	0.259	0.241	0.243	0.252	0.273	0.283
$h_g(5)$	1099	0.285	0.280	0.280	0.320	0.300	0.211	0.233	0.241	0.211	0.212	0.217
$h_g(6)$	1250	0.220	0.230	0.235	0.190	0.160	0.126	0.169	0.178	0.126	0.125	0.124
$h_g(7)$	1428	0.490	0.470	0.435	0.320	0.430	0.398	0.414	0.433	0.392	0.398	0.415
$h_g(8)$	1575	0.295	0.285	0.260	0.350	0.410	0.338	0.335	0.345	0.330	0.333	0.343

Table 1.2: Stabilization energies (meV) obtained in the present chapter. (1),(2),and (3) are derived from the PES of Wang *et al.* [15]. (4),(5) are derived from the PES of Gunnarsson *et al.* [3]. The percentage 20 %, 25 %, and 30 % indicate fractions of the Hartree–Fock exact exchange taken in the exchange-correlation functional.

	Frequency	PES					B3LYP					
	(cm^{-1})	Wang			Gunnarsson		6-311G(d)			6-311+G(d)	cc-pVTZ	
							20 %	25 %	30 %	20 %	20 %	25 %
		(1)	(2)	(3)	(4)	(5)	(6)	(7)	(8)	(9)	(10)	(11)
$a_g(1)$	496	7.8	7.8	7.7	0.6	7.8	2.5	2.3	2.2	3.7	2.6	2.5
$a_g(2)$	1470	0.9	3.6	8.2	16.4	3.6	15.7	18.0	19.3	18.9	16.9	18.5
$h_g(1)$	273	4.2	4.2	4.1	9.3	11.4	3.2	3.2	3.3	3.1	3.3	3.5
$h_g(2)$	437	7.5	7.3	7.2	20.0	12.9	6.7	6.9	7.0	6.2	6.7	6.6
$h_g(3)$	710	9.5	9.3	9.1	6.7	5.4	7.7	9.5	10.0	7.5	7.2	7.6
$h_g(4)$	774	4.6	4.6	4.3	11.5	11.5	3.2	2.8	2.8	3.1	3.6	3.8
$h_g(5)$	1099	5.5	5.3	5.3	7.0	6.1	3.0	3.7	4.0	3.0	3.0	3.2
$h_g(6)$	1250	3.9	4.1	4.3	2.8	2.0	1.2	2.2	2.5	1.2	1.2	1.2
$h_g(7)$	1428	21.3	19.6	16.8	9.1	16.4	14.0	15.2	16.6	13.6	14.0	15.2
$h_g(8)$	1575	8.5	7.9	6.6	12.0	16.4	11.2	11.0	11.6	10.7	10.9	11.5
E_s		8.7	11.4	15.9	17.0	11.4	18.2	20.3	21.5	22.6	19.5	21.0
E_{JT}		65.0	62.3	57.7	78.4	82.1	50.2	54.4	57.8	48.4	49.9	52.6
$E_s + E_{\mathrm{JT}}$		73.7	73.7	73.6	95.4	93.5	68.4	74.7	79.3	71.0	69.4	73.6

To assess the thermal population of the excited vibronic states, we calculate statistical weights of the excited Jahn–Teller levels p_{kJ} at 70 K and 90 K. The vibronic levels are obtained using the set of VCCs (1). In the calculation of the distribution function $Z_{\rm JT}$, we include all excited vibronic levels whose weights are larger than 10^{-7}. The computed weights are shown in Table 1.3. Although these statistical weights are computed using the set (1), rest of the sets of VCCs (2), (3) give similar results. The statistical weights of the ground vibronic level at 70 K and 90 K are more than 90 %. This indicates that the transition from the ground vibronic level is dominant in the PES of Wang *et al.* We focus, therefore, on the ground vibronic level to discuss the effect of the size of the basis (1.8) on the calculated vibronic states. The ground vibronic level is -962.65 cm^{-1} when we use the basis set with $N = 5$. Compared with the gap between the ground and first excited vibronic levels with $J = 1$, the change of the ground vibronic level due to the increase of the size of the vibronic basis set is only about 0.07 %. Therefore, we regard our basis set as large enough to simulate the spectrum of Wang *et al.*

Table 1.3: The lowest vibronic levels (cm^{-1}) and the statistical weights p_{kJ} (%) at 70 K and 90 K. J is the magnitude of the vibronic angular momentum. To calculate the vibronic levels, the set of VCCs (1) in Table 1.1 is used.

Level	J	Energy	Weight	
			70 K	90 K
1	1	-962.85	97.75	92.48
2	3	-713.97	1.37	4.04
3	2	-683.40	0.52	1.77
4	1	-672.75	0.25	0.90
Sum			99.89	99.19

The differences between several sets of VCCs are in the constants of $a_g(2)$, $h_g(7)$, and $h_g(8)$ modes. If we increase the dimensionless VCC (the stabilization energy) of the $a_g(2)$ mode from 0.1 to 0.3 (0.9 to 8.2 meV) and at the same time decrease the dimensionless VCCs of $h_g(7), h_g(8)$ modes, the shape of the PES does not vary significantly (see Fig. 1.2). This is due to a poor resolution of the peaks of $a_g(2), h_g(7)$, and $h_g(8)$ modes and essentially the same problem arose in the analysis of Gunnarsson *et al.* [3]. In the latter

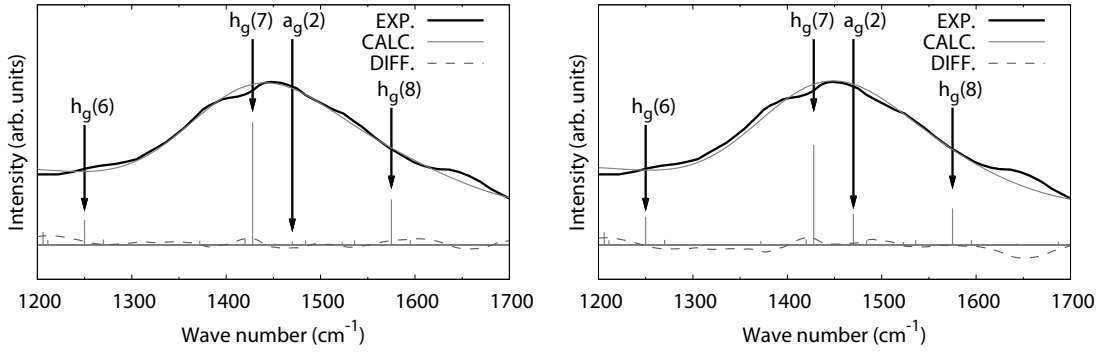

Figure 1.2: The peak of the photoelectron spectra due to $a_g(2)$, $h_g(7)$, and $h_g(8)$ modes. The black line indicates the experimental spectrum of Wang *et al.* [15], the gray solid line indicates the simulated spectrum, and the dashed line indicates the difference between the experimental and simulated spectra. The left of the two spectra is simulated using the VCCs (1) and the right one is simulated using the VCCs (3) from Table 1.1. The simulation is performed at 70 K with $N = 6$ and $\sigma = 80$ cm^{-1}.

Table 1.4: Residuals of the experimental and simulated spectra. The calculation of the residual is performed for all sets of VCCs in Table 1.1 at 70 K and 90 K.

	Set (1)		Set (2)		Set (3)	
	70 K	90 K	70 K	90 K	70 K	90 K
$R \times 10^{-4}$	8.35	8.07	8.41	8.16	8.76	8.41

case, the stabilization energy of $a_g(2)$ is varied from 0 to 45 meV, i.e., in a range larger than ours. Owing to the narrow peaks of the spectrum of Wang *et al.*, we can derive the VCCs with less ambiguity.

We compute the residuals (1.17) of the experimental and the simulated spectra for all sets of VCCs at 70 K and 90 K. The values are shown in Table 1.4. The differences of the residuals of the different sets of VCCs are almost within the ambiguity of the vibrational temperature. Therefore, we conclude that these sets of VCCs cannot be distinguished from the experiment of Wang *et al.*

Although we obtain several sets of VCCs, the stabilization energies $E_s + E_{\mathrm{JT}}$ are similar to each other (see (1), (2), and (3) in Table 1.2). On the other hand, present stabilization energies are smaller than the stabilization energy of Gunnarsson *et al.* [3] by 30 % (see

Table 1.5), i.e., the Jahn–Teller coupling is weaker than previously expected. We find that the distributions of $E_{s,i}$ and $E_{\mathrm{JT},\mu}$ also differ from each other (Tables 1.2, 1.5). In Ref. [3], the stabilization energy of $h_g(2)$ was found the strongest, while our results show that the strongest is the stabilization energy of $h_g(7)$.

Hands *et al.* estimated the Jahn–Teller stabilization energy E_{JT} of 57.94 meV within the single-mode $T_{1u}\otimes h_g$ Jahn–Teller model from the visible and near-infrared spectrum [5]. The present Jahn–Teller stabilization energy agrees well with their value.

Table 1.5: Comparison between the obtained stabilization energies of C_{60}^{-} with previous results (meV). (3) and (10) are given in Tables 1.2. The stabilization energies of the a_g modes are not reported by Varma *et al.* [6] and Saito [12].

	Freq.	PES		LDA		GGA	MNDO	B3LYP		
	(cm^{-1})	(3)	Gun [3]	Man [11]	Bre [10]	Fre [13]	Var [6]	Sai [12]	Laf [14]	(10)
$a_g(1)$	496	7.7	0.6	0.2	1.5	1.5	-	-	1.8	2.6
$a_g(2)$	1470	8.2	16.4	2.7	9.0	11.0	-	-	16.4	16.9
$h_g(1)$	273	4.1	11.4	2.7	6.0	2.8	1.8	3.6	3.5	3.3
$h_g(2)$	437	7.2	24.0	6.3	15.6	7.0	0.6	6.6	6.5	6.7
$h_g(3)$	710	9.1	7.8	5.5	6.6	6.1	0.6	6.6	7.1	7.2
$h_g(4)$	774	4.3	10.8	2.4	3.0	2.4	0.0	3.0	3.1	3.6
$h_g(5)$	1099	5.3	7.2	2.6	3.6	2.6	3.6	3.0	3.0	3.0
$h_g(6)$	1250	4.3	3.0	1.5	1.8	1.9	0.0	1.8	1.3	1.2
$h_g(7)$	1428	16.8	10.2	9.0	9.6	9.0	20.4	13.2	13.8	14.0
$h_g(8)$	1575	6.6	13.8	8.2	4.8	8.8	6.6	10.2	10.6	10.9
E_s		15.9	17.0	2.9	10.5	12.5	-	-	18.2	19.5
E_{JT}		57.7	88.2	38.2	51.0	40.6	33.6	48.0	48.9	49.9
$E_s + E_{\mathrm{JT}}$		73.6	105.2	41.1	61.5	53.1	-	-	67.1	69.4

1.6.2 Simulation of the PES of Gunnarsson *et al.*

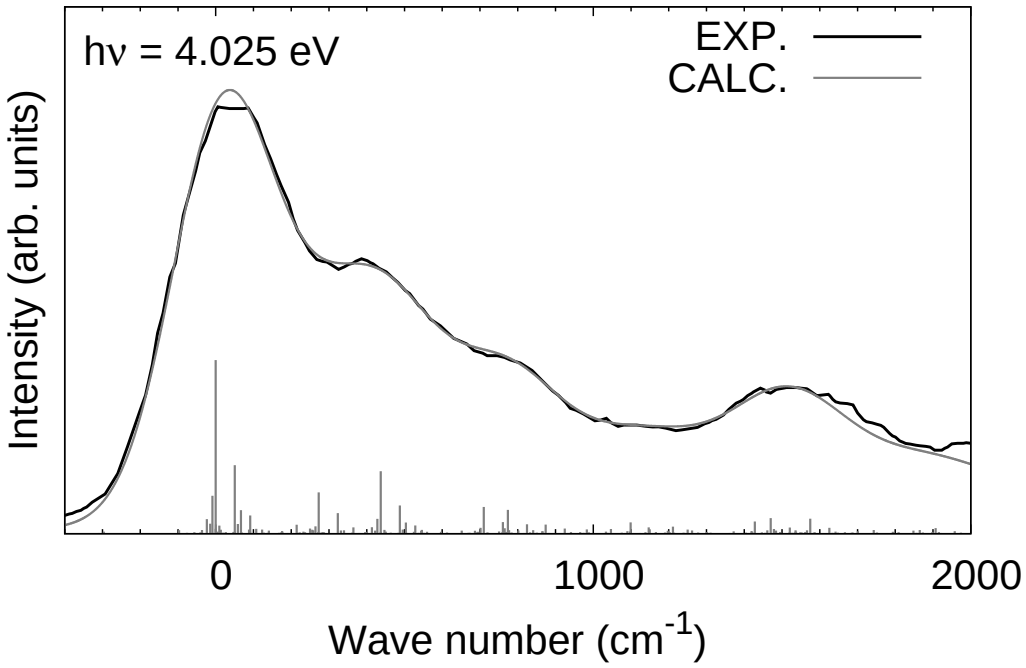

Figure 1.3: The experimental photoelectron spectrum measured by Gunnarsson *et al.* [3] (black line) and the simulated spectrum (gray line). The simulation is performed at 200 K with $\sigma = 120$ cm^{-1}.

As a preliminary calculation, we compute the vibronic levels using the data from Ref. [3], that is, the same VCCs and the same size of the vibronic basis ($N = 5$). The statistical weight of the ground state at 200 K is obtained ca. 39 %. This result indicates that not only the ground level but also excited levels must be considered in order to simulate the spectrum of Gunnarsson *et al.* [3].

We simulate this spectrum at 200 K with the FWHM of 283 cm^{-1} ($\sigma = 120$ cm^{-1}). The size of the vibronic basis set is $N = 7$. The experimental and the simulated spectra are shown in Fig. 1.3. As was mentioned also by Gunnarsson *et al.* [3], we obtain several sets of VCCs that give close stabilization energies. These sets of dimensionless VCCs and stabilization energies are (4), (5) in Table 1.1 and 1.2 respectively. In comparison with the original stabilization energy of Gunnarsson *et al.*, present stabilization energies are smaller by 10 meV. However, stabilization energies are still larger than those obtained from the spectrum of Wang *et al.* by 20 meV. The inconsistencies of these VCCs come from the difference between the shapes of the spectra of Wang *et al.* and Gunnarsson *et*

al., due to different vibrational temperature and resolution.

Simulating the spectrum of Gunnarsson *et al.*, we encounter two problems. First, the spectrum is too broad and, second, the vibrational temperature is too high. In fact, the statistical weights of the ground vibronic level at 200 K are about 37 % in both cases (see Table 1.6), hence, we must consider many excited vibronic states. To represent the excited vibronic states with enough accuracy, we expect that the vibronic basis must be larger than the present one. Furthermore, as the vibrational temperature is further increased, the weight of each vibronic level and the shape of the spectrum varies easily. Although the range of the vibrational temperature is not reported, we increased the temperature by 20 K which is the uncertainty range of vibrational temperature in the case of Wang *et al.* [15]. The statistical weights of the ground vibronic level decreased from ca. 37 % to ca. 31 % with this increase of the temperature. This change of the weight affects the shape of the spectrum. Therefore it is difficult to perform an accurate simulation and to estimate VCCs from the spectrum of Gunnarsson *et al.*

Given better the experimental conditions of Wang *et al.* [15] allowing for more accurate simulations, we may conclude that the VCCs extracted from these experiments should be considered more reliable than those obtained by Gunnarsson *et al.* [3].

1.6.3 DFT calculations of the vibronic coupling constants

We compute the vibronic coupling constants of C_{60}^- using the DFT method described in Sec. 1.4. It is well known that in the high-symmetry geometry the occupied level moves upwards in energy relative to the empty levels when pure DFT functional is used [34]. However in our case the situation is opposite (the occupied level is the lowest one) because of the Hartree–Fock exchange contribution contained in the B3LYP functional. The splitting between the t_{1u} Kohn–Sham levels are about 1 eV (see Table 1.7) and the variations of the total electronic energies for different occupation schemes of t_{1u} orbitals are less than 0.2 meV. Moreover, the vibronic coupling constants do not depend on the choice of the electronic states significantly. The variation of the total stabilization energy is ca. 1 meV. The dimensionless VCCs and the stabilization energies are shown in Table 1.1 and 1.2. Although we use several basis sets, the VCCs do not depend on the basis set significantly. On the other hand, the VCCs vary with the increase of the fraction of the Hartree–Fock exchange energy in the exchange-correlation functional. Increasing this

Table 1.6: The computed vibronic levels (cm^{-1}) and statistical weights p_{kJ} (%) using the sets of VCCs (4), (5) which are derived from the experimental spectrum of Gunnarsson *et al.* [3]. The statistical weights are calculated at 200K.

Level	Set (4)			Set (5)		
	J	Energy	Weight 200 K	J	Energy	Weight 200 K
1	1	-1067.6	36.56	1	-1134.4	37.00
2	3	-845.2	17.22	3	-914.7	17.77
3	2	-785.9	8.03	2	-850.2	7.98
4	1	-771.3	4.34	1	-829.9	4.14
5	3	-697.5	5.95	3	-742.5	5.15
6	2	-616.0	2.37	2	-687.8	2.48
7	5	-613.1	5.10	5	-685.5	5.37
8	1	-590.0	1.18	1	-667.0	1.28
9	3	-580.3	2.56	3	-650.1	2.65
10	2	-535.1	1.32	2	-595.0	1.27
11	4	-531.4	2.06	4	-594.0	2.02
12	1	-525.4	0.74	1	-590.6	0.74
13	3	-485.2	1.29	3	-543.5	1.23
14	5	-464.8	1.75	5	-515.2	1.58
15	4	-445.7	1.11	4	-495.6	1.00
16	2	-404.6	0.52	2	-456.7	0.47
17	7	-371.4	1.22	7	-446.6	1.31
18	4	-362.7	0.61	3	-436.7	0.57
19	3	-362.1	0.53	4	-432.7	0.63
20	5	-339.6	0.71	5	-414.8	0.77
21	0	-330.5	0.06	0	-400.2	0.06
22	2	-317.4	0.28	4	-388.3	0.46
23	4	-316.8	0.44	2	-387.9	0.29
24	1	-291.3	0.14	1	-357.6	0.14
25	6	-275.4	0.53	6	-336.5	0.52
Sum			96.62			96.88

Table 1.7: The splitting between the lifted one-electron t_{1u} levels $\Delta\epsilon$ (meV).

	6-311G(d)			6-311+G(d)	cc-pVTZ	
	20 %	25 %	30 %	20 %	20 %	25 %
$\Delta\epsilon$	691	874	1059	686	693	876

fraction leads to larger VCCs and stabilization energies. We find that the stabilization energies of high frequency modes, $a_g(2), h_g(7)$, and $h_g(8)$ are the strongest. Compared with other DFT calculations, we may conclude that the stabilization energies of a_g modes agree well with the previous calculations, while the present stabilization energy $E_s + E_{\rm JT}$ is larger than the previous results.

In comparison with present simulation of the experimental PES, the DFT calculations with the energy functionals including fractions of 20 % and 25 % of the Hartree–Fock exchange energy give close values. Although the stabilization energy $E_s+E_{\rm JT}$ obtained using the original B3LYP functional is slightly smaller than the experimental value, the result obtained with it is also close to the experimental one. The distribution of the computed stabilization energy of each h_g mode $E_{{\rm JT},\mu}$ qualitatively agrees with the experimental results. The stabilization energy of the $h_g(7)$ mode is obtained smaller and that of the $h_g(8)$ mode is obtained larger than the experimental values. The slight difference between theoretical and experimental results should originate from still inaccurately computed vibrational vectors. Indeed, it was shown that a small mixing of the vibrational vectors in fullerene affects the values of VCCs significantly [3]. Besides the present computational results, the LDA calculation by Manini *et al.* [11], the GGA calculation by Frederiksen *et al.* [13], and the B3LYP calculation by Saito [12] and Laflamme Janssen [14] give similar relative values for the coupling constants of h_g modes as the present simulations of PES of Wang *et al.* [15]. On the other hand, the LDA and GGA calculations give smaller absolute values of the VCCs and of the total stabilization energies than the presently obtained. The LDA calculation of Breda *et al.* [10] gives the distribution of relative strengths of VCCs which is similar to the results of Gunnarsson *et al.* and do not agree with the values derived here from PES of Wang *et al.* Varma *et al.* [6] computed VCCs using MNDO method, however, the distribution of the stabilization energies is different from the present simulations of experiment and the theoretical values obtained here.

Table 1.8: Stabilization energies (meV) derived from the experimental C-C bond lengths of C_{60} and C_{60}^-.

	Frequency (cm^{-1})	Stabilization energies of a_g modes (meV)				
		(3)	(10)	Narymbetov[1]	Fujiwara[1]	Fujiwara[2]
				7K	25K	90K
$a_g(1)$	496	7.7	2.6	8.0	0.1	58.8
$a_g(2)$	1470	8.2	16.9	0.0	7.5	7.0

On the contrary, the theoretical stabilization energy of the $a_g(1)$ mode is too small and that of the $a_g(2)$ mode is too large compared to $E_{s,i}$ derived from experiment (Tables 1.1, 1.2). To find the correct order of the corresponding VCCs, we derive the coupling constants of the a_g modes from the experimental bond lengths as described in Sect. 1.5. The obtained stabilization energies $E_{s,i}$ are shown in Table 1.8. Unfortunately, as we can see, $E_{s,i}$ depend very strongly on the set of the C-C bond lengths, thus we cannot draw a conclusion about their relative strength. This comes from the fact that we use the structural data measured by different techniques (X-ray and neutron scattering) on different systems (TDAE-C_{60} and fullerite) for C_{60}^- and C_{60}, respectively. In both cases, fullerenes should be deformed due to the environment compared with the free C_{60} molecule. The distortions caused by the crystal fields of C_{60} in TDAE-C_{60} and fullerite are different from each other. Furthermore, the expected changes in the bond lengths in C_{60} and C_{60}^- are within the experimental accuracy of the structural data. Thus, the origin of the discrepancy of the relative strength of VCCs of the a_g modes between the simulations and DFT calculations remains unclear.

Note that although the values of $E_{s,i}$ are different from the experimental results, their sum, as well as, the distribution of $E_{\mathrm{JT},\mu}$ and $E_s + E_{\mathrm{JT}}$ are close to the experimental values. Therefore, we may conclude that the present theoretical method gives improved values of vibronic coupling constants.

1.7 Conclusion

In this chapter, we simulated the PES of Wang *et al.* and derived the vibronic coupling constants of C_{60}^{-}. We obtain several sets of VCCs, because the frequencies of $a_g(2)$, $h_g(7)$, and $h_g(8)$ modes are close to each other. Considering the ambiguity of the vibrational temperature in the experiment, these sets of VCCs cannot be distinguished. Thus, to obtain more accurate coupling constants, it is desired to perform an observation of a PES of C_{60}^{-} in still better experimental conditions. Although we find several sets of VCCs from the spectrum, the stabilization energies are similar to each other. In comparison with the total stabilization energy derived by Gunnarsson *et al.* [3], our value is smaller by 30 %. We also calculated the VCCs using the DFT method. Even though the experimental and theoretical orders of $E_{s,i}$ disagree with each other, the distribution of $E_{\mathrm{JT},\mu}$ and the total stabilization energy $E_s + E_{\mathrm{JT}}$ agrees well with the experimental values. Thus we may conclude that the problem of the discrepancy between the experimental and calculated coupling constants, persistent in the previous studies, is basically solved in the present chapter. As an extension of the present chapter we expect that the theoretical approach used here could be successfully applied for the calculation of VCC of C_{60}^{n-} anions in A_nC_{60} fullerides as well as of their multiplet splitting parameters.

Appendix: Vibronic coupling constants and the gradient of Kohn–Sham levels

The total energy $E(\mathbf{R})$ in the DFT is written as follows:

$$\begin{aligned} E(\mathbf{R}) &= \sum_{\mu\Gamma\gamma} \epsilon_{\mu\Gamma\gamma}(\mathbf{R}) - \frac{1}{2}\int d\mathbf{r}\int d\mathbf{r}' \frac{n(\mathbf{r};\mathbf{R})n(\mathbf{r}';\mathbf{R})}{|\mathbf{r}-\mathbf{r}'|} \\ &+ E_{xc}\left[n(\mathbf{r};\mathbf{R})\right] - \int d\mathbf{r} n(\mathbf{r};\mathbf{R}) V_{xc}(\mathbf{r};\mathbf{R}) + V_{nn}(\mathbf{R}), \end{aligned} \tag{1.24}$$

where $\Gamma\gamma$ is the irreducible representation of the Kohn–Sham orbital, μ is the quantum number other than $\Gamma\gamma$, $\epsilon_{\mu\Gamma\gamma}$ is the Kohn–Sham level, $\sum_{\mu\Gamma\gamma}$ is taken over occupied levels, $n(\mathbf{r};\mathbf{R})$ is the ground electronic density, $E_{xc}\left[n(\mathbf{r};\mathbf{R})\right]$ is the exchange-correlation energy functional, $V_{xc}(\mathbf{r},\mathbf{R})$ is the exchange-correlation potential, and $V_{nn}(\mathbf{R})$ is the Coulomb

potential energy between nuclei. The vibronic coupling constant of $\Gamma'\gamma'$ mode is

$$\begin{aligned} V_{\Gamma'\gamma'} &= \sum_{\mu\Gamma\gamma} \left(\frac{\partial \epsilon_{\mu\Gamma\gamma}(\mathbf{R})}{\partial Q_{\Gamma'\gamma'}} \right)_{\mathbf{R}_0} - \int d\mathbf{r} \left(\frac{\partial n(\mathbf{r};\mathbf{R})}{\partial Q_{\Gamma'\gamma'}} \right)_{\mathbf{R}_0} \int d\mathbf{r}' \frac{n(\mathbf{r}';\mathbf{R})}{|\mathbf{r}-\mathbf{r}'|} \\ &- \int d\mathbf{r} n(\mathbf{r};\mathbf{R}) \left(\frac{\partial V_{xc}(\mathbf{r};\mathbf{R})}{\partial Q_{\Gamma'\gamma'}} \right)_{\mathbf{R}_0} + \left(\frac{\partial V_{nn}(\mathbf{R})}{\partial Q_{\Gamma'\gamma'}} \right)_{\mathbf{R}_0}. \end{aligned} \tag{1.25}$$

For the totally symmetric modes, all the derivatives in the right-hand side of Eq. (1.25) are not zero. For the Jahn–Teller active modes, the sum of the gradient of the completely occupied Kohn–Sham levels belonging to the same Γ is zero due to the symmetry reasons, and the gradient of the Coulomb potential between the nuclei is zero also because of the symmetry. However, the second and third terms which include the derivative of $n(\mathbf{r};\mathbf{R})$ and $V_{xc}(\mathbf{r};\mathbf{R})$ with respect to $Q_{\Gamma'\gamma'}$, respectively, are nonzero because $n(\mathbf{r};\mathbf{R})$ is not a totally symmetric function. Therefore, in general, the vibronic coupling constant is not equal to the gradient of the frontier Kohn–Sham level.

Bibliography

[1] C. C. Chancey, and M. C. M. O'Brien, *The Jahn–Teller Effect in C_{60} and other Icosahedral Complexes* (Princeton University PressPrinceton, 1997).

[2] O. Gunnarsson, *Alkali-Doped Fullerides: Narrow-Band Solids with Unusual Properties* (World ScientificSingapore, 2004).

[3] O. Gunnarsson, H. Handschuh, P. S. Bechthold, B. Kessler, G. Ganteför, and W. Eberhardt, Phys. Rev. Lett. **74**, 1875 (1995).

[4] J. Winter, and H. Kuzmany, Phys. Rev. B **53**, 655 (1996).

[5] I. D. Hands, J. L. Dunn, C. A. Bates, M. J. Hope, S. R. Meech, and D. L. Andrews, Phys. Rev. B **77**, 115445 (2008).

[6] C. M. Varma, J. Zaanen, and K. Raghavachari, Science **254**, 989 (1991).

[7] M. Schluter, M. Lannoo, M. Needels, G. A. Baraff, and D. Tománek, Phys. Rev. Lett. **68**, 526 (1992).

[8] J. C. R. Faulhaber, D. Y. K. Ko, and P. R. Briddon, Phys. Rev. B **48**, 661 (1993).

[9] V. P. Antropov, O. Gunnarsson, and A. I. Liechtenstein, Phys. Rev. B **48**, 7651 (1993).

[10] N. Breda, R. A. Broglia, G. Colò, H. E. Roman, F. Alasia, G. Onida, V. Ponomarev, and E. Vigezzi, Chem. Phys. Lett. **286**, 350 (1998).

[11] N. Manini, A. D. Carso, M. Fabrizio, and E. Tosatti, Philos. Mag. B **81**, 793 (2001).

[12] M. Saito, Phys. Rev. B **65**, 220508(R) (2002).

[13] T. Frederiksen, K. J. Franke, A. Arnau, G. Schulze, J. I. Pascual, and N. Lorente, Phys. Rev. B **78**, 233401 (2008).

[14] J. Laflamme Janssen, M. Côté, S. G. Louie, and M. L. Cohen, Phys. Rev. B **81**, 073106 (2010).

[15] X. B. Wang, H. K. Woo, and L. S. Wang, J. Chem. Phys. **123**, 051106 (2005).

[16] M. C. M. O'Brien, J. Phys. C: Solid St. Phys. **4**, 2524 (1971).

[17] A. Auerbach, N. Manini, and E. Tosatti, Phys. Rev. B **49**, 12998 (1994).

[18] A. R. Edmonds, *Angular Momentum in Quantum Mechanics* (Princeton University PressPrinceton, 1974).

[19] M. C. M. O'Brien, Phys. Rev. **187**, 407 (1969).

[20] I. B. Bersuker, and V. Z. Polinger, *Vibronic Interactions in Molecules and Crystals* (Springer–VerlagBerlin and Heidelberg, 1989).

[21] D. S. Bethune, G. Meijer, W. C. Tang, H. J. Rosen, W. G. Golden, H. Seki, C. A. Brown, and M. S. de Vries, Chem. Phys. Lett. **179**, 181 (1991).

[22] L. Hedin, and S. Lundqvist, in *Solid State Physics*, edited by H. Ehrenreich, D. Turnbull, and F. Seitz (Academic PressNew York, 1969), Vol. 23, p. 1.

[23] M. S. Child, and H. G. Longuet-Higgins, Phil. Trans. R. Soc. A **254**, 259 (1961).

[24] R. P. Feynman, Phys. Rev. **56**, 340 (1939).

[25] A. D. Becke, J. Chem. Phys. **98**, 5648 (1993).

[26] T. Sato, K. Tokunaga, and K. Tanaka, J. Chem. Phys. **124**, 024314 (2006).

[27] T. Sato, K. Tokunaga, N. Iwahara, K. Shizu, and K. Tanaka, in *The Jahn–Teller Effect: Fundamentals and Implications for Physics and Chemistry*, edited by H. Köppel, D. R. Yarkony, and H. Barentzen (Springer–VerlagBerlin and Heidelberg, 2009), p. 99.

[28] M. J. Frisch, G. W. Trucks, H. B. Schlegel, G. E. Scuseria, M. A. Robb, J. R. Cheeseman, J. A. Montgomery, Jr., T. Vreven, K. N. Kudin, J. C. Burant, J. M. Millam, S. S. Iyengar, J. Tomasi, V. Barone, B. Mennucci, M. Cossi, G. Scalmani, N. Rega, G. A. Petersson, H. Nakatsuji, M. Hada, M. Ehara, K. Toyota, R. Fukuda, J. Hasegawa, M. Ishida, T. Nakajima, Y. Honda, O. Kitao, H. Nakai, M. Klene, X. Li, J. E. Knox, H. P. Hratchian, J. B. Cross, V. Bakken, C. Adamo, J. Jaramillo, R. Gomperts, R. E. Stratmann, O. Yazyev, A. J. Austin, R. Cammi, C. Pomelli, J. W. Ochterski, P. Y. Ayala, K. Morokuma, G. A. Voth, P. Salvador, J. J. Dannenberg, V. G. Zakrzewski, S. Dapprich, A. D. Daniels, M. C. Strain, O. Farkas, D. K. Malick, A. D. Rabuck, K. Raghavachari, J. B. Foresman, J. V. Ortiz, Q. Cui, A. G. Baboul, S. Clifford, J. Cioslowski, B. B. Stefanov, G. Liu, A. Liashenko, P. Piskorz, I. Komaromi, R. L. Martin, D. J. Fox, T. Keith, M. A. Al-Laham, C. Y. Peng, A. Nanayakkara, M. Challacombe, P. M. W. Gill, B. Johnson, W. Chen, M. W. Wong, C. Gonzalez, and J. A. Pople, *GAUSSIAN 03, Revision D.02*, Wallingford, CT, 2004.

[29] B. Narymbetov, H. Kobayashi, M. Tokumoto, A. Omerzu, and D. Mihailovic, Chem. Commun. 1511 (1999).

[30] M. Fujiwara, T. Kambe, and K. Oshima, Phys. Rev. B **71**, 174424 (2005).

[31] W. I. F. David, R. M. Ibberson, J. C. Matthewman, K. Prassides, T. J. S. Dennis, J. P. Hare, H. W. Kroto, R. Tayloa, and D. R. M. Walton, Nature (London) **353**, 147 (1991).

[32] H. B. Bürgi, E. Blanc, D. Schwarzenbach, S. Z. Liu, Y. J. Lu, and M. Kappes, Angew. Chem. Int. Ed. Engl. **31**, 640 (1992).

[33] Actually this line contains contributions also from temperature populated excited vibronic levels of C_{60}^- to some excited vibrational levels of C_{60}. However in the present case their contribution to the 0–0 line is very small.

[34] R. Bruyndonckx, C. Daul, P. T. Manoharan, and E. Deiss, Inorg. Chem. **36**, 4251 (1997).

Chapter 2

Effect of Coulomb Interactions on the Vibronic Couplings in C_{60}^{-}

2.1 Introduction

The vibronic coupling (electron-vibration coupling) [1–3] in C_{60}^{-} anion has been investigated extensively [4–14] because the coupling is not only a fundamental interaction to characterize the Jahn–Teller effect in C_{60}^{-} [3] but also important to discuss the mechanism of the superconductivity of alkali-doped fullerides [15]. Reliable vibronic coupling constants (VCC) are required in solid state physics of the fullerides. However, vibronic couplings obtained from the photoelectron spectrum [5] have been larger than theoretical evaluations [4, 10–14]. Among the intramolecular electron-phonon couplings, Gunnarsson *et al.* have concluded that the coupling to the bending $h_g(2)$ mode is the strongest from the experiment [5]. On the other hand, many theoretical works have suggested that the couplings to the stretching $h_g(7)$ and $h_g(8)$ modes are the strongest [4,10–14]. Among the investigations on the vibronic couplings in C_{60}^{-}, some authors [4, 8, 9] have explained the order of the VCCs. However, the strongest coupling mode is still controversial. Therefore, both the agreement between experimental and theoretical VCCs of C_{60}^{-} and physical picture of the couplings are crucial to understand the vibronic couplings.

Recently, we have estimated the VCCs in C_{60}^{-} performing the exact diagonalization of a dynamic multimode Jahn-Teller Hamiltonian with the totally symmetric a_{1g} modes [16] to fit the experimental photoelectron spectrum (PES) of C_{60}^{-} measured by Wang *et al.* [17], and evaluated the VCCs using the density-functional theory (DFT) calculations [16]. It

has been found that our experimental and theoretical VCCs agree well with each other. Our experimental and theoretical results show that the $h_g(7)$ and $h_g(8)$ have strong VCCs, while the coupling to the $h_g(2)$ mode is weak. In this study, we employ a concept of vibronic coupling density (VCD) [18,19], to elucidate this order of the vibronic couplings. The VCD whose integral over a 3D space yields a VCC is defined from the electronic and vibrational structures. Since the VCD is a function of the position $\mathbf{r}$ in a molecule, it provides a local picture of the vibronic coupling. Employing the VCD analysis, we have succeeded in designing for novel carrier-transporting materials [20,21]. Furthermore, with the use of the VCD analysis, we have revealed a crucial role of the Coulomb interaction in the VCCs of hole-transporting molecules such as TPD and TPF [22,23]. In this chapter, we apply the VCD analysis to the VCCs of C_{60}^-, to explain the order of the vibronic couplings.

2.2 Theory

2.2.1 Vibronic coupling constant

As a reference system, the neutral C_{60} in its equilibrium geometry $\mathbf{R}_0$ with I_h symmetry was adopted as in Ref. [16]. We use the convention of the molecular orientation by Boyle and Parker [24] (Fig. 2.1). The irreducible representation of the ground electronic state

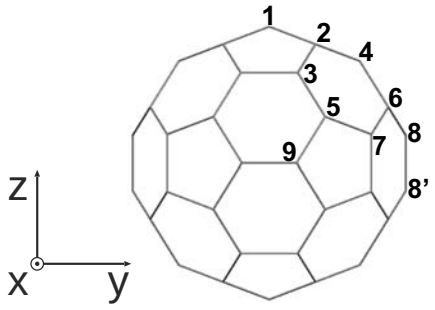

Figure 2.1: The orientation and the atomic labelling of C_{60}.

of C_{60}^- is T_{1u}. From the selection rule, the ground electronic state couples to two a_g and

eight h_g modes. The VCCs of C_{60}^- for the $\Gamma(\mu)$ modes ($\Gamma = a_g, h_g$) are defined by [25]

$$V_{a_g(i)} = \left\langle \Psi_{T_{1u}\lambda} \left| \left(\frac{\partial \hat{H}}{\partial Q_{a_g(i)}} \right)_{\mathbf{R}_0} \right| \Psi_{T_{1u}\lambda} \right\rangle, \tag{2.1}$$

$$V_{h_g(\mu)} = \left\langle \Psi_{T_{1u}z} \left| \left(\frac{\partial \hat{H}}{\partial Q_{h_g(\mu)\theta}} \right)_{\mathbf{R}_0} \right| \Psi_{T_{1u}z} \right\rangle, \tag{2.2}$$

where $\hat{H}$ is the electronic Hamiltonian which includes the Coulomb potential between nuclei, $|\Psi_{T_{1u}\lambda}\rangle$ ($\lambda = x, y, z$) the electronic ground state of C_{60}^- at the geometry of the reference system $\mathbf{R}_0$, and $Q_{\Gamma(\mu)\gamma}$ the normal coordinates of the neutral C_{60} for the $\Gamma(\mu)\gamma$ mode ($\Gamma\gamma = a_g, h_g\theta, h_g\epsilon, h_g\xi, h_g\eta, h_g\zeta$). Among the three electronic states $\lambda = x, y, z$, we choose the $T_{1u}z$ electronic state because the electronic state couples only to the $h_g\theta$ modes [3]. Hereafter we will present results for the $T_{1u}z$ electronic state and the $h_g\theta$ vibrational modes. The phase of the a_g and $h_g\theta$ modes are chosen so that the VCCs are negative. Applying the Hellmann–Feynman theorem, we obtain

$$V_{a_g(i)} = \sum_{A=1}^{60} \left(\frac{\partial E(\mathbf{R})}{\partial \mathbf{R}_A} \right)_{\mathbf{R}_0} \cdot \frac{\mathbf{u}_A^{a_g(i)}}{\sqrt{M}}, \tag{2.3}$$

$$V_{h_g(\mu)} = \sum_{A=1}^{60} \left(\frac{\partial E(\mathbf{R})}{\partial \mathbf{R}_A} \right)_{\mathbf{R}_0} \cdot \frac{\mathbf{u}_A^{h_g(\mu)\theta}}{\sqrt{M}}, \tag{2.4}$$

where $E(\mathbf{R}) = \langle \Psi_{T_{1u}z} | \hat{H} | \Psi_{T_{1u}z} \rangle$, A denotes an atom in C_{60}, $\mathbf{R}_A$ the Cartesian coordinates of the atom A, $\mathbf{R}$ the set of all coordinates of $\mathbf{R}_A$, $\mathbf{u}_A^{\Gamma(\mu)\gamma}$ the displacement of the atom A of the mass-weighted $\Gamma\gamma$ vibrational vector, M the mass of carbon. For the calculation of the VCCs, we used Eqs. (2.3) and (2.4). The VCCs are decomposed into couplings for the atoms

$$V_{a_g(i),A} = \left(\frac{\partial E(\mathbf{R})}{\partial \mathbf{R}_A} \right)_{\mathbf{R}_0} \cdot \frac{\mathbf{u}_A^{a_g(i)}}{\sqrt{M}}, \tag{2.5}$$

$$V_{h_g(\mu),A} = \left(\frac{\partial E(\mathbf{R})}{\partial \mathbf{R}_A} \right)_{\mathbf{R}_0} \cdot \frac{\mathbf{u}_A^{h_g(\mu)\theta}}{\sqrt{M}}. \tag{2.6}$$

We call $V_{a_g(i),A}$ and $V_{h_g(\mu),A}$ atomic vibronic coupling constants (AVCC).

Instead of the VCC, $V_{h_g(\mu)}$, an electron-vibration coupling constant $\lambda_{h_g(\mu)}$ is often used [26]. The electron-phonon couplings to the $h_g(\mu)$ modes $\lambda_{h_g(\mu)}$ are defined by

$$\frac{\lambda_{h_g(\mu)}}{n(0)} = \frac{5V_{h_g(\mu)}^2}{6\omega_{h_g(\mu)}^2}, \tag{2.7}$$

where $n(0)$ is the density of states per molecule per spin at the Fermi level, and $\omega_{h_g(\mu)}$ is the frequency.

Note that Eq. (2.4) is slightly different from the formula that we used in Ref. [16]. In the previous chapter, we used Eq. (2.8) to evaluate the VCCs for the h_g modes.

$$V'_{h_g(\mu)} = \sqrt{\sum_{\gamma} \left[\left(\frac{\partial E(\mathbf{R})}{\partial \mathbf{R}_A} \right)_{\mathbf{R}_0} \cdot \frac{\mathbf{u}_A^{h_g(\mu)\gamma}}{\sqrt{M}} \right]^2}. \tag{2.8}$$

Eq. (2.8) and Eq. (2.4) give the same result as long as the symmetries of both the wavefunction and the vibrational modes are kept. Since unrestricted wavefunction with slightly broken symmetry is employed (see Sec. 2.3) , the couplings to vibrational modes other than θ components are not zero. We found that the difference between couplings calculated using Eq. (2.8) and (2.4) are close to each other. The difference of VCCs between the two methods is less than 0.3 % of the present VCCs.

2.2.2 Vibronic coupling density

The VCCs can be rewritten as the integral form using electronic and vibrational structures [18, 19]. For the h_g modes, the VCCs are written as

$$V_{h_g(\mu)} = \int d^3\mathbf{r} \eta_{h_g(\mu)}(\mathbf{r}). \tag{2.9}$$

The vibronic coupling density (VCD) $\eta_{h_g(\mu)}$ is defined by the product of the electron density difference $\Delta\rho$ and the potential derivative $v_{h_g(\mu)}$:

$$\eta_{h_g(\mu)}(\mathbf{r}) = \Delta\rho(\mathbf{r}) \times v_{h_g(\mu)}(\mathbf{r}), \tag{2.10}$$

where the electron density difference $\Delta\rho$ is the difference between the electron density ρ of C_{60}^- and the electron density ρ_0 of C_{60} :

$$\Delta\rho(\mathbf{r}) = \rho(\mathbf{r}) - \rho_0(\mathbf{r}). \tag{2.11}$$

The potential derivative $v_{h_g(\mu)}$ is the derivative of the one-electron potential $u(\mathbf{r};\mathbf{R})$ acting on a single electron from all the nuclei of C_{60} with respect to $Q_{h_g(\mu)\theta}$:

$$v_{h_g(\mu)}(\mathbf{r}) = \left(\frac{\partial u(\mathbf{r};\mathbf{R})}{\partial Q_{h_g(\mu)\theta}} \right)_{\mathbf{R}_0}, \tag{2.12}$$

$$= \sum_{A=1}^{60} \frac{-Z(\mathbf{r} - \mathbf{R}_{0,A})}{|\mathbf{r} - \mathbf{R}_{0,A}|^3} \cdot \frac{\mathbf{u}_A^{h_g(\mu)\theta}}{\sqrt{M}}, \tag{2.13}$$

where u is

$$u(\mathbf{r};\mathbf{R}) = \sum_{A=1}^{60} \frac{-Z}{|\mathbf{r} - \mathbf{R}_A|}, \tag{2.14}$$

where $Z = 6$, the atomic number of carbon atom. From the VCD, we obtain a local picture of the vibronic coupling constant.

2.2.3 Contribution of each orbital to the electron density difference

Within the Kohn–Sham method, $\Delta\rho$ is written as follows:

$$\Delta\rho(\mathbf{r}) = \sum_{\nu\Lambda\lambda\sigma} \left(N_{\Lambda(\nu)\lambda\sigma} \psi^2_{\Lambda(\nu)\lambda\sigma}(\mathbf{r}) - N_{0,\Lambda(\nu)\lambda\sigma} \psi^2_{0,\Lambda(\nu)\lambda}(\mathbf{r}) \right), \tag{2.15}$$

where $\{\psi_{\Lambda(\nu)\lambda\sigma}\}$ is a set of Kohn–Sham orbitals of the C_{60}^- anion, $\{\psi_{0,\Lambda(\nu)\lambda}\}$ a set of the orbitals of the neutral C_{60}, Λ the irreducible representations, λ the components of Λ, σ the z component of the electron spin, ν the quantum number except for Λ, λ, and σ, and $N_{\Lambda(\nu)\lambda\sigma}$ and $N_{0,\Lambda(\nu)\lambda\sigma}$ the occupation numbers of the orbitals $\psi_{\Lambda(\mu)\lambda\sigma}$ and $\psi_{0,\Lambda(\mu)\lambda}$, respectively. The Kohn–Sham orbitals are chosen to be real. In order to evaluate the contribution of each orbital to the electron density difference, we expand $\Delta\rho$ in terms of $\{\psi_{0,\Lambda(\nu)\lambda}\}$:

$$\begin{aligned}
\Delta\rho(\mathbf{r}) &= \sum_{\nu\Lambda\lambda\sigma} A(\Lambda(\nu)\lambda\sigma) \psi^2_{0,\Lambda(\nu)\lambda}(\mathbf{r}) \\
&+ \sum_{\nu\Lambda\lambda\nu'\Lambda'\lambda'\sigma} B(\Lambda(\nu)\lambda\Lambda'(\nu')\lambda'\sigma) \psi_{0,\Lambda(\nu)\lambda}(\mathbf{r}) \psi_{0,\Lambda'(\nu')\lambda'}(\mathbf{r}), \qquad (2.16) \\
A(\Lambda(\nu)\lambda\sigma) &= \sum_{\bar{\nu}\bar{\Lambda}\bar{\lambda}} N_{\bar{\Lambda}(\bar{\nu})\bar{\lambda}\sigma} \langle \psi_{0,\Lambda(\nu)\lambda} | \psi_{\bar{\Lambda}(\bar{\nu})\bar{\lambda}\sigma} \rangle^2 - N_{0,\Lambda(\nu)\lambda\sigma}, \qquad (2.17) \\
B(\Lambda(\nu)\lambda\Lambda'(\nu')\lambda'\sigma) &= \sum_{\bar{\nu}\bar{\Lambda}\bar{\lambda}} N_{\bar{\Lambda}(\bar{\nu})\bar{\lambda}\sigma} \langle \psi_{0,\Lambda(\nu)\lambda} | \psi_{\bar{\Lambda}(\bar{\nu})\bar{\lambda}\sigma} \rangle \langle \psi_{0,\Lambda'(\nu')\lambda'} | \psi_{\bar{\Lambda}(\bar{\nu})\bar{\lambda}\sigma} \rangle. \qquad (2.18)
\end{aligned}$$

2.3 Method of calculation

To obtain the electronic states, the equilibrium geometry $\mathbf{R}_0$, and the vibrational modes, density-functional theory (DFT) calculations were performed. In the DFT calculations, we employed the hybrid functional B3LYP [27] with a triple-zeta basis set 6-311G(d). The gradients of $E(\mathbf{R})$ were calculated analytically for both a symmetrized wavefunction $|\Psi^{\mathrm{S}}_{T_{1u}z}\rangle$ and a symmetry-broken wavefunction $|\Psi^{\mathrm{BS}}_{T_{1u}z}\rangle$ which comes from the z component of the T_{1u} state. The vibrational modes employed are symmetrized. For the DFT calculations, we used GAUSSIAN 09 [28]. The VCCs and VCDs were calculated using our code.

2.4 Results and discussion

2.4.1 Calculation of the vibronic coupling constants

Experimental [5,16] and present theoretical vibronic coupling constants (VCCs) are shown in Table 2.1. Present theoretical couplings with the symmetry-broken wavefunction $|\Psi^{\rm BS}_{T_{1u}z}\rangle$ (Table 2.1, BS) are in line with our experimental ones [16]. On the other hand, in comparison with the experimental VCCs, some of the VCCs calculated with the symmetrized wavefunction $|\Psi^{\rm S}_{T_{1u}z}\rangle$ (Table 2.1, S) are qualitatively different; the VCC for the $h_g(4)$ mode is overestimated and VCCs for the $h_g(5)$, $h_g(6)$, and $h_g(7)$ are underestimated. This discrepancy occurs because the orbital relaxation is not fully included. We will discuss this issue later. Hereafter, we concentrate on the VCCs calculated with the symmetry-broken electronic wavefunction $|\Psi^{\rm BS}_{T_{1u}z}\rangle$ and analyze them.

Next we compare our VCCs with the Gunnarssons' result. The theoretical VCCs to the stretching $h_g(7)$ and $h_g(8)$ modes (the $h_g(8)$ mode is shown in Fig. 2.2) are as large as those of Gunnarsson *et al.* On the other hand, our vibronic coupling to the bending $h_g(2)$ mode (Fig. 2.2) is almost the half of theirs. Moreover, in terms of the electron-phonon coupling (2.7), the coupling constant for the $h_g(2)$ mode (11 meV) is about one quarter of that estimated by Gunnarsson *et al.* (40 meV). Consequently the coupling of the $h_g(2)$ is not the strongest, which is consistent with many theoretical studies [4, 10–14].

In order to obtain the contribution to the VCCs from each atom, we calculated the AVCCs (2.5) and (2.6). The AVCCs are shown in Table 2.2. In general, the AVCCs of the $h_g(2)$ mode are smaller than those of the $h_g(7)$ and $h_g(8)$ modes. In the case of the stretching $h_g(7)$ and $h_g(8)$ modes, the AVCC is the largest at the C8 atom which is one of the 6:6 carbons.

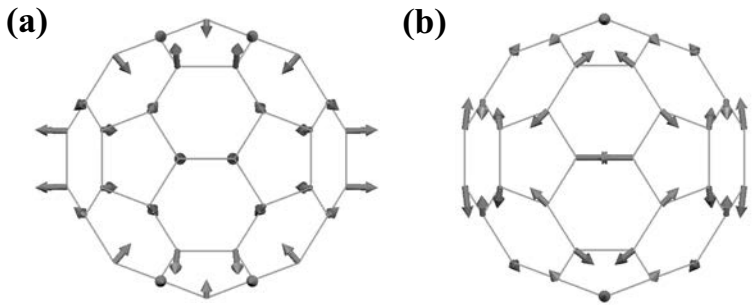

Figure 2.2: The θ elements of the (a) $h_g(2)$ and (b) $h_g(8)$ modes.

Table 2.1: Vibronic coupling constants to the a_g and h_g modes (10^{-4} a.u.) and the stabilization energies (meV). The VCCs obtained from PES are taken from Refs. [16] and [5]. Frequencies are taken from the data of a Raman scattering measurement of fullerite [29].

	Freq.	PES		B3LYP	
	(cm^{-1})	Iwahara [16]	Gunnarsson [5]	BS	S
$a_g(1)$	496	0.537	0.15	0.301	0.308
$a_g(2)$	1470	1.644	2.33	2.352	2.396
$h_g(1)$	273	0.215	0.36	0.185	0.128
$h_g(2)$	437	0.458	0.84	0.435	0.448
$h_g(3)$	710	0.837	0.77	0.740	0.655
$h_g(4)$	774	0.628	0.99	0.554	1.163
$h_g(5)$	1099	0.992	1.15	0.758	0.211
$h_g(6)$	1250	1.010	0.85	0.544	0.111
$h_g(7)$	1428	2.283	1.78	2.096	1.783
$h_g(8)$	1575	1.581	2.29	2.031	2.110
E_s		15.9	17.0	19.2	19.9
E_{JT}		57.7	88.2	49.4	51.0
$E_s + E_{\mathrm{JT}}$		73.6	105.2	68.6	70.9

2.4.2 Vibronic coupling density analysis

The strengths of the vibronic couplings can be explained in terms of the VCD (2.9). The difference between the AVCCs for the $h_g(2)$ and $h_g(8)$ modes is the largest at the C8 atom (Table 2.2), thus we focus on these two modes in the vibronic coupling density analysis.

The $t_{1u}z$ lowest unoccupied molecular orbital (LUMO) of C_{60} and the electron density differences of C_{60}^- are shown in Fig. 2.3. The positive (light gray) area of electron density differences $\Delta\rho$ originates from the LUMO density. One should note that $\Delta\rho$ obtained using the symmetry-broken wavefunction $|\Psi^{\mathrm{BS}}_{T_{1u}z}\rangle$ (Fig. 2.3 (b)) has not only positive but also polarized negative (dark gray) area. This negative area appears due to the Coulomb repulsion between the electron in the t_{1u} LUMO and other doubly-occupied electrons.

Table 2.2: Atomic vibronic coupling constants of the a_g and h_g modes (10^{-4} a.u.). The atomic label is shown in Fig. 2.1.

Atom	$a_g(1)$	$a_g(2)$	$h_g(1)$	$h_g(2)$	$h_g(3)$	$h_g(4)$	$h_g(5)$	$h_g(6)$	$h_g(7)$	$h_g(8)$
1	-0.004	0.014	-0.010	0.004	-0.003	-0.001	0.004	0.009	-0.028	0.005
2	0.003	-0.015	0.009	-0.007	-0.001	0.009	-0.026	0.006	0.012	-0.001
3	-0.011	-0.090	-0.048	-0.044	0.021	-0.063	-0.093	0.065	-0.028	-0.098
4	-0.005	0.002	-0.018	0.008	-0.005	-0.027	0.006	-0.036	-0.006	-0.006
5	-0.027	-0.061	0.042	0.030	-0.051	0.019	0.069	-0.038	-0.039	-0.072
6	0.008	-0.041	0.012	-0.021	-0.018	0.032	-0.079	-0.018	-0.059	0.010
7	0.002	-0.031	-0.007	-0.003	-0.013	-0.014	-0.013	-0.103	-0.057	-0.004
8	-0.031	-0.118	0.002	-0.019	-0.014	-0.057	0.074	0.103	-0.132	-0.193
9	0.019	-0.012	-0.017	-0.020	-0.035	0.006	0.003	0.000	-0.010	0.022
Total	-0.301	-2.352	-0.185	-0.435	-0.740	-0.554	-0.758	-0.544	-2.096	-2.031

Polarization in $\Delta\rho$ has been reported in other π system. [18]

In Fig. 2.4, the potential derivatives and the VCDs for the $h_g(2)$ and $h_g(8)$ modes are shown. The potential derivative of the bending $h_g(2)$ mode ($v_{h_g(2)}$) is localized on each atom (Fig. 2.4 (a1)). On the C1, C3, C4, C7, C8, and C9 atoms, the displacements of the $h_g(2)$ modes are perpendicular to the surface of the C_{60} cage, and the signs of $v_{h_g(2)}$ of the inside and outside of the cage are opposite. The VCD $\eta_{h_g(2)}$ is localized on each atom (Fig. 2.4 (a2)), and hence the integral of the VCD is canceled around the atom. In the case of the stretching $h_g(8)$ mode, on the other hand, $v_{h_g(8)}$ is delocalized on the C-C bonds of the 6:6 carbons (Fig. 2.4 (b1)). Since both $\Delta\rho$ and $v_{h_g(8)}$ are delocalized on the C-C bonds, $\eta_{h_g(8)}$ is also delocalized on the C-C bonds (Fig. 2.4 (b2)). Particularly, $\eta_{h_g(8)}$ has large density on the C8-C8' bonds, thus the AVCC of the C8 atom is the largest. The delocalized $\eta_{h_g(8)}$ on the C8-C8' bonds appears because of the polarized electron density difference. Therefore the polarization of $\Delta\rho$ is crucial to evaluate the vibronic coupling constants. In fact, the orbital VCC $\langle\psi_{0,\mathrm{L}z}|v_{h_g(8)\theta}|\psi_{0,\mathrm{L}z}\rangle$ is -0.775×10^{-4} a.u. where $\psi_{0,\mathrm{L}z}$ is the LUMO of the neutral C_{60}.

The electron density difference calculated using the symmetrized electronic state $|\Psi^{\mathrm{S}}_{T_{1u}z}\rangle$

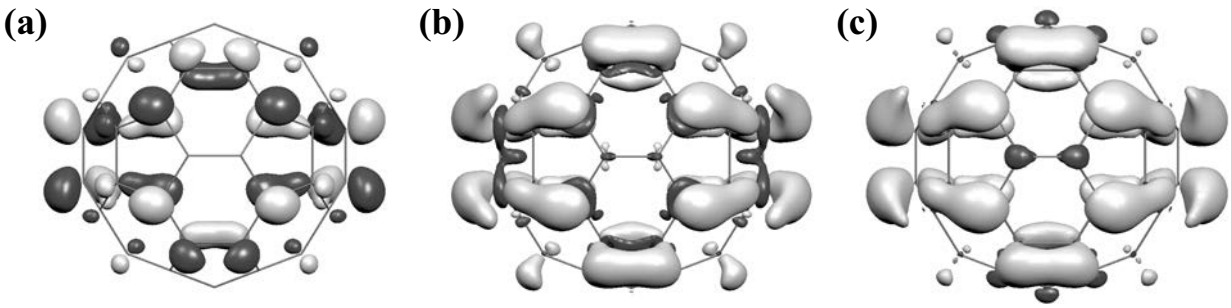

Figure 2.3: (a) LUMO, (b) Electron density difference $\Delta\rho$ of the symmetry-broken wavefunction and (c) electron density difference of the symmetrized wavefunction. The light gray and dark gray indicate positive and negative, respectively. The isosurface value is 0.035 a.u. for LUMO and 0.0008 a.u for electron density differences.

(Fig. 2.3 (c)) has small negative density. Moreover, $\Delta\rho$ has negative density on the C1, C2, and C9 atoms despite the small LUMO coefficients there. This result suggests that the Coulomb repulsion is not fully included in the electron density difference. The discrepancy between the experimental VCCs and theoretical ones computed with $|\Psi^{\mathrm{S}}_{T_{1u}z}\rangle$ should come from the the electron density difference.

Some authors have explained the order of the VCCs of C_{60}^{-} [4, 8, 9]. Varma *et al.* considered that the couplings to the stretching $h_g(7)$ and $h_g(8)$ modes are stronger than the coupling to the bending $h_g(2)$ mode because for a normalized displacement the distortion along the stretching mode gives larger change in energy than that along the bending mode does [4]. However, since they explained the VCC using the force constant, their discussion will not always give a correct result. Hands *et al.* assumed that the vibronic coupling is strong when the overlap between the t_{1u} LUMO and the displacements of the atoms is large [8, 9]. They concluded that the coupling to the $h_g(2)$ mode is large. Nonetheless, they did not take into account the derivative of the Coulomb potential between electron and nuclei $v(\mathbf{r})$, and that leads to opposite result to ours.

2.4.3 Electron-electron interactions in the electron density difference

In order to evaluate the contribution from each Kohn–Sham orbital to $\Delta\rho$, we decomposed $\Delta\rho$ into orbital densities (2.16). Fig. 2.5 shows the contribution of each Kohn–Sham

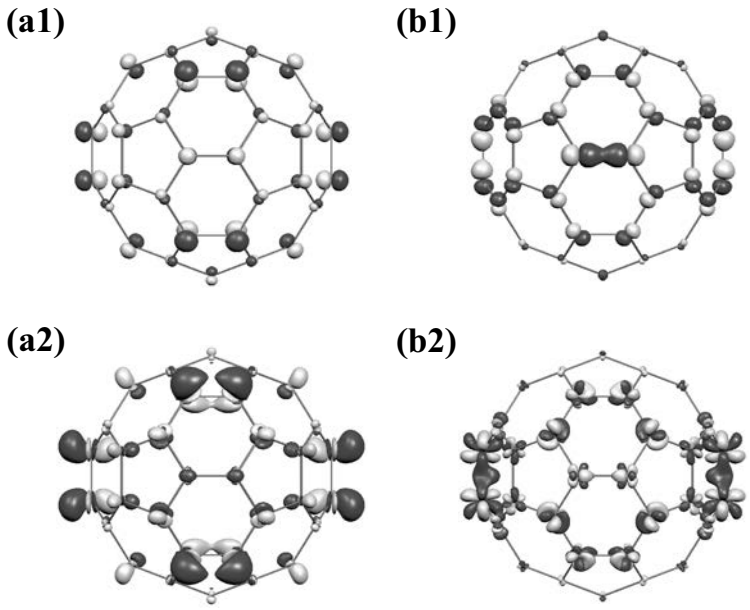

Figure 2.4: Potential derivatives for the (a1) $h_g(2)$ and (b1) $h_g(8)$ modes and vibronic coupling densities for the (a2) $h_g(2)$ and (b2) $h_g(8)$ modes. The light gray and dark gray indicate positive and negative, respectively. The isosurface value is 0.01 a.u. for the potential derivatives and 10^{-5} a.u. for the VCDs.

orbital to $\Delta\rho$ ($\sum_\lambda \sum_{\sigma=\uparrow,\downarrow} A(\Lambda(\nu)\lambda\sigma)$). Since one of the triply degenerate t_{1u} orbitals is occupied by an electron and the positive density of $\Delta\rho$ mainly originates from the $t_{1u}(7)$ orbital, the contribution of the LUMO ($t_{1u}(7)$) is the largest. However, as we have discussed in 2.4.2, the contributions to $\Delta\rho$ from both the occupied orbitals other than the LUMO are crucial too. The coefficients for the doubly occupied orbitals are negative because of the Coulomb repulsions between the doubly occupied electrons and the electron in the LUMO. Since these orbitals have finite orbital coefficients of s atomic orbitals and in-plane p atomic orbitals, $\Delta\rho$ has negative polarized density. Among the orbitals other than LUMO, $h_g(10)$ and $t_{1g}(3)$ orbitals (Fig. 2.6) have the largest negative and positive coefficients, respectively. The densities of these orbitals can mix with each other because these orbitals have common representations in their direct products. Since the density of the $h_g(10)$ orbital overlaps the LUMO density, the Coulomb repulsion between the electrons occupied in the LUMO and $h_g(10)$ orbitals is large. The Coulomb interactions give rise to an additional negative contribution in the $\Delta\rho$. Due to the decrease of the $h_g(10)$ density, the density around C1, C2, and C8 atoms where there is small SOMO density also decreases. The negative density around C1, C2, and C8 is canceled by the

$t_{1g}(3)$ density. As a result, $\Delta\rho$ is small around the C1, C2, and C8 atoms where the density of the $t_{1u}(7)$ SOMO is small, whereas there are both positive and negative areas around the atoms where the SOMO density is large.

It is desired that the wavefunction of C_{60}^{-} has the correct symmetry. Moreover, for the calculation of the VCCs, we must take into account the polarization of $\Delta\rho$. To fulfill both of them, a state-averaged post Hartree–Fock method could be one of the solutions. In the post Hartree–Fock calculation, we have to include not only frontier orbitals but also other orbitals which contribute to $\Delta\rho$.

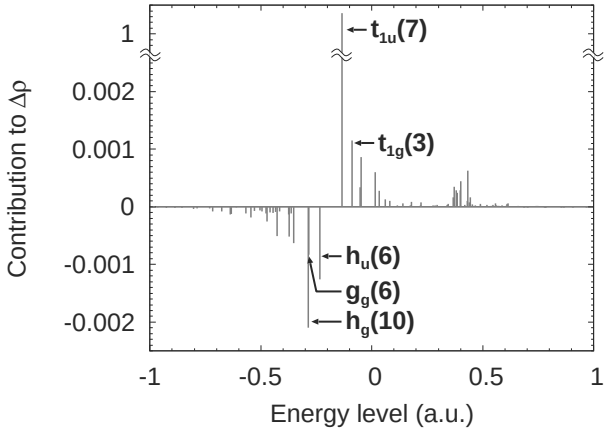

Figure 2.5: Contribution of each Kohn–Sham orbital to $\Delta\rho$. $t_{1u}(7)$ orbital is the LUMO.

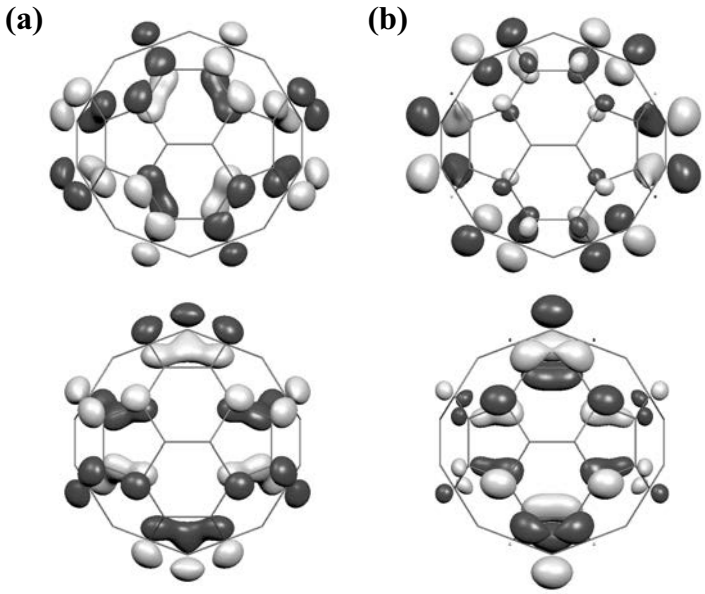

Figure 2.6: (a) $h_g(10)$ orbitals and (b) $t_{1g}(3)$ orbitals.

2.5 Conclusion

In this chapter, we analyzed the order of the vibronic coupling constants (VCCs) using the concept of the vibronic coupling density (VCD). The coupling to the bending $h_g(2)$ mode is small because the displacement of the vibrational mode is perpendicular to the surface of the C_{60} cage and the VCD is localized on atom. On the other hand, the coupling to the stretching $h_g(8)$ mode is large due to the delocalization of the VCD on the C-C bond. The polarization of the electron density difference is crucial for the couplings to the stretching modes. From the analysis of $\Delta\rho$, we found that the contribution from not only the frontier orbitals but also other orbitals are large. The VCD analysis clearly demonstrates the weakness of the vibronic coupling to the $h_g(2)$ mode. This may shed light on the mechanism of the electronic properties in alkali doped fullerides, A_4C_{60}, band insulator vs Mott-Hubbard insulator [30–32]. In addition to the solid state properties in fullerides, the VCD analysis can also be useful in the studies on C_{60} derivatives for organic photovoltaic cells.

Bibliography

[1] I. B. Bersuker, and V. Z. Polinger, *Vibronic Interactions in Molecules and Crystals* (Springer–VerlagBerlin and Heidelberg, 1989).

[2] I. B. Bersuker, *The Jahn–Teller Effect* (Cambridge University PressCambridge, 2006).

[3] C. C. Chancey, and M. C. M. O'Brien, *The Jahn–Teller Effect in C_{60} and other Icosahedral Complexes* (Princeton University PressPrinceton, 1997).

[4] C. M. Varma, J. Zaanen, and K. Raghavachari, Science **254**, 989 (1991).

[5] O. Gunnarsson, H. Handschuh, P. S. Bechthold, B. Kessler, G. Ganteför, and W. Eberhardt, Phys. Rev. Lett. **74**, 1875 (1995).

[6] N. Breda, R. A. Broglia, G. Colò, H. E. Roman, F. Alasia, G. Onida, V. Ponomarev, and E. Vigezzi, Chem. Phys. Lett. **286**, 350 (1998).

[7] I. D. Hands, J. L. Dunn, and C. A. Bates, Phys. Rev. B **63**, 245414 (2001).

[8] I. D. Hands, J. D. Dunn, and C. A. Bates, in *Advances in Quantum Chemistry*, edited by J. R. Sabin, and E. Brändas (Elsevier Academic PressSan Diego, 2003), Vol. 44, p. 335.

[9] I. D. Hands, J. L. Dunn, C. A. Bates, M. J. Hope, S. R. Meech, and D. L. Andrews, Phys. Rev. B **77**, 115445 (2008).

[10] N. Manini, A. D. Carso, M. Fabrizio, and E. Tosatti, Philos. Mag. B **81**, 793 (2001).

[11] M. Saito, Phys. Rev. B **65**, 220508(R) (2002).

[12] T. Frederiksen, K. J. Franke, A. Arnau, G. Schulze, J. I. Pascual, and N. Lorente, Phys. Rev. B **78**, 233401 (2008).

[13] J. Laflamme Janssen, M. Côté, S. G. Louie, and M. L. Cohen, Phys. Rev. B **81**, 073106 (2010).

[14] C. Faber, J. Laflamme Janssen, M. Côté, E. Runge, and X. Blase, Phys. Rev. B **84**, 155104 (2011).

[15] O. Gunnarsson, *Alkali-Doped Fullerides: Narrow-Band Solids with Unusual Properties* (World ScientificSingapore, 2004).

[16] N. Iwahara, T. Sato, K. Tanaka, and L. F. Chibotaru, Phys. Rev. B **82**, 245409 (2010).

[17] X. B. Wang, H. K. Woo, and L. S. Wang, J. Chem. Phys. **123**, 051106 (2005).

[18] T. Sato, K. Tokunaga, and K. Tanaka, J. Phys. Chem. A **112**, 758 (2008).

[19] T. Sato, K. Tokunaga, N. Iwahara, K. Shizu, and K. Tanaka, in *The Jahn–Teller Effect: Fundamentals and Implications for Physics and Chemistry*, edited by H. Köppel, D. R. Yarkony, and H. Barentzen (Springer–VerlagBerlin and Heidelberg, 2009), p. 99.

[20] K. Shizu, T. Sato, K. Tanaka, and H. Kaji, Appl. Phys. Lett. **97**, 142111 (2010).

[21] K. Shizu, T. Sato, A. Ito, K. Tanaka, and H. Kaji, J. Mater. Chem. **21**, 6375 (2011).

[22] T. Sato, K. Shizu, T. Kuga, K. Tanaka, and H. Kaji, Chem. Phys. Lett. **458**, 152 (2008).

[23] T. Sato, K. Shizu, K. Uegaito, N. Iwahara, K. Tanaka, and H. Kaji, Chem. Phys. Lett. **507**, 151 (2011).

[24] L. L. Boyle, and Y. M. Parker, Mol. Phys. **39**, 95 (1980).

[25] The definition of the VCCs for the h_g modes are slightly different from those in Ref. [3]. Eq. (2.2) is written as a product of the Clebsch–Gordan coefficient and reduced matrix element. The reduced matrix element is used as a vibronic coupling constant.

[26] M. Lannoo, G. A. Baraff, M. Schlüter, and D. Tomanek, Phys. Rev. B **44**, 12106 (1991).

[27] A. D. Becke, J. Chem. Phys. **98**, 5648 (1993).

[28] M. J. Frisch, G. W. Trucks, H. B. Schlegel, G. E. Scuseria, M. A. Robb, J. R. Cheeseman, G. Scalmani, V. Barone, B. Mennucci, G. A. Petersson, H. Nakatsuji, M. Caricato, X. Li, H. P. Hratchian, A. F. Izmaylov, J. Bloino, G. Zheng, J. L. Sonnenberg, M. Hada, M. Ehara, K. Toyota, R. Fukuda, J. Hasegawa, M. Ishida, T. Nakajima, Y. Honda, O. Kitao, H. Nakai, T. Vreven, J. J. A. Montgomery, J. E. Peralta, F. Ogliaro, M. Bearpark, J. J. Heyd, E. Brothers, K. N. Kudin, V. N. Staroverov, T. Keith, R. Kobayashi, J. Normand, K. Raghavachari, A. Rendell, J. C. Burant, S. S. Iyengar, J. Tomasi, M. Cossi, N. Rega, J. M. Millam, M. Klene, J. E. Knox, J. B. Cross, V. Bakken, C. Adamo, J. Jaramillo, R. Gomperts, R. E. Stratmann, O. Yazyev, A. J. Austin, R. Cammi, C. Pomelli, J. W. Ochterski, R. L. Martin, K. Morokuma, V. G. Zakrzewski, G. A. Voth, P. Salvador, J. J. Dannenberg, S. Dapprich, A. D. Daniels, O. Farkas, J. B. Foresman, J. V. Ortiz, J. Cioslowski, and D. J. Fox, *Gaussian 09, Revision B.01*, Wallingford CT, 2010.

[29] D. S. Bethune, G. Meijer, W. C. Tang, H. J. Rosen, W. G. Golden, H. Seki, C. A. Brown, and M. S. de Vries, Chem. Phys. Lett. **179**, 181 (1991).

[30] M. Fabrizio, and E. Tossati, Phys. Rev. B **55**, 13465 (1997).

[31] L. F. Chibotaru, A. Ceulemans, and S. P. Cojocaru, Phys. Rev. B **59**, R12728 (1999).

[32] M. Capone, M. Fabrizio, P. Giannozzi, and E. Tosatti, Phys. Rev. B **62**, 7619 (2000).

Chapter 3

C_{60} Bearing Ethylene Moieties

3.1 Introduction

In order to functionalize fullerenes, [4+2] cycloadditions to C_{60} (Figure 3.1) have been extensively studied in synthetic and material chemistry [1–3]. For example, mono adduct [4], bis adduct [5], and hexakis adduct with the T_h symmetry [6] have been isolated and characterized. The reactive site of these reactions is usually carbons of the C=C double bonds between two adjacent hexagon rings (6:6 carbons). Since the LUMOs of C_{60} are low-lying, C_{60} acts as a good dienophile.

Though these experimental findings indicate that C_{60} bears ethylene moieties in its cage, it is well known that the frontier orbital theory encounters difficulty to predict the reactivity. The t_{1u} LUMOs of C_{60} are three-fold degenerate and strongly delocalized as shown in Figure 3.2. Since the averaged frontier electron density shown in Figure 3.3 is totally symmetric, one cannot predict the reactive site. In order to overcome the difficulty, Fukui *et al.* have proposed the interaction frontier orbitals (IFO) [7]. The IFO approach is based on an orbital localization technique. Chikama *et al.* have applied the IFO theory for the Diels-Alder reaction of C_{60} [8].

In addition to an electronic structure, molecular vibrations are also essential for chemical reactions because they cause molecular distortions in the reaction processes. Therefore, in chemical reactions, it is desired to discuss a vibronic (electron-vibration) coupling [9,10] which is a driving force of the distortions. In this chapter, we propose that vibronic coupling density (VCD) [11, 12] for a reaction mode can be regarded as a reactivity index. We demonstrate this for the [4+2] cycloaddition to C_{60}.

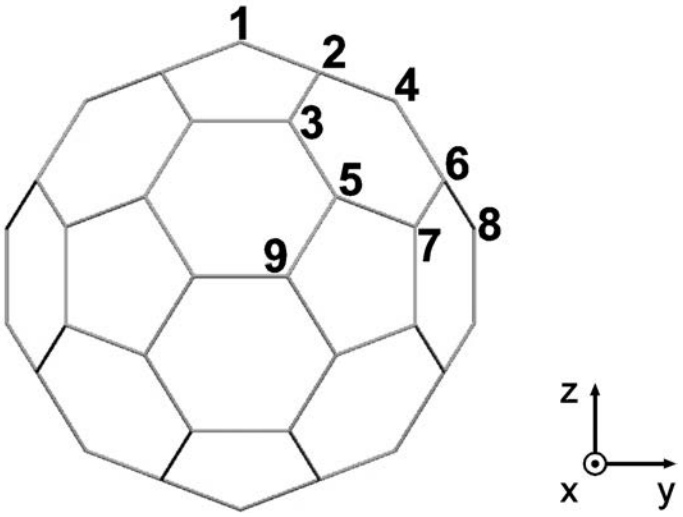

Figure 3.1: Numbering scheme of C_{60}. C8 is one of the 6:6 carbons of the C=C bonds between two adjacent hexagons.

3.2 Theory

The vibronic coupling density is defined as a product of the electron density difference $\Delta\rho$ between a neutral and an ionized (charge-transfer) state and the potential derivative v_α with respect to a mass-weighted normal coordinate Q_α:

$$\eta_\alpha(\mathbf{r}) := \Delta\rho(\mathbf{r}) \times v_\alpha(\mathbf{r}). \tag{3.1}$$

The potential derivative $v_\alpha(\mathbf{r})$ is defined as a derivative of a potential $u(\mathbf{r})$ acting on one electron from all the nuclei:

$$v_\alpha(\mathbf{r}) := \left(\frac{\partial u(\mathbf{r})}{\partial Q_\alpha}\right)_0. \tag{3.2}$$

The vibronic coupling constant (VCC) V_α is exactly equal to the integral of η_α [11, 12]:

$$V_\alpha = \int \eta_\alpha(\mathbf{r})\, d^3\mathbf{r}. \tag{3.3}$$

Based on Eq. 3.3, we can discuss a vibronic coupling in terms of the electronic structure $\Delta\rho$ and the vibrational structure v_α. We have applied the VCD analysis for carrier-transporting molecules, and succeeded in elucidating that a hole-transporting molecule, TPD, has small VCCs from view of the VCDs [11]. Furthermore, we have shown that VCCs can be controlled based on the VCD analysis to design highly-efficient carrier-transporting molecules [13, 14].

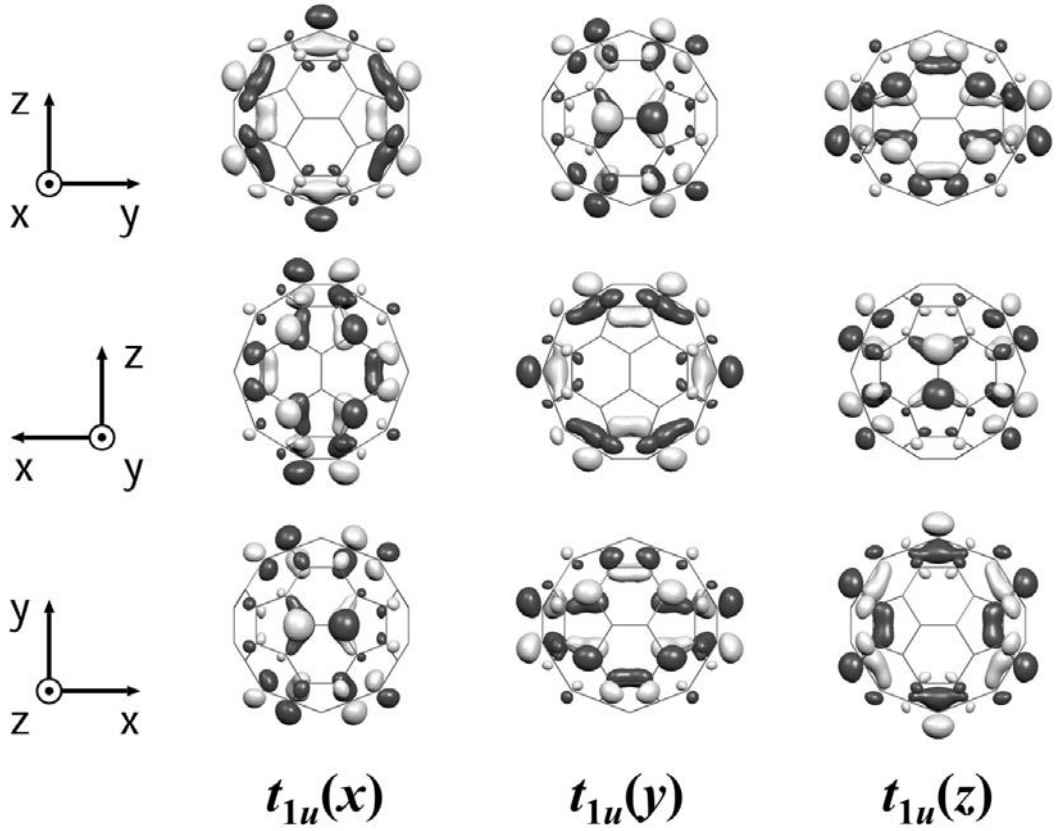

Figure 3.2: Symmetrized t_{1u} LUMOs of C_{60}.

Here we show the theoretical background of the VCD analysis for chemical reactions. Parr and Yang have derived the classical frontier-orbital theory from the conceptual density-functional theory [15]. Ground-state electronic energy of a species S is a functional of the number of electrons N and u: $E = E[N; u]$. Chemical potential μ is defined by $(\partial E/\partial N)_u$. The total differential of $E = E[N; u]$ is

$$dE = \mu\, dN + \int \rho(\mathbf{r})\, du(\mathbf{r})\, d^3\mathbf{r}. \tag{3.4}$$

The total differential of $\mu = \mu[N; u]$ is written as

$$d\mu = 2\eta dN + \int f(\mathbf{r})\, du(\mathbf{r})\, d^3\mathbf{r}, \tag{3.5}$$

where η is the hardness, and f is the Fukui function:

$$f(\mathbf{r}) := \left(\frac{\delta\mu}{\delta u(\mathbf{r})}\right)_N = \left(\frac{\partial\rho}{\partial N}\right)_u. \tag{3.6}$$

The last equality comes from the Maxwell relation of Eq. 3.4. The problem of chemical reactivity is what direction is preferred when a reagent R approaches S. Parr and Yang

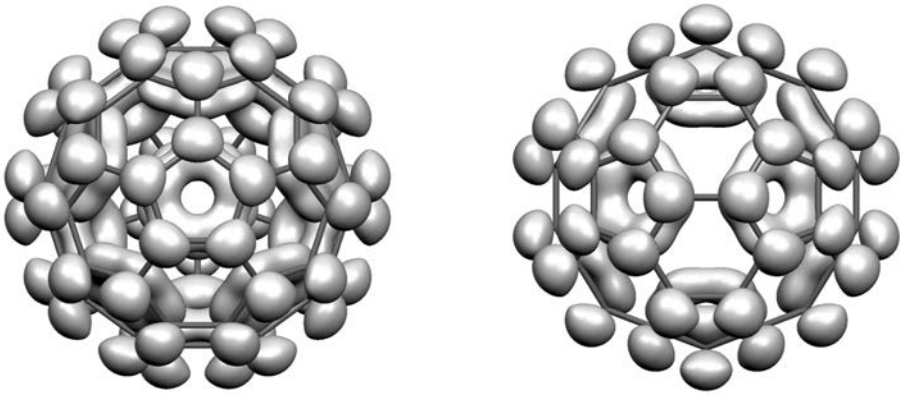

Figure 3.3: Averaged density of the LUMOs.

assumed that *the preferred direction is the one for which the initial* $|d\mu|$ *for the species* S *is a maximum* [15]. Based on the principle, they have derived the classical frontier-orbital theory.

Let us start from this principle. We assume that (1) the Fukui function is approximated by $\Delta\rho$ and (2) du is expressed in terms of normal modes:

$$du = \sum_{\alpha} \left(\frac{\partial u}{\partial Q_\alpha} \right)_0 dQ_\alpha = \sum_{\alpha} v_\alpha dQ_\alpha, \tag{3.7}$$

where $\alpha = a_g(1), a_g(2), h_g(1), \cdots, h_g(8)$. Furthermore, the effective mode s is assumed to coincide with the direction of the reaction path:

$$ds := \sum_{\alpha} \lambda_\alpha dQ_\alpha, \text{where} \quad \lambda_\alpha := \frac{V_\alpha}{\sqrt{\sum_\alpha V_\alpha^2}}. \tag{3.8}$$

Finally we obtain

$$d\mu = 2\eta dN + \int \Delta\rho(\mathbf{r}) v_s(\mathbf{r})\, ds\, d^3\mathbf{r} = 2\eta dN + \int \eta_s(\mathbf{r})\, ds\, d^3\mathbf{r}, \tag{3.9}$$

where v_s and η_s are the potential derivative and the vibronic coupling density for the reaction mode s, respectively. From the principle by Parr and Yang, *the preferred direction is the one for which the initial* $|\eta_s|$ *for the species* S *is a maximum.*

3.3 Method

We have published vibronic coupling constants of C_{60}^- which reproduce the experimental photoelectron spectrum well [16]. The VCD for the reaction mode was calculated employing our previous results by using B3LYP/6-311G(d) [16]. A VCC can be decomposed

into atomic contributions, atomic vibronic coupling constants (AVCC) [17]. We also calculated the AVCC for the reaction mode. We show the results for the vibronic coupling between the electronic $T_{1u}(z)$ state and the reaction mode consisting of all the a_g and $h_g(2z^2 - x^2 - y^2)$ modes.

3.4 Results and discussion

Table 3.1: Atomic vibronic coupling constants for the reaction mode in 10^{-4} a.u. The labeling is defined in Figure 3.1.

Label	Num. of equiv. atoms	AVCC
C1	4	-0.003
C2	8	-0.006
C3	8	-0.138
C4	8	-0.014
C5	8	-0.088
C6	8	-0.067
C7	8	-0.071
C8	4	-0.223
C9	4	-0.008
Total		-4.008

The calculated AVCCs are tabulated in Table 3.1. The 6:6 carbon C8 has the maximum of the AVCCs. Figure 3.4 shows the electron density difference $\Delta\rho$, the reaction mode s, and the potential derivative v_s. Though $\Delta\rho$ is delocalized like a belt, the reaction mode has a large displacement on C8 atoms. Accordingly $|v_s|$ on C8 has a large value. Figure 3.5(a) shows the vibronic coupling density η_s. $|\eta_s|$ has the maximum on the 6:6 carbon, C8. The VCD of ethylene anion is also shown in Figure 3.5(b) for comparison. It is clear that the distribution of the VCD on the C8 atoms of C_{60} is almost the same as that of the ethylene. From view of the vibronic coupling density, C_{60} bears ethylene moieties in its cage.

Since there are other two reaction modes corresponding to the $T_{1u}(x)$ and $T_{1u}(y)$ electronic states, the C_{60} cage contains six dienophiles, which is consistent with the ex-

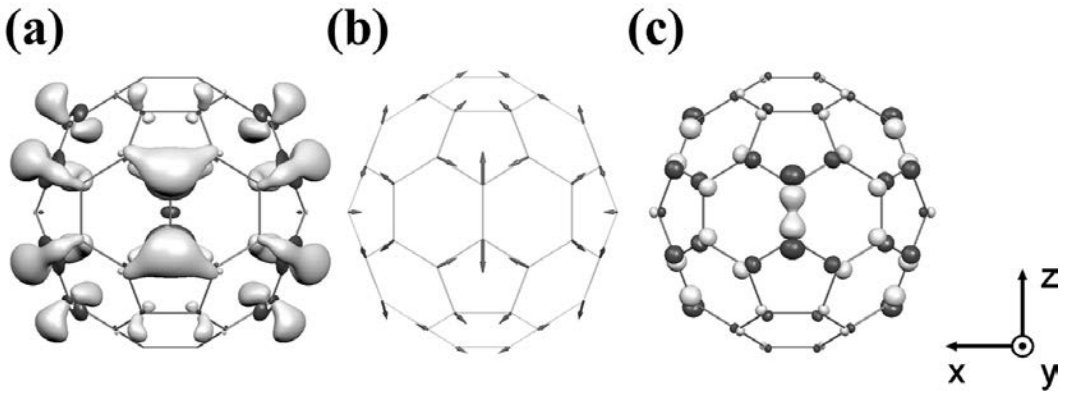

Figure 3.4: (a) Electron density difference $\Delta\rho$, (b) reaction mode s, and (c) potential derivative v_s for the reaction mode in C_{60}^{-}.

perimental observation of the hexakis adduct [6]. In the previous theoretical studies, both the t_{1u} LUMOs and the t_{1g} next LUMOs of C_{60} compose the frontier bonding orbitals of the hexakis adduct [18, 19]. Our theory is consistent with these results because $\Delta\rho$ includes contributions from the LUMOs of C_{60} as well as the other orbitals due to the effects of orbital mixing and relaxation. Since we consider not the t_{1u} LUMOs but the T_{1u} electronic states, all the possible contributions from the orbitals other than the frontier orbitals including the t_{1g} next LUMOs are naturally incorporated to the VCD for the reaction mode. In other words, the present theory has an advantage that the concept of the VCD is free from the orbital approximation.

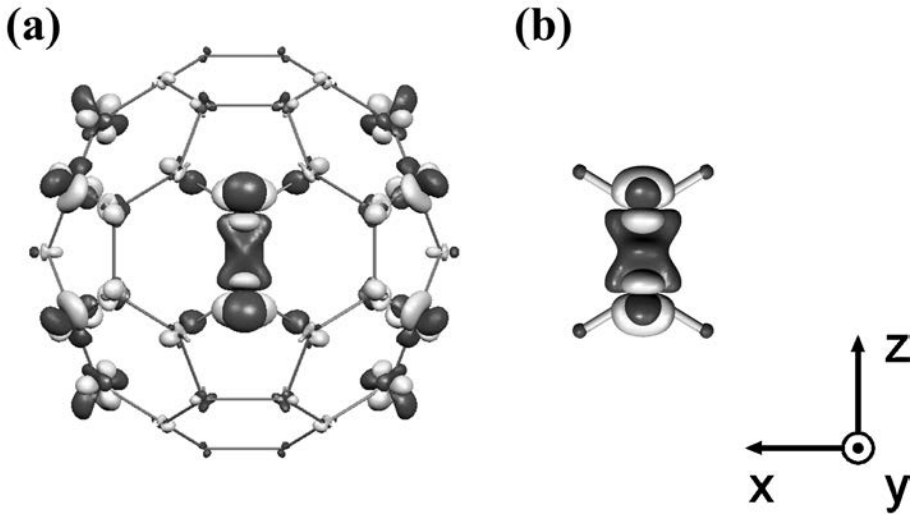

Figure 3.5: Vibronic coupling density analysis for the reaction mode in (a) C_{60}^{-} and (b) ethylene monoanion.

3.5 Conclusion

The vibronic coupling density for the reaction mode can be regarded as a reaction index which can be employed even for large systems such as a fullerene. One of the advantages is that the results of post Hartree-Fock calculations can be employed since the VCD is not based on the orbital approximation. In addition, no orbital localization technique is required. From view of the vibronic coupling density, C_{60} bears ethylene moieties which behave as a dienophile. In other words, the C_{60} cage contains the six isolated double bonds as a functional group. The VCD analysis may extract a picture of a functional group from the results of quantum-chemistry calculations without any localization technique as in the ethylene moieties of C_{60}. We will apply the present theory for similar reactions of higher fullerenes including metallofullerenes [20] and fullerenes encapsulating a molecule such as H_2O [21] in the near future.

Bibliography

[1] A. Hirsch, Synthesis 895 (1995).

[2] W. Śliwa, Full. Sci. Techn. **5**, 1133 (1997).

[3] M. A. Yurovskaya, and I. V. Trushkov, Russian Chem. Bull. Int. Ed. **51**, 367 (2002).

[4] Y. Rubin, S. Khan, D. I. Freedberg, and C. Yeretzian, J. Am. Chem. Soc. **115**, 344 (1993).

[5] M. Tsuda, T. Ishida, T. Nogami, S. Kurono, and M. Ohashi, J. Chem. Soc. Chem. Comm. 1296 (1993).

[6] B. Kräutler, and J. Maynollo, Angew. Chem. Int. Ed. Engl. **34**, 87 (1995).

[7] K. Fukui, N. Koga, and H. Fujimoto, J. Am. Chem. Soc. **103**, 196 (1981).

[8] A. Chikama, H. Fueno, and H. Fujimoto, J. Phys. Chem. **99**, 8541 (1995).

[9] G. Fischer, *Vibronic Coupling: The interaction between the Electronic and Nuclear Motions* (Academic PressLondon, 1984).

[10] I. B. Bersuker, *The Jahn–Teller Effect* (Cambridge University PressCambridge, 2006).

[11] T. Sato, K. Tokunaga, and K. Tanaka, J. Phys. Chem. A **112**, 758 (2008).

[12] T. Sato, K. Tokunaga, N. Iwahara, K. Shizu, and K. Tanaka, in *The Jahn–Teller Effect: Fundamentals and Implications for Physics and Chemistry*, edited by H. Köppel, D. R. Yarkony, and H. Barentzen (Springer–VerlagBerlin and Heidelberg, 2009), p. 99.

[13] K. Shizu, T. Sato, K. Tanaka, and H. Kaji, Appl. Phys. Lett. **97**, 142111 (2010).

[14] K. Shizu, T. Sato, A. Ito, K. Tanaka, and H. Kaji, J. Mater. Chem. **21**, 6375 (2011).

[15] R. G. Parr, and W. Yang, J. Am. Chem. Soc. **106**, 4049 (1984).

[16] N. Iwahara, T. Sato, K. Tanaka, and L. F. Chibotaru, Phys. Rev. B **82**, 245409 (2010).

[17] T. Sato, K. Shizu, T. Kuga, K. Tanaka, and H. Kaji, Chem. Phys. Lett. **458**, 152 (2008).

[18] P. W. Fowler, and A. Ceulemans, J. Phys. Chem. **99**, 508 (1995).

[19] C. Bo, M. Costas, and J. M. Poblet, J. Phys. Chem. **99**, 5914 (1995).

[20] X. Lu, T. Akasaka, and S. Nagase, Chem. Commun. **47**, 5942 (2011).

[21] K. Kurotobi, and Y. Murata, Science **333**, 613 (2011).

Chapter 4

Vibronic Couplings in C_{60} Derivatives for Organic Photovoltaics

4.1 Introduction

Fullerene (C_{60}) derivatives have been employed as acceptors in organic photovoltaics (OPV) [1]. C_{60} derivatives are known to be good electron-transporting materials since the vibronic couplings (VC) which give rise to inelastic scattering of an electron are small. The VCs have been discussed using a reorganization energy which can be decomposed into vibronic coupling constants (VCC) and vibrational frequencies. So far, the reorganization energy of a C_{60} derivative has been estimated in solution [2, 3].

Recently we have estimated the VCCs of C_{60}^{-} from the photoelectron spectrum in gas phase [4] using the exact diagonalization of a dynamic Jahn-Teller Hamiltonian [5]. Furthermore the estimated VCCs agree well with the density functional calculation [5]. Therefore, the method of calculation is expected to be applied for accurate estimations of the VCCs in C_{60} derivatives.

The VCCs can be analyzed in terms of vibronic coupling density (VCD) [6]. The VCD provides a local picture of the VC from the electronic and vibrational structures. Moreover, using the VCD analysis, we have succeeded in designing novel hole- and electron-transporting molecules with small VCCs [7, 8].

In this study, we calculate the VCCs or reorganization energies in C_{60} derivative anions

(see Fig. 4.1) and analyze the VCs in terms of VCD, and compare the VCs with those in C_{60} anion. (see Figs. 4.1). [6,6]-phenyl-C-61-butyric acid methyl ether (PCBM) is employed as an acceptor in organic thin film solar cells [1]. Fullerene pyrrolidines (**2**, **3**) are used as acceptors in donor acceptor dyads [3]. The calculated results are analyzed in terms of vibronic coupling density analysis.

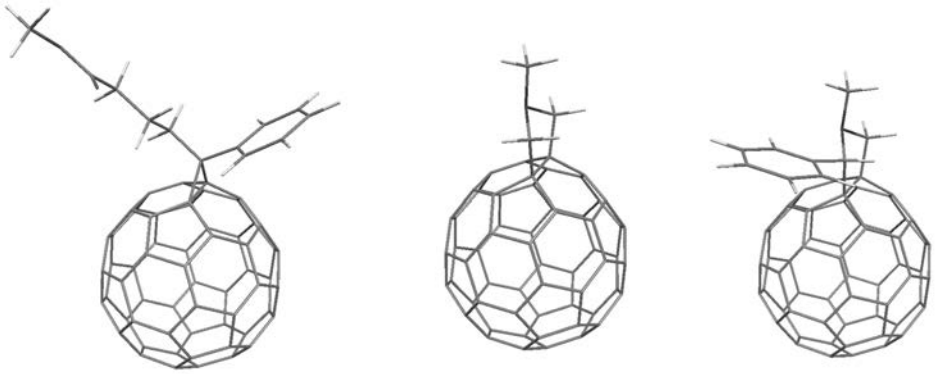

1 (PCBM, C_1) **2** (C_s) **3** (C_1)

Figure 4.1: Calculated C_{60} derivatives.

4.2 Theory

Vibronic coupling constant for a vibrational mode α is defined by

$$V_\alpha = \left\langle \Psi(\mathbf{R_0}, \mathbf{r}) \left| \left(\frac{\partial \hat{H}(\mathbf{Q}, \mathbf{r})}{\partial Q_\alpha} \right)_{\mathbf{R_0}} \right| \Psi(\mathbf{R_0}, \mathbf{r}) \right\rangle, \tag{4.1}$$

where Ψ denotes the electronic wavefunction for the anionic state at the equilibrium structure of the neutral state $\mathbf{R_0}$, $\mathbf{r} = (\mathbf{r}_1, \cdots, \mathbf{r}_i, \cdots, \mathbf{r}_N)$ a set of the electron coordinates, $\hat{H}$ molecular Hamiltonian, $\mathbf{Q} = (Q_1, \cdots, Q_\alpha, \cdots)$ a set of the normal coordinate Q_α. Vibronic Hamiltonian can be written as

$$\hat{H}_{\text{vibro}} = E_0 + \sum_{\alpha}^{3M-6} \left(-|V_\alpha| Q_\alpha + \frac{1}{2}\omega_\alpha^2 Q_\alpha^2 \right), \tag{4.2}$$

where E_0 is the ground-state electronic energy of the anion at $\mathbf{R}_0$. The direction of mode α is defined so as V_α is negative. The vibronic Hamiltonian can be rewritten as

$$\hat{H}_{\text{vibro}} = E_0 + \sum_{\alpha}^{3M-6} \left[\frac{1}{2}\omega_\alpha^2 \left(Q_\alpha - \frac{|V_\alpha|}{2\omega_\alpha^2} \right)^2 - \frac{V_\alpha^2}{2\omega_\alpha^2} \right]. \tag{4.3}$$

From Eq.(4.3), reorganization energy for mode α is obtained as

$$E_{R,\alpha} = \frac{V_\alpha^2}{2\omega_\alpha^2}. \tag{4.4}$$

Total reorganization energy is calculated from

$$E_R = \sum_\alpha E_{R,\alpha}. \tag{4.5}$$

VCD for a vibrational mode α is defined by

$$\eta_\alpha(\mathbf{r}_i) = \Delta\rho(\mathbf{r}_i) \times v_\alpha(\mathbf{r}_i), \tag{4.6}$$

where $\Delta\rho(\mathbf{r}_i) = \rho(\mathbf{r}_i) - \rho_0(\mathbf{r}_i)$ is the electron density difference between the anionic density ρ and the neutral density ρ_0. Potential derivative $v_\alpha(\mathbf{r}_i)$ is defined using the nuclear attraction potential acting on a single electron:

$$u(\mathbf{r}_i) = \sum_{A=1}^{M} -\frac{Z_A e^2}{4\pi\epsilon_0 |\mathbf{r}_i - \mathbf{R}_A|}, \tag{4.7}$$

where M is the number of the nuclei, and $\mathbf{R}_A$ and Z_A denote the position and the charge of nucleus A, respectively. The potential derivative is defined by

$$v_\alpha(\mathbf{r}_i) = \left(\frac{\partial u(\mathbf{r}_i)}{\partial Q_\alpha} \right)_{\mathbf{R}_0}, \tag{4.8}$$

The space integral of a vibronic coupling density η_α yields the VCC:

$$V_\alpha = \int \eta_\alpha(\mathbf{r}_i)\, d^3\mathbf{r}_i = \int \Delta\rho(\mathbf{r}_i) \times v_\alpha(\mathbf{r}_i)\, d^3\mathbf{r}_i. \tag{4.9}$$

The VCC can be analyzed in terms of the electronic structure $\Delta\rho$ and the vibrational structure v_α through the VCD η_α based on Eq. (4.9). Note that a VCD is sometimes canceled in a certain region since a VCD distributes with positive and negative values.

Effective mode with the VCC

$$V_{\text{eff}} = \sqrt{\sum_\alpha V_\alpha^2} \tag{4.10}$$

is defined by

$$\mathbf{u}_{\text{eff}} = \sum_{\alpha=1}^{3M-6} \left(\frac{|V_\alpha|}{V_{\text{eff}}} \right) \mathbf{u}_\alpha, \tag{4.11}$$

where $\mathbf{u}_\alpha$ is a vibrational vector of mode α. For the effective mode, the frequency and the reorganization energy are

$$\omega_{\text{eff}}^2 = \sum_\alpha \frac{V_\alpha^2}{V_{\text{eff}}^2} \omega_\alpha^2, \tag{4.12}$$

$$E_{\text{eff}} = \frac{V_{\text{eff}}^2}{2\omega_{\text{eff}}^2}. \tag{4.13}$$

respectively.

4.3 Method of calculation

We employed the B3LYP functional with the 6-311G(d,p) basis set. The reference structures were obtained by geometry optimizations of the neutral states. Vibrational analyses were applied for the optimized structures to be checked if the structure is a stationary minimum. Analytical force calculations were performed for the optimized structures of the neutral states. We employed the Gaussian09 packages for the optimizations, vibrational analysis, and force calculations [9]. The VCCs were evaluated using the results of the force calculations. The VCD analyses were performed using the electronic wavefunctions of the neutral and anionic states at their reference geometry as well as the vibrational modes. The VCC and VCD calculations were performed using our codes. In order to analyze the electronic structures, we performed the fragment molecular orbital analysis using the YAeHMOP program [10].

4.4 Results and discussion

4.4.1 Vibronic coupling constants

Figures 4.2 show the calculated vibronic coupling constants V_α of C_{60}^- [5] and the anions of its derivatives. The VCCs of the derivatives are quite similar to those of C_{60}^-. For C_{60}^-, the VCCs of the $a_g(2)$ (1492 cm^{-1}), $h_g(7)$ (1442 cm^{-1}), and $h_g(8)$ (1608 cm^{-1}) modes are strong. For the derivative anions, the vibrational mode originating from the $a_g(2)$ mode of C_{60} is the most intense among other modes, and the mode from the $h_g(8)$ mode of C_{60} is the second strongest.

Since the symmetry of C_{60} is I_h, and the LUMOs belong to the t_{1u} irreducible representation, the T_{1u} electronic state couples with a_g and h_g modes from the selection rule, $[T_{1u}^2] = a_g \oplus h_g$. In C_{60}, there are two a_g modes and eight sets of h_g modes. Therefore, the number of the vibronically active modes is 42 for C_{60}^-. The VCCs of the other modes are exactly zero. On the other hand, the symmetries of the derivatives are lower than that of C_{60}. The derivatives has larger number of active modes than C_{60} does. For example, PCBM has 258 active modes. However, note that the VCCs for the modes which originate from the active modes of C_{60}^-, a_g and h_g modes, are large.

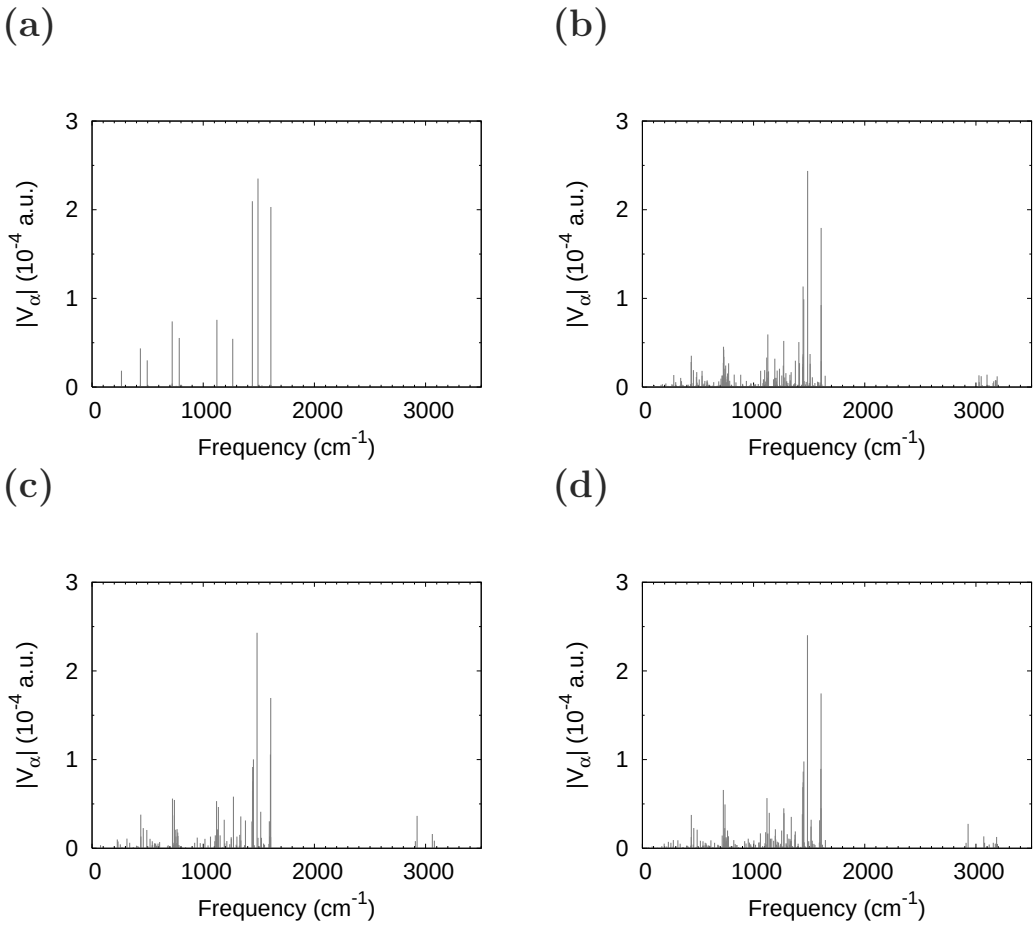

Figure 4.2: Vibronic coupling constants of (a) C_{60}^-, (b) PCBM$^-$, (c) C_{60} pyrrolidine$^-$ (C_s), and (d) C_{60} pyrrolidine derivative$^-$ (C_1) in 10^{-4} a.u.

4.4.2 Reorganization energies

Reorganization energies $E_{R,\alpha}$ are shown in Fig. 4.3, and total reorganization energies E_R are tabulated in Table 4.1. The reorganization energies of the derivatives are almost the same as that of C_{60}^-. The reorganization energy of PCBM is larger than C_{60} by 7 meV. Since the symmetry of PCBM is C_1, all the vibrational modes are active and contribute to the reorganization energy. Present reorganization energies are slightly larger than experimental value of *ca.* 50 meV [2].

The VCCs and total reorganization energies for the effective modes of the derivatives are the same as C_{60} as tabulated in Table 4.1. Moreover, the Mulliken charges on the substituent group are small. These result indicates that the vibronic couplings in the derivatives originate from the coupling in C_{60}.

Table 4.1: Total reorganization energies E_R (meV). Frequencies ω_{eff} (cm^{-1}, vibronic couplings V_{eff} (10^{-4} a.u.), and stabilization energies E_{eff} (meV) of the effective modes. Sums of Mulliken charges on the substituent groups.

	E_R	ω_{eff}	V_{eff}	E_{eff}	Charge
C_{60}^-	67.2	1450	4.01	50.1	
$\mathbf{1}^-$	74.0	1452	4.03	50.4	-0.098
$\mathbf{2}^-$	69.2	1466	4.00	48.8	-0.095
$\mathbf{3}^-$	69.1	1460	4.00	49.1	-0.109

4.4.3 Vibronic coupling density

Figure 4.4 (a) shows the LUMO and the electron density difference of PCBM. The LUMO is strongly localized on the C_{60} fragment.On the other hand, the electron density difference appears not only on C_{60} but also on the substituent (Fig. 4.4 (b)). In addition, σ-type polarization of $\Delta\rho$ is found on the C_{60} cage. These properties of $\Delta\rho$ are due to the Coulomb interactions between the doubly occupied electrons and an additional electron in the anion. In other words, the many-body effect strongly affects $\Delta\rho$, and therefore, VCCs [11].

The LUMOs of the derivatives originate from a t_{1u} LUMO of C_{60}, and the $\Delta\rho$'s are localized on the C_{60} fragments. The electronic states of the derivative anions strongly couple to vibrational modes corresponding to $a_g(2)$ and $h_g(8)$ modes of C_{60}. Therefore, the distributions of the VCDs in the derivative anions are similar to that of C_{60}^- (see chapter 2 in Part II). Furthermore, the effective modes of the derivative anions are the stretching mode of the 6:6 C=C double bond, which is the same as in C_{60}^- (see chapter 3 in Part II). Figure 4.5 shows the VCD analysis of the effective mode.

The VCCs or reorganization energies of C_{60}^- and derivatives are close to each other because the distribution of the LUMOs of the derivatives are similar to that of C_{60}. This conservation of LUMO is explained based on the FMO analysis. For FMO analysis, each C_{60} derivative is divided into C_{60} (Fragment A) and the substituted group (Fragment B). The FMO of PCBM is shown in Fig. 4.6. The HOMO of PCBM consists of h_g and t_{1u} frontier orbitals of C_{60} and the LUMO of Fragment B. One of the t_{1u} LUMOs contributes

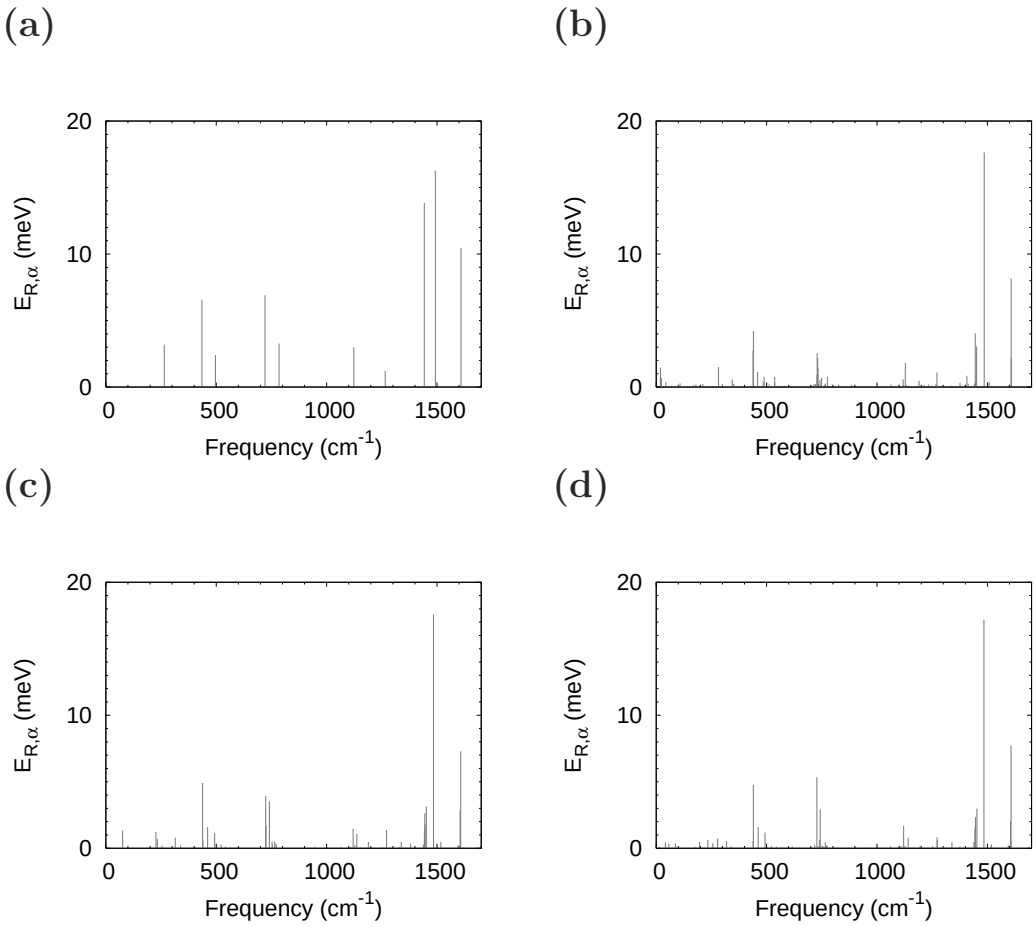

Figure 4.3: Reorganization energies $E_{R,\alpha}$ of (a) C_{60}^{-}, (b) PCBM^{-}, (c) C_{60} pyrrolidine^{-}, and (d) C_{60} pyrrolidine derivative^{-} in meV.

to the HOMO and the others do not. The latter are almost unchanged under addition of the substituent. Therefore, the LUMO of PCBM is almost the same as the LUMO of C_{60}. As long as the LUMO of a derivative is similar to the LUMO of C_{60}, the VCCs or reorganization of the derivative is almost the same as those of C_{60}.

4.5 Summary

VCCs and reorganization energy of C_{60} derivative anions including PCBM were evaluated. The results were analyzed in terms of the VCD.

All the molecules calculated exhibit almost the same VCCs in C_{60}^{-}. Since the LUMO of the derivatives originate from the t_{1u} LUMOs, $\Delta\rho$ is localized on the C_{60} fragment. The reorganization energy of PCBM is slightly larger than that of C_{60}. This is because the molecular symmetry of PCBM is low. In order to avoid increase of the reorganization

energy, (1) $\Delta\rho$ should localize on the C_{60} fragment, and (2) the molecular symmetry should be high. Therefore, a low symmetry derivative with a delocalized LUMO would exhibit large VCCs and not be suitable for a OPV material from view of vibronic couplings.

Bibliography

[1] G. Yu, J. Gao, J. C. Hummelen, F. Wudl, and A. J. Heeger, Science **270**, 1789 (1995).

[2] H. Imahori, N. V. Tkachenko, V. Vehmanen, K. Tamaki, H. Lemmetyinen, Y. Sakata, and S. Fukuzumi, J. Phys. Chem. A **105**, 1750 (2001).

[3] H. Imahori, Bull. Chem. Soc. Jpn. **80**, 621 (2007).

[4] X. B. Wang, H. K. Woo, and L. S. Wang, J. Chem. Phys. **123**, 051106 (2005).

[5] N. Iwahara, T. Sato, K. Tanaka, and L. F. Chibotaru, Phys. Rev. B **82**, 245409 (2010).

[6] T. Sato, K. Tokunaga, and K. Tanaka, J. Phys. Chem. A **112**, 758 (2008).

[7] K. Shizu, T. Sato, K. Tanaka, and H. Kaji, Appl. Phys. Lett. **97**, 142111 (2010).

[8] K. Shizu, T. Sato, A. Ito, K. Tanaka, and H. Kaji, J. Mater. Chem. **21**, 6375 (2011).

[9] M. J. Frisch, G. W. Trucks, H. B. Schlegel, G. E. Scuseria, M. A. Robb, J. R. Cheeseman, G. Scalmani, V. Barone, B. Mennucci, G. A. Petersson, H. Nakatsuji, M. Caricato, X. Li, H. P. Hratchian, A. F. Izmaylov, J. Bloino, G. Zheng, J. L. Sonnenberg, M. Hada, M. Ehara, K. Toyota, R. Fukuda, J. Hasegawa, M. Ishida, T. Nakajima, Y. Honda, O. Kitao, H. Nakai, T. Vreven, J. J. A. Montgomery, J. E. Peralta, F. Ogliaro, M. Bearpark, J. J. Heyd, E. Brothers, K. N. Kudin, V. N. Staroverov, T. Keith, R. Kobayashi, J. Normand, K. Raghavachari, A. Rendell, J. C. Burant, S. S. Iyengar, J. Tomasi, M. Cossi, N. Rega, J. M. Millam, M. Klene, J. E. Knox, J. B. Cross, V. Bakken, C. Adamo, J. Jaramillo, R. Gomperts, R. E. Stratmann, O. Yazyev, A. J. Austin, R. Cammi, C. Pomelli, J. W. Ochterski, R. L. Martin, K. Morokuma, V. G. Zakrzewski, G. A. Voth, P. Salvador, J. J. Dannenberg, S. Dapprich, A. D. Daniels, O. Farkas, J. B. Foresman, J. V. Ortiz, J. Cioslowski, and D. J. Fox, *Gaussian 09, Revision B.01*, Wallingford CT, 2010.

[10] G.A.Landrum and W.V.Glassey, YAeHMOP (ver. 3.0). http://sourceforge.net/projects/yaehmop/.

[11] T. Sato, K. Shizu, K. Uegaito, N. Iwahara, K. Tanaka, and H. Kaji, Chem. Phys. Lett. **507**, 151 (2011).

(a) LUMO

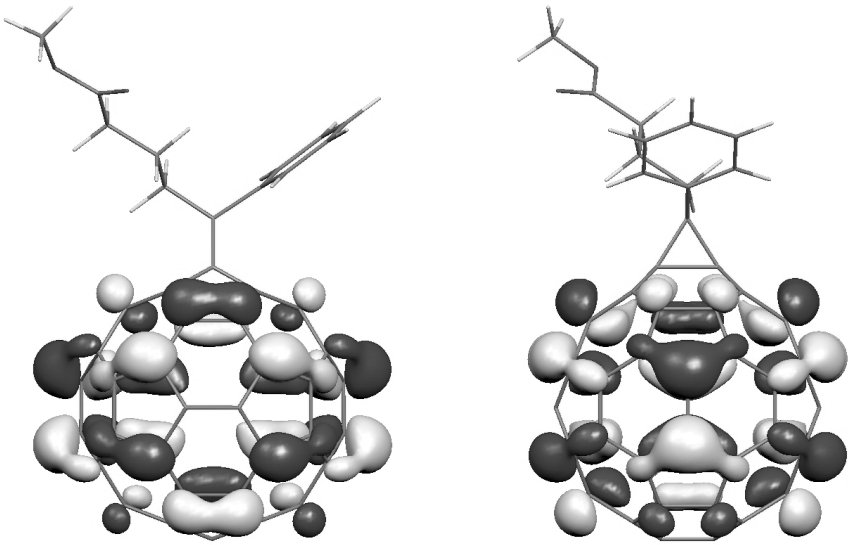

(b) $\Delta\rho$

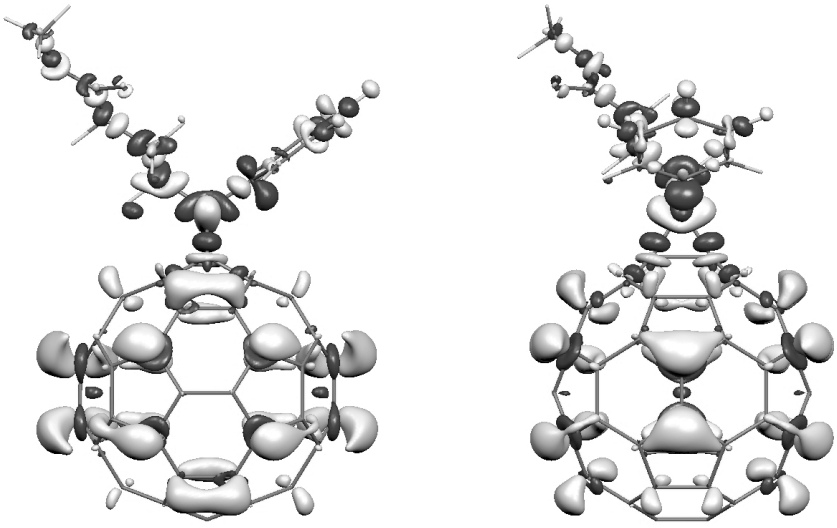

x-direction y-direction

Figure 4.4: (a) LUMO (isosurface value=0.025 a.u.), (b) $\Delta\rho$ (isosurface value=0.001 a.u.), of PCBM.

(a) v_{eff}

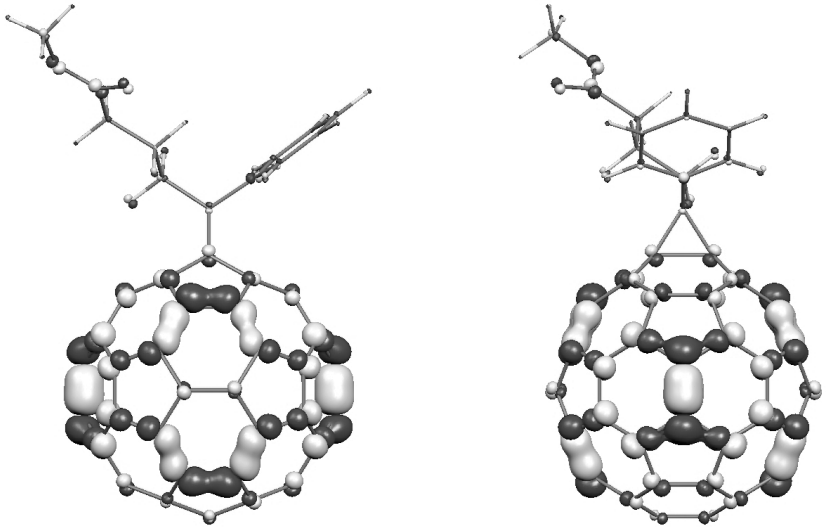

(b) η_{eff}

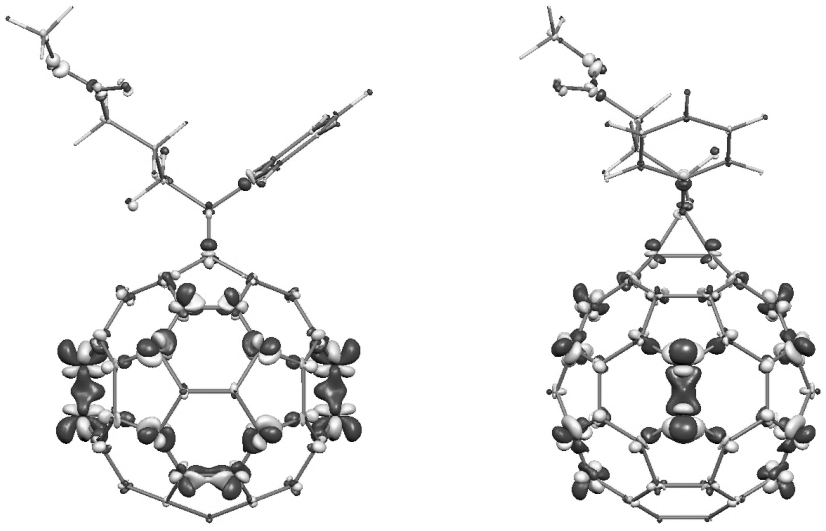

x-direction y-direction

Figure 4.5: (a) v_{eff} (isosurface value=0.005 a.u.) and (b) η_{eff} (isosurface value=5×10^{-6} a.u.) of the effective mode in PCBM.

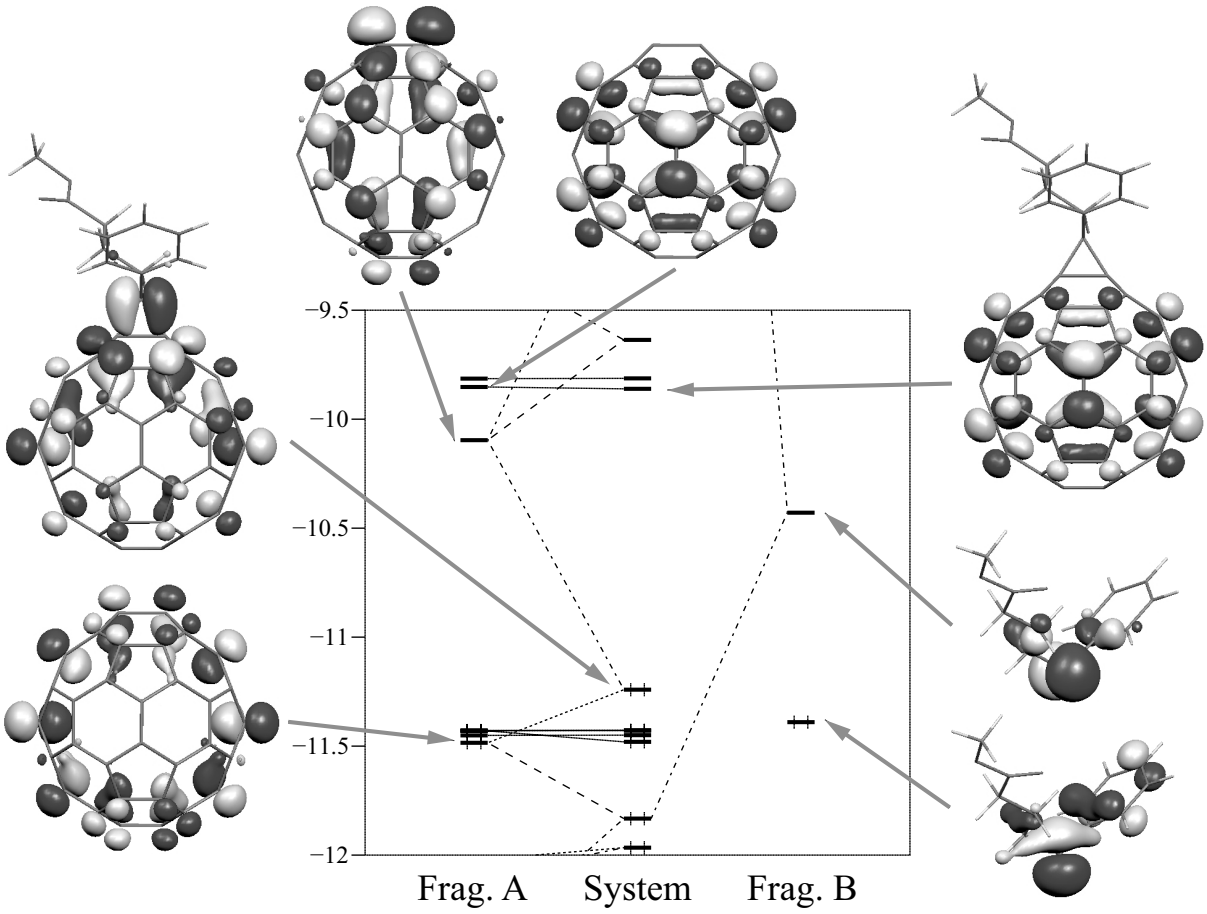

Figure 4.6: FMO analysis for PCBM. Threshold of the MO is 0.03 a.u. for the system and fragment A and 0.05 a.u. for the fragment B.

Part III

Miscellaneous Applications of the Vibronic Couplings

Chapter 1

Active Center Induced by Vibronic Interactions in V_2O_5/SiO_2

1.1 Introduction

Highly dispersed vanadium oxide on silica, V_2O_5/SiO_2, is a photocatalyst which promotes the oxidation of light alkenes [1–4]. The active species is the isolated VO_4, which has a C3v structure (see Fig. 1.1(a)) [5,6]. The vanadium oxide has two kinds of oxygen, basal oxygen (O_b) and terminal oxygen (O_t). The terminal oxygen reacts with a substrate in the photo-excited T_1 state [2, 3, 7]. Spectroscopy and molecular orbital calculation have revealed that the HOMO of the ground state consists of p orbitals of the basal oxygens, and LUMO's are doubly degenerate orbitals which originated from d orbitals of vanadium [8, 9]. The first triplet state is assigned to the excitation from the HOMO to the LUMO [9]. In the T_1 state, the frontier orbitals have no orbital coefficient on the terminal oxygen, although a substrate reacts with the terminal oxygen. In addition, a driving force of the ligand-to-metal charge transfer (LMCT) from the terminal oxygen to the vanadium is still open [8].

In this chapter, we will address these problems in terms of the vibronic coupling theory [10–12] using the density functional calculation as well as the vibronic model calculation. Vibronic coupling, or electron-phonon interaction, in a molecule with degenerate electronic state gives rise to a symmetry-lowering distortion, which is so called a Jahn-Teller distortion. We focus on the JT distortion in the molecule and discuss the reaction mechanism considering the vibronic coupling.

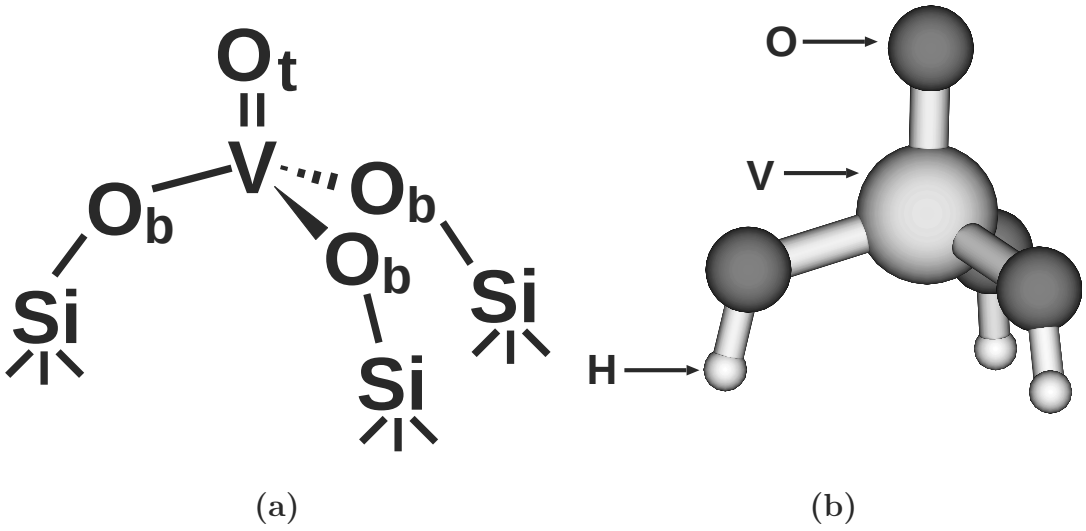

(a) (b)

Figure 1.1: (a) Isolated active species of highly dispersed vanadium oxide supported on silica, VO_4/SiO_2. There are two kinds of oxygen, terminal oxygen O_t and basal oxygen O_b. (b) Model molecule H_3VO_4.

1.2 Structures

We performed preliminary calculations for VO_4 clusters with some SiO_2 units. The orbitals corresponding to the HOMO in H_3VO_4 are largely localized on the VO_4. Accordingly, we employed H_3VO_4 as a model of the isolated VO_4 on silica (VO_4/SiO_2), where three Si atoms bonded with the O_b are replaced by hydrogen atoms (Fig. 1.1(b)). We optimized the singlet ground state and the triplet state of H_3VO_4 using the density functional method. We employed the B3LYP functional with a basis set, LANL2DZ for V, 6-31G(d) for O, and 6-31G for H. To obtain vibrational modes and frequencies, vibrational analyses were performed. For simplicity, we adopted the result of the ground state as vibrational modes of the present system. Molecular orbitals were obtained employing the extended Hückel method. All the density functional calculations and the extended Hückel calculations were performed using the Gaussian03 package [13].

For the ground state, we optimized the structure within the C_{3v} symmetry. The vibrational frequencies are tabulated in Table 1.1, and the vibrational a_1 and e modes are depicted in Fig. 1.2. One imaginary mode $a_2(1)$ remains in the C_{3v}-optimized structure, which will give rise to a distortion from C_{3v} to C_3 or lower symmetry. It is ascribed to the pseudo Jahn-Teller effect in the ground state.

Since this effect is not important in the present discussion, we simply refer the opti-

Table 1.1: Vibrational frequency (cm^{-1}) of X^1A_1 state of H_3VO_4. The asymmetric $a_2(1)$ mode with an imaginary frequency suggests that the pseudo Jahn-Teller effect occurs in the singlet ground state.

$a_1(1)$	255.4	$a_2(1)$	124.0 i	$e(1)$	216.6
$a_1(2)$	698.2			$e(2)$	294.4
$a_1(3)$	758.7			$e(3)$	407.1
$a_1(4)$	1151.7			$e(4)$	637.7
$a_1(5)$	3763.6			$e(5)$	799.9
				$e(6)$	3756.4

mized structure within the C_{3v} symmetry as the optimized structure.

On the other hand, for the triplet state, we obtained two C_s structures, one is a local minimum, and the other a saddle point with one imaginary frequency. Fig. 1.3 shows a schematic representation of the potential surface of the triplet state. At the middle, the potential surfaces conically intersect, and the minima are located along the trough which corresponds to the deformed structures. The minima are separated by the saddle points. This suggests that the Jahn-Teller effect occurs in the triplet state, and the vibronic coupling may play an important role in the mechanism of the photocatalytic reaction. In fact, in the C_s structure, the frontier orbitals have finite coefficients on the terminal oxygen, while, in the C_{3v} structure, the HOMO has no coefficient on the terminal oxygen at all. Therefore, the reaction center appears, and the LMCT occurs associated with the Jahn-Teller distortion. In other words, the vibronic coupling induces the active center of the photocatalyst. The effects on the frontier orbitals are discussed in detail in Sec. 1.3.

Since the electronic term of the photo-excited state is ^3E, the Jahn-Teller active vibrational modes are deduced from the symmetric product representation:

$$[E]^2 = a_1 \oplus e. \tag{1.1}$$

Thus, the Jahn-Teller active mode is an e mode. In the model molecule, H_3VO_4, there are five a_1 and six e modes. Among them, some vibrational modes significantly couple to the electronic state. To find such modes, the distortion from the ground state structure with the C_{3v} symmetry to the triplet state with the C_s symmetry was projected onto these

Table 1.2: Distortion of H_3VO_4 in the T_1 state from C_{3v} to C_s projected on the normal coordinates (amu$^{1/2}$Å).

$a_1(1)$	0.330	$e(1)$	-0.039
$a_1(2)$	0.390	$e(2)$	0.567
$a_1(3)$	0.438	$e(3)$	1.397
$a_1(4)$	0.607	$e(4)$	0.149
$a_1(5)$	-0.616	$e(5)$	0.132
		$e(6)$	0.436

vibrational modes. The result is summarized in Table 1.2. It is found that the $e(2)$ mode has large contribution to the Jahn-Teller distortion and the deformation of VO_4 is large. Thus, we concentrate ourselves on the $e(2)$ mode, for simplicity. The a_1 modes also couple to the electronic state, though they cannot lower the molecular symmetry, and they shift the orbital levels. Therefore, they can contribute to the deformation associated with the transition from the singlet ground state to the triplet state. Among them, the $a_1(4)$ mode is particularly important since it corresponds to a stretching mode of the V=O_t bonds which has been attributed to the progression in the emission spectra [7, 14, 15].

1.3 Vibronic model

As mentioned in the previous section, the $e(2)$ mode has the largest contribution to the Jahn-Teller distortion of VO_4 among the six e modes. Fig. 1.4 shows the change of the HOMO and NHOMO along the $e(2)$ mode. Note that we denote HOMO, next HOMO (NHOMO), and LUMO as those of the singlet ground state, not the triplet state, throughout this chapter. The orbital patterns and levels were calculated using the extended Hückel method in the DFT optimized structures [13]. The LUMO's originate from the d orbitals of the vanadium, and they are doubly degenerate, which results in the Jahn-Teller effect after the electronic excitation $E \leftarrow A_1$. In the NHOMO, the molecular orbital is localized on the terminal oxygen as well as the basal oxygens. The HOMO consists of the p orbitals of the basal oxygens and has no coefficients on the terminal oxygen as long as the molecular symmetry is C_{3v}. From Fig. 1.4, it is clear that the finite coefficient on the

terminal oxygen appears in the HOMO with the $e(2)$ deformation.

Since the LUMO level is doubly degenerate, denoted by e^*, the Jahn-Teller coupling exists between the LUMO's, denoted by θ^* and ϵ^*. In addition, the NHOMO's are also e, and they are denoted by θ and ϵ. The NHOMO's also couple to the e mode.

The Jahn-Teller active e mode can couple the e orbitals with a_2 and a_1 orbitals:

$$a_1 \otimes e = e, \qquad a_2 \otimes e = e. \tag{1.2}$$

Therefore, such off-diagonal couplings should be taken into account in the present model. Since an off-diagonal coupling is important as long as two levels are close, we consider the off-diagonal couplings between the HOMO (a_2) and NHOMO (e), and that between the NHOMO and HOMO-2 (a_1).

Accordingly, we set up the following vibronic Hamiltonian:

$$\begin{aligned}
\hat{H} &= \hat{H}_0 + \hat{H}_{\rm LJT} + \hat{H}_{\rm off-diag}, && (1.3)\\
\hat{H}_0 &= \sum_i \epsilon_i |i\rangle\langle i|, && (1.4)\\
\hat{H}_{\rm LJT} &= V_1 \left[(-|\theta^*\rangle\langle\theta^*| + |\epsilon^*\rangle\langle\epsilon^*|)\, Q_\theta + (-|\theta^*\rangle\langle\epsilon^*| + |\epsilon^*\rangle\langle\theta^*|)\, Q_\epsilon \right] \\
&+ V_3 \left[(-|\theta\rangle\langle\theta| + |\epsilon\rangle\langle\epsilon|)\, Q_\theta + (-|\theta\rangle\langle\epsilon| + |\epsilon\rangle\langle\theta|)\, Q_\epsilon \right], && (1.5)\\
\hat{H}_{\rm off-diag} &= V_2 \left[(|a_2\rangle\langle\epsilon| + |\epsilon\rangle\langle a_2|)\, Q_\theta + (-|a_2\rangle\langle\theta| + |\theta\rangle\langle a_2|)\, Q_\epsilon \right] \\
&+ V_4 \left[(|a_1\rangle\langle\theta| + |\theta\rangle\langle a_1|)\, Q_\theta + (|a_1\rangle\langle\epsilon| + |\epsilon\rangle\langle a_1|)\, Q_\epsilon \right], && (1.6)
\end{aligned}$$

where $i = a_1, \theta, \epsilon, a_2, \theta^*, \epsilon^*$, and ϵ_i denotes the orbital level of the molecular orbital i. $\hat{H}_0$ is the Hamiltonian without a distortion. $\hat{H}_{\rm LJT}$ describes the linear Jahn-Teller couplings of the e^* and e orbitals, respectively. $\hat{H}_{\rm off-diag}$ describes the off-diagonal coupling between the e and a_2 orbitals and that between the e and a_1 orbitals. V_1, V_2, V_3 and V_4 denote the corresponding orbital vibronic coupling constants.

We obtained the orbital vibronic coupling constants for the $e(2)$ mode by fitting the eigenvalues of the above Hamiltonian (1.3) to the orbital energy levels calculated using the extended Hückel method. The calculated constants are $V_1 = 1.2\ 10^{-1}$ eV/(amu$^{1/2}$Å), $V_2 = 3.3\ 10^{-2}$ eV/(amu$^{1/2}$Å), $V3 = -1.1\ 10^{-2}$ eV/(amu$^{1/2}$Å), $V4 = 2.5\ 10^{-2}$ eV/(amu$^{1/2}$Å).

Fig. 1.5 shows the eigenvalues of the vibronic Hamiltonian (1.3) with the parameters calculated above (solid lines) and the orbital level from the extended Hückel calculation (dotted lines). It is found that the Jahn-Teller stabilization mainly comes from the Jahn-Teller coupling V_1 of the LUMO e^*. Furthermore, the HOMO a_2 is slightly destabilized

against the Jahn-Teller distortion with the off-diagonal coupling V_2. The HOMO which has no coefficient on the O_t interacts with the NHOMO e via the Jahn–Teller-active mode e. Fig. 1.4 shows the orbital mixing of the HOMO and NHOMO. In other words, the whole system is stabilized by the Jahn-Teller coupling V_1, and, in the same time, the active center is induced by the off-diagonal vibronic coupling V_2 between the HOMO and NHOMO.

1.4 Conclusion

We calculated the optimized structure in the singlet ground and triplet excited states of the model molecule of vanadium oxide on silica, and the energy spectrum of the vibronic Hamiltonian. Major findings are as follows:

1. The optimized structures of the triplet state have C_s symmetry, which is ascribed to the Jahn-Teller effect.

2. The Jahn-Teller stabilization mainly comes from the orbital vibronic coupling of the LUMO e^* originated from the d orbitals of the vanadium with the e vibrational mode.

3. The off-diagonal vibronic coupling V_2 induces the active center in the photocatalytic reaction, while the whole system is stabilized with the Jahn-Teller coupling V_1.

Since the SOMO consists of the atomic orbitals of the basal oxygens as well as the terminal oxygen, the present result does not exclude the possibility of the reactivity on the basal oxygens. The JT effect contributes not only to the appearance of the active center on the terminal oxygen but also to the stabilization of the active center. Furthermore, it may contribute to the life time of the phosphorescent state, because of the reduction of a Franck-Condon factor.

Since the a_1 and e modes couple to the phosphorescent state, the emission spectrum should shed light on the vibronic structure in the present system. In the assignments published so far, explaining the various separations of the vibrational fine structure have failed since they have considered only the stretching of V=O_t bond ($a_1(4)$ mode) [7,14,15] or attributed the progression to a stretching of the V-O-Si ligands [9].

Our study reveals the crucial role of the e modes as well as the a1 modes in the phosphorescent state. Further study on the complete assignment of the phosphorescence spectra is now in progress. The result will be published in the future.

Bibliography

[1] S. Yoshida, Y. Magatani, S. Noda, and T. Funabiki, Chem. Commun. 601 (1981).

[2] S. Yoshida, T. Tanaka, M. Okada, and T. Funabiki, J. Chem. Soc. Faraday Trans. **80**, 119 (1984).

[3] T. Tanaka, M. Ooe, T. Funabiki, and S. Yoshida, J. Chem. Soc. Faraday Trans. **82**, 35 (1986).

[4] F. Amano, T. Tanaka, and T. Funabiki, Langmuir **20**, 4236 (2004).

[5] S. Yoshida, T. Tanaka, T. Hanada, T. Hiraiwa, H. Kanai, and T. Funabiki, Catal. Lett. **12**, 277 (1992).

[6] K. Teramura, T. Hosokawa, T. Ohuchi, T. Shishido, and T. Tanaka, Chem. Phys. Lett. **460**, 478 (2008).

[7] A. M. Gritscov, V. A. Shvets, and V. B. Kazansky, Chem. Phys. Lett. **35**, 511 (1975).

[8] H. Kobayashi, M. Yamaguchi, T. Tanaka, and S. Yoshida, J. Chem. Soc., Faraday Trans. **81**, 1513 (1985).

[9] K. Tran, M. A. Hanning-Lee, A. Biswas, A. E. Stiegman, and G. W. Scott, J. Am. Chem. Soc. **117**, 2618 (1995).

[10] I. B. Bersuker, *The Jahn-Teller Effect and Vibronic Interactions in Modern Chemistry* (PlenumNewYork, 1984).

[11] I. B. Bersuker, and V. Z. Polinger, *Vibronic Interactions in Molecules and Crystals* (Springer–VerlagBerlin and Heidelberg, 1989).

[12] I. B. Bersuker, *The Jahn–Teller Effect* (Cambridge University PressCambridge, 2006).

[13] M. J. Frisch, G. W. Trucks, H. B. Schlegel, G. E. Scuseria, M. A. Robb, J. R. Cheeseman, J. A. Montgomery, Jr., T. Vreven, K. N. Kudin, J. C. Burant, J. M. Millam, S. S. Iyengar, J. Tomasi, V. Barone, B. Mennucci, M. Cossi, G. Scalmani, N. Rega, G. A. Petersson, H. Nakatsuji, M. Hada, M. Ehara, K. Toyota, R. Fukuda, J. Hasegawa, M. Ishida, T. Nakajima, Y. Honda, O. Kitao, H. Nakai, M. Klene, X. Li, J. E. Knox, H. P. Hratchian, J. B. Cross, V. Bakken, C. Adamo, J. Jaramillo, R. Gomperts, R. E. Stratmann, O. Yazyev, A. J. Austin, R. Cammi, C. Pomelli, J. W. Ochterski, P. Y. Ayala, K. Morokuma, G. A. Voth, P. Salvador, J. J. Dannenberg, V. G. Zakrzewski, S. Dapprich, A. D. Daniels, M. C. Strain, O. Farkas, D. K. Malick, A. D. Rabuck, K. Raghavachari, J. B. Foresman, J. V. Ortiz, Q. Cui, A. G. Baboul, S. Clifford, J. Cioslowski, B. B. Stefanov, G. Liu, A. Liashenko, P. Piskorz, I. Komaromi, R. L. Martin, D. J. Fox, T. Keith, M. A. Al-Laham, C. Y. Peng, A. Nanayakkara, M. Challacombe, P. M. W. Gill, B. Johnson, W. Chen, M. W. Wong, C. Gonzalez, and J. A. Pople, *GAUSSIAN 03, Revision D.02*, Wallingford, CT, 2004.

[14] M. Anpo, I. Tanahashi, and Y. Kubokawa, J. Phys. Chem. **84**, 3440 (1980).

[15] M. Iwamoto, H. Furukawa, K. Matsukami, T. Takenaka, and T. Kagawa, J. Am. Chem. Soc. **105**, 3719 (1983).

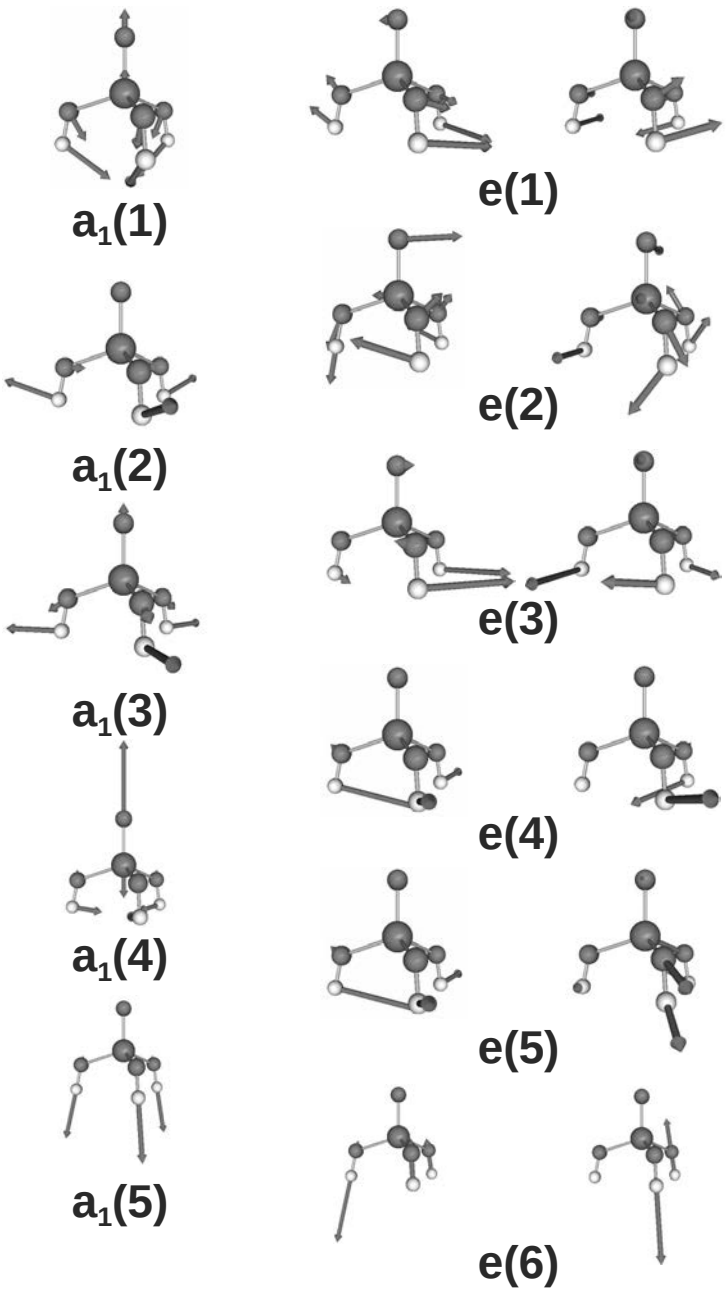

Figure 1.2: Vibrational a_1 and e modes of the X^1A_1 state.

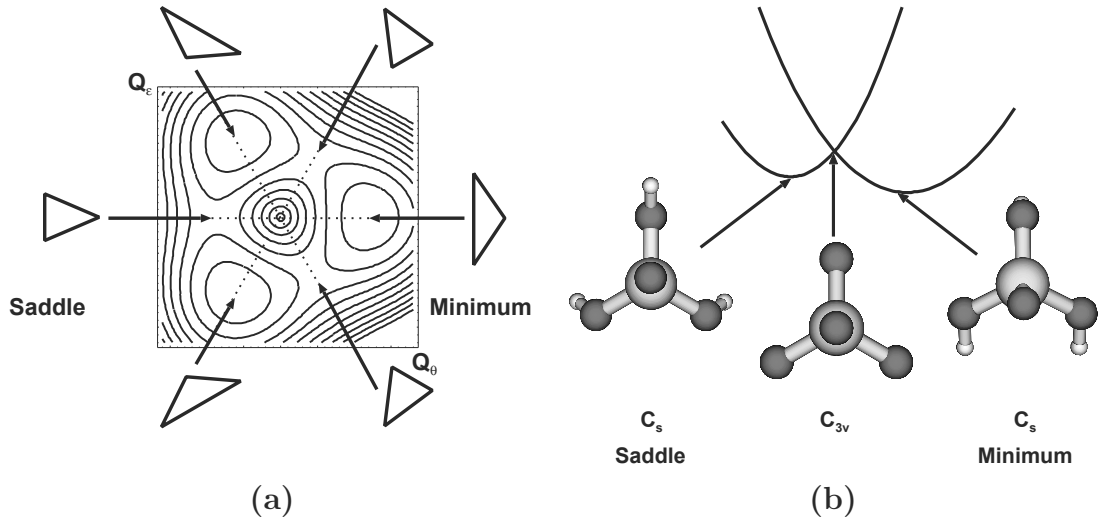

Figure 1.3: Schematic representation of the optimized structures and the Jahn-Teller potential surface in the triplet state. (a) The triangle indicates three basal oxygens (b) Cross section of the potential along the line between the minimum and the saddle point. At the center, the potential curves conically intersect.

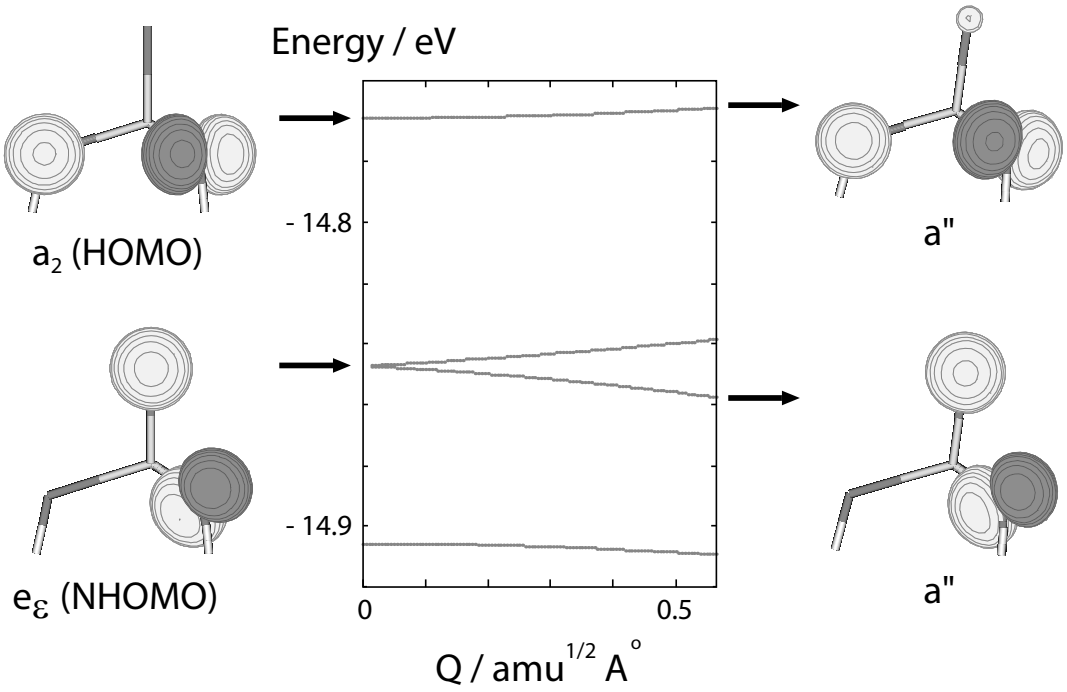

Figure 1.4: Orbital mixing of the HOMO a_2 and NHOMO e.

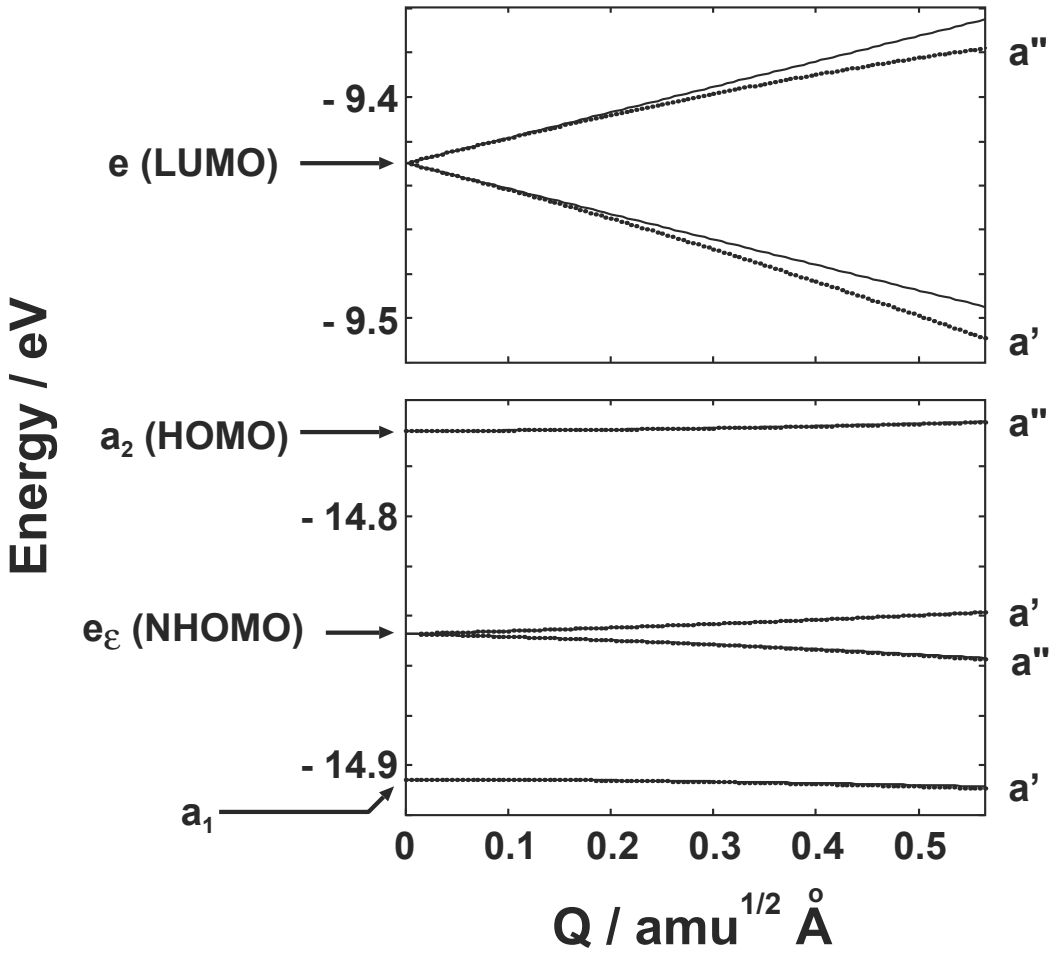

Figure 1.5: Orbital energy calculated using the extended Hückel method (dotted lines) and calculated energy spectrum of the vibronic Hamiltonian with the parameters (solid lines) as a function of the $e(2)$ normal coordinate.

Chapter 2

Molecular Design for High-Spin Molecules in View of Vibronic Couplings

2.1 Introduction

Aromatic amines have been paid to much attention for decades since they can exhibit a high-spin ground state [1, 2]. In 1950 Longuet-Higgins proved that the ground state of a molecule with *m*-xylene skeleton is expected to be a high-spin, triplet ground state [3]. Within the Hückel molecular orbital (HMO) approximation, molecules with a *m*-phenylene diamine (**1** in Figs. 2.1) skeleton can have pseudo-degenerate frontier orbitals which can result in a triplet ground state after oxidation. The Longuet-Higgins' theory has been a guiding principle for designing high-spin organic molecules. However, since the Longuet-Higgins' theory is based on the HMO theory, the ground state of such a molecule is not always a triplet because of the electronic correlation [4, 5] and structural relaxation.

Within higher approximations than the HMO theory, there remains a pseudo degeneracy in the frontier level. A degeneracy or pseudo degeneracy of frontier orbitals is crucial to realize high-spin molecules. However, the Jahn-Teller or pseudo Jahn-Teller effect reduces the degeneracy or pseudo degeneracy due to the vibronic couplings, or electron-vibration interactions [6, 7]. Strong vibronic couplings (VC) cause the level splitting of the frontier level and stabilize the closed-shell singlet state with a structural relaxation. When the structural stabilization energy of the closed-shell singlet ΔE_{S} is smaller enough

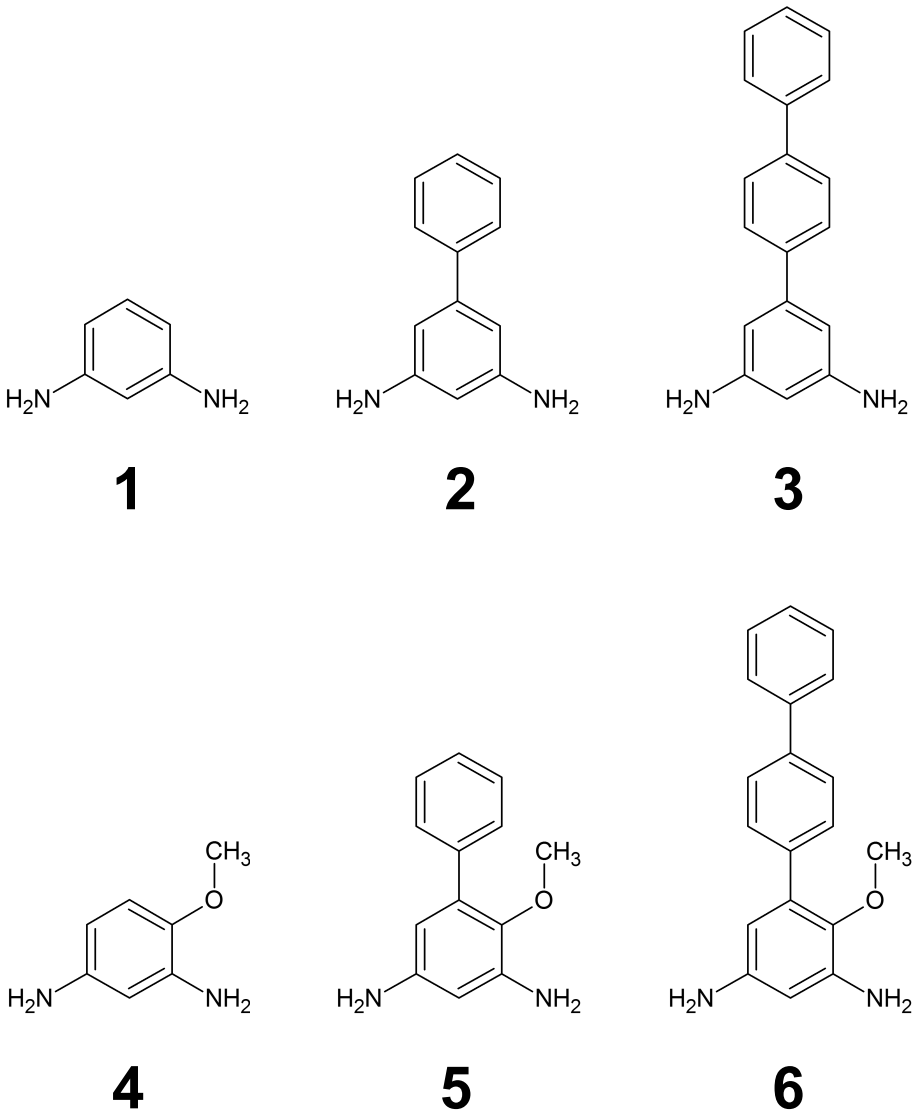

Figure 2.1: Target molecules.

than that of the triplet ΔE_{T}, the ground state can be a triplet (see Figs. 2.2). Thus, in order to design a high-spin molecule, the stabilization energy ΔE_{S} which is ascribed to the VCs in the singlet state should be reduced.

To analyze the strength of the VC, or vibronic coupling constant (VCC), we have proposed vibronic coupling density (VCD) [8, 9]. Based on the concept of the VCD, we can discuss the VCs from the relations between the electronic and vibrational structures of a molecule. Furthermore, we can control the VCs by designing the molecular structure.

In this article, we focus on *m*-phenylene diamine **1** and its derivatives (**2**-**6**) shown in Figs. 2.1. We evaluate their VCCs and analyzed them in terms of the concept of the

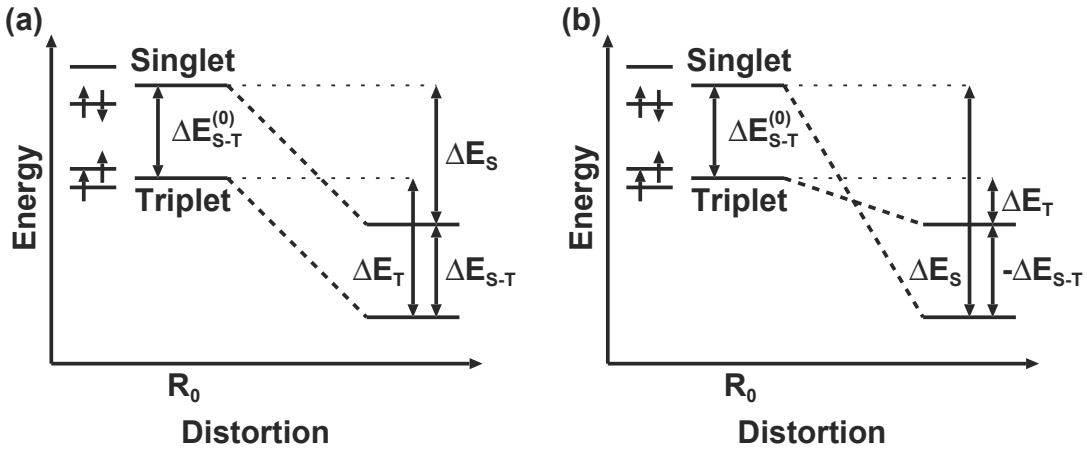

Figure 2.2: Relation between the ground electronic state and the stabilization due to structural relaxation. (a) The vibronic coupling of the singlet electronic state is weak, and the ground electronic state is a triplet. (b) The vibronic coupling of the singlet electronic state is strong, and the ground electronic state is a closed-shell singlet.

VCD. Since the dication of **4** has the closed-shell singlet ground state at the equilibrium geometry, our goal is to find a substituent group which makes the ground state of the dicationic state of **4** a triplet.

2.2 Vibronic coupling constant and vibronic coupling density

The strength of the VC with respect to vibrational mode α is defined by the VCC V_α [6, 7, 9]:

$$V_\alpha = \left\langle \Psi \left| \left(\frac{\partial H_e(\mathbf{R})}{\partial Q_\alpha} \right)_{\mathbf{R}_0} \right| \Psi \right\rangle, \tag{2.1}$$

where $\mathbf{R}$ is the set of the nuclear coordinates of a molecule, $\mathbf{R}_0$ the reference geometry, Q_α the mass-weighted normal coordinate of mode α, $H_e(\mathbf{R})$ the electronic Hamiltonian of the dication, and Ψ the electronic wavefunction of $H_e(\mathbf{R}_0)$. The reference geometry $\mathbf{R}_0$ is the equilibrium structure of the neutral *m*-phenylene diamine or its derivative. Applying the Hellmann–Feynman theorem [10] for Eq. (2.1), the VCC is rewritten as follows:

$$V_\alpha = \left(\frac{\partial E(\mathbf{R})}{\partial Q_\alpha} \right)_{\mathbf{R}_0} \tag{2.2}$$

$$= \sum_A \left(\frac{\partial E(\mathbf{R})}{\partial \mathbf{R}_A} \right)_{\mathbf{R}_0} \cdot \frac{\mathbf{u}_A^\alpha}{\sqrt{M_A}}, \tag{2.3}$$

where $E(\mathbf{R})$ is the eigenvalue of $H_e(\mathbf{R})$, $\mathbf{R}_A$ the position of Ath nucleus, $\mathbf{u}_A^\alpha$ the 3D components of the Ath nucleus of the normal modes α, and M_A the nuclear mass. In the calculation of the VCCs, Eq. (2.3) is employed.

To analyze the VCCs, we use the concept of the VCD [8,9] which gives a local picture of the VC. The VCC V_α is written as a space integral of the VCD η_α:

$$V_\alpha = \int \eta_\alpha(\mathbf{r}) d\mathbf{r}, \tag{2.4}$$

where $\eta_\alpha(\mathbf{r})$ is defined by the product of the electron-density difference $\Delta\rho(\mathbf{r})$ and the potential derivative $v_\alpha(\mathbf{r})$ [8,9]:

$$\eta_\alpha(\mathbf{r}) = \Delta\rho(\mathbf{r}) v_\alpha(\mathbf{r}), \tag{2.5}$$

where the electron-density difference $\Delta\rho(\mathbf{r})$ is defined by the difference of the one-electron density of the system $\rho(\mathbf{r})$ and reference system $\rho_0(\mathbf{r})$:

$$\Delta\rho(\mathbf{r}) = \rho(\mathbf{r}) - \rho_0(\mathbf{r}). \tag{2.6}$$

The potential derivative $v_\alpha(\mathbf{r})$ is expressed as

$$v_\alpha(\mathbf{r}) = \left[\frac{\partial}{\partial Q_\alpha} \left(\frac{-Z_A}{|\mathbf{r} - \mathbf{R}_A|} \right) \right]_{\mathbf{R}_0} \tag{2.7}$$

$$= \sum_A - \frac{Z_A (\mathbf{r} - \mathbf{R}_{0,A})}{|\mathbf{r} - \mathbf{R}_{0,A}|^3} \cdot \frac{\mathbf{u}_A^\alpha}{\sqrt{M_A}}. \tag{2.8}$$

$\Delta\rho(\mathbf{r})$, $v_\alpha(\mathbf{r})$, and $\eta_\alpha(\mathbf{r})$ give information about the origin of the VC. If the electron-density difference $\Delta\rho$ is localized not on bonds but on atoms, the VCCs become small [11]. Based on an analysis for the distribution of $\Delta\rho$, we have succeeded in designing an electron-transporting molecule for organic light-emitting diodes [12]. Thus, in this article, we focus on the electron-density difference $\Delta\rho$.

We performed density-functional theory (DFT) calculation with the B3LYP functional [13] to obtain the optimized geometries, the normal modes $\mathbf{u}_A^\alpha$, and the gradient of the total electronic energy $(\partial E(\mathbf{R})/\partial \mathbf{R}_A)_{\mathbf{R}_0}$. For the neutral and closed-shell singlet states of the dications, we used the spin restricted B3LYP method. For the triplet states of the dications, we employed the spin unrestricted B3LYP method. The basis set is the triple zeta cc-pVTZ. In addition, the time-dependent DFT calculations with the B3LYP functional were performed to confirm the assumption that the triplet and closed-shell singlet states are more stable than the open-shell singlet states for **1**, **4**, and **6**. The calculation for the electronic and vibrational structures were performed using Gaussian 03 [14].

2.3 Results and discussion

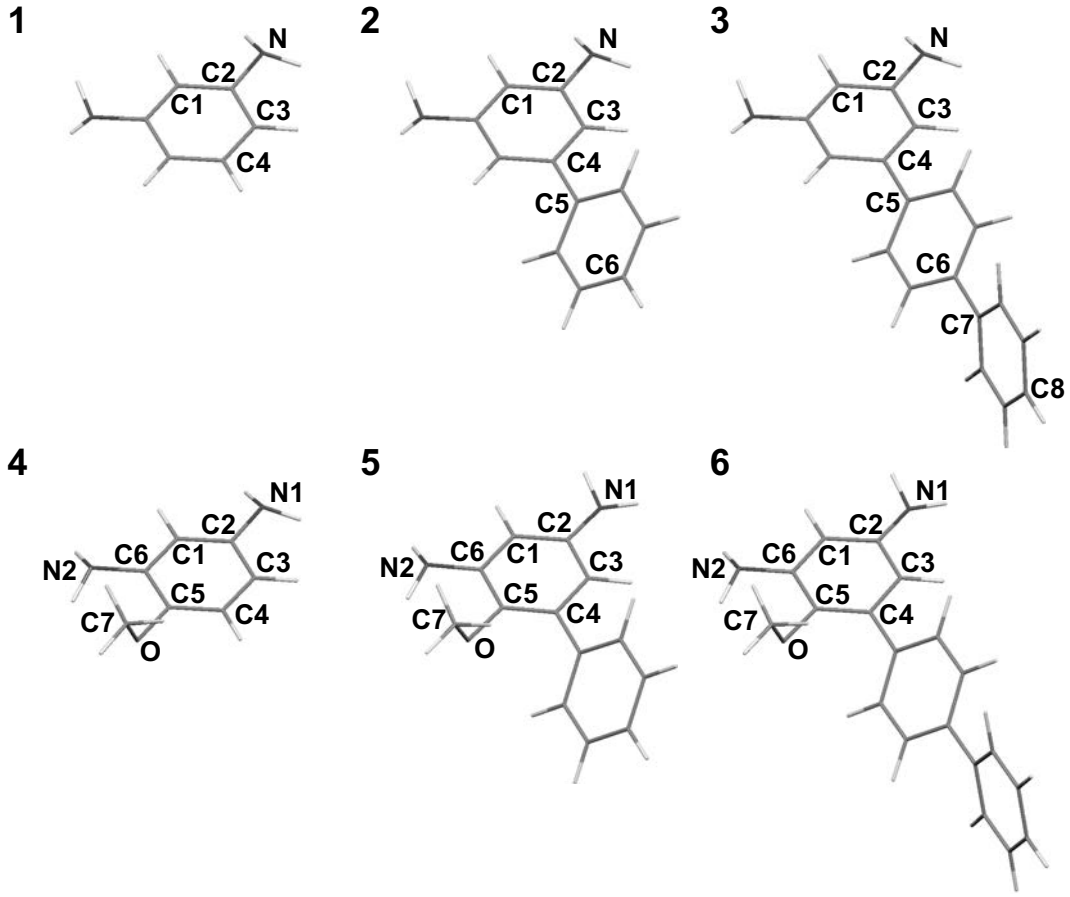

Figure 2.3: Equilibrium geometries in the neutral states.

We optimized the geometries of the target molecules (Figs. 2.1) in the neutral and dication states. The equilibrium geometries of the neutral molecules are shown in Figs. 2.3. The optimized geometries of molecules **1**, **2**, and **3** are C_2 symmetry. The C_2 axis intersects the carbon atoms C1 and C4 in **1**, C1, C4, C5, and C6 in **2**, and C1, C4, C5, C6, C7, and C8 in **3**. (labels of nuclei are shown in Figs. 2.3). On the other hand, the optimized geometries of **4**, **5**, and **6** are C_1 symmetry.

For all the molecules, the total electronic energy of the triplet states are lower than those of the closed-shell singlet states at the reference geometries $\mathbf{R}_0$ as expected from the Longuet-Higgins's theory (see the energy gap $\Delta E^{(0)}_{S-T}$ in Table 2.1). Although all the triplet states are the ground state at the reference geometries, the structural relaxations must be taken into account since the dications have nonzero vibronic coupling constants.

Since molecules **1**, **2**, and **3** belong to the C_2 symmetry, the electronic states of the

Table 2.1: Energy gaps in meV between the singlet and triplet states at the reference geometries $\Delta E^{(0)}_{S-T}$ and at the equilibrium geometry ΔE_{S-T}. Relaxation energies of the singlet and triplet states in meV, E_S and E_T, respectively. The negative values of ΔE_{S-T} denote that the ground state is a closed-shell singlet.

	1	**2**	**3**	**4**	**5**	**6**
$\Delta E^{(0)}_{S-T}$	544	902	803	177	534	624
ΔE_T	760	624	605	1468	849	731
ΔE_S	964	833	702	2219	1433	1033
ΔE_{S-T}	341	693	706	−574	−50	322

dications couple with only totally symmetric a modes. Molecules **1**, **2**, and **3** have 20, 34, and 48 a modes, respectively. On the other hand, since the symmetry of **4**, **5**, and **6** is C_1, the electronic states couple with all the vibrational modes. The number of the modes are 56, 84, and 114 modes, respectively.

Figs. 2.4 show the VCCs of the dications $\mathbf{1}^{2+}$, $\mathbf{2}^{2+}$, and $\mathbf{3}^{2+}$. In the case of $\mathbf{1}^{2+}$, the VCCs of the singlet state tend to be larger than those of the triplet state. However, the ground electronic state at the relaxed structure is a triplet (see ΔE_{S-T} in Table 2.1) since the energy gap at $\mathbf{R}_0$ between the singlet and triplet states $\Delta E^{(0)}_{S-T}$ is large enough. Among twenty active a modes, the $a(14)$ mode (1630 cm^{-1}. **1a** in Figs. 2.6) has the largest value (-6.66×10^{-4} a.u.) in the singlet $\mathbf{1}^{2+}$. The potential derivative of the C-C stretching mode $v_{a(14)}$ is shown as **1b** in Figs. 2.6. Since both the electron-density difference of the singlet state (**1b** in Figs. 2.5) and potential derivative are localized on the bonds between C2 and C3, the coupling constant is large. On the other hand, $\Delta\rho$ of the triplet state (**1a** in Figs. 2.5) is localized not on the bonds but on C3 atoms. Therefore, the VCC of the triplet state (-0.26×10^{-4} a.u.) is smaller than the VCC of the singlet state (-6.66×10^{-4} a.u.).

In order to stabilize the triplet state of $\mathbf{1}^{2+}$, it is desired to reduce the strength of the VC in the singlet state. We introduced a phenyl or biphenyl group to the *m*-phenylene diamine as a substituent group. The position of the substituent is chosen so that the symmetry of the system is kept (**2** and **3** in Figs. 2.3).

The electron-density differences of $\mathbf{2}^{2+}$ and $\mathbf{3}^{2+}$ are displayed in Figs. 2.5. In com-

parison with $\Delta\rho$ of $\mathbf{1}^{2+}$, $\Delta\rho$'s of $\mathbf{2}^{2+}$ and $\mathbf{3}^{2+}$ decrease on the *m*-phenylene diamine. The maximum-coupling mode of $\mathbf{2}^{2+}$ in the singlet state is the $a(25)$ mode (1636 cm^{-1}. **2a** in Figs. 2.6). This mode is localized on *m*-phenylene diamine and corresponds to the $a(14)$ mode of **1**. However, the VCC of the $a(25)$ mode (-4.81×10^{-4} a.u.) is smaller than that of the $a(14)$ mode of the singlet $\mathbf{1}^{2+}$ because $\Delta\rho$ of the singlet state tends to be localized on C3 atoms in **2**. The $a(36)$ mode of **3** (1635 cm^{-1}. **3a** in Figs. 2.6) also is localized on *m*-phenylene diamine, however, the VCC of the singlet is smaller (3.23×10^{-4} a.u.) than that of $\mathbf{1}^{2+}$. It should be noted that $\Delta\rho$'s in **3** are strongly localized on N and C3 atoms for the triplet state and N and C1 atoms for the singlet state. These localizations on the atoms are responsible for the small VCCs in **3**. This is the most important effect of the biphenyl as a substituent group.

Besides the modes which originate from the *m*-phenylene diamine, **2** and **3** have modes that originate from the phenyl and biphenyl groups. For instance, **2** and **3** have C-C stretching modes of the phenyl ($a(26)$, 1644 cm^{-1}) and biphenyl ($a(37)$, 1643 cm^{-1}) groups. The couplings of these modes are rather strong in both the singlet and triplet states. Moreover, the $a(37)$ mode of **3** is the maximum-coupling mode in the singlet state (-4.16×10^{-4} a.u.). However, in spite of the additional modes of substituents in **2** and **3**, the maximum VCCs are reduced from the values of **1** due to the localization of $\Delta\rho$'s on the atoms. Consequently, the stabilization energies ΔE_S are decreased and the gaps between the singlet and triplet at the relaxed structures ΔE_{S-T} are increased, i.e., the triplet state is stabilized (see the Table 2.1).

The ground state of molecule $\mathbf{4}^{2+}$ is a closed-shell singlet state (see the Table 2.1). The VCCs of $\mathbf{4}^{2+}$ are shown in Figs. 2.7 (**4a** and **4b**). The magnitude of the strongest VCC of $\mathbf{4}^{2+}$ is as large as that of $\mathbf{1}^{2+}$ since the patterns of $\Delta\rho$ of the triplet and singlet $\mathbf{4}^{2+}$ (**4a** and **4b** in Figs. 2.8) are similar to those of $\mathbf{1}^{2+}$. Furthermore, as mentioned above, $\mathbf{4}^{2+}$ has more than twice as many active modes as $\mathbf{1}^{2+}$, the couplings as a whole are stronger than those of $\mathbf{1}^{2+}$. In consequence, the stabilization energy ΔE_S of $\mathbf{4}^{2+}$ is increased and the ground state after the structural relaxation is a closed-shell singlet (Table 2.1).

Even in the case of $\mathbf{4}^{2+}$, it is possible to make the ground state a triplet state introducing an appropriate substituent group for $\mathbf{4}^{2+}$. The $\Delta\rho$ of $\mathbf{5}^{2+}$ and $\mathbf{6}^{2+}$ are shown in Figs. 2.8. It should be noted that the $\Delta\rho$'s on the bonds between C2-C3 and C5-C6 in **4** and **5** are disappeared in **6**. Moreover, there is little $\Delta\rho$ on the biphenyl. The electron-

density difference of $\mathbf{6}^{2+}$ is strongly localized on C5 atoms (C5 is shown in Figs. 2.3), hence the localized $\Delta\rho$ does not contribute to the VCCs significantly. Thereby the VCCs in $\mathbf{6}^{2+}$ are weakened (**6** in Figs. 2.7), and the ground state of $\mathbf{6}^{2+}$ is a triplet in spite of its low symmetry. From view of the electronic theory of organic chemistry, **6** would not be favorable as a high-spin molecule because of the following reasons: (1) the electron-donating/withdrawing character of the substituents would reduce the localization of the spins on N atoms, (2) many quinoid-type structures which yield a large structural relaxation would contribute to the resonance structures of $\mathbf{6}^{2+}$. Therefore, it is surprising that the ground state of $\mathbf{6}^{2+}$ is theoretically predicted to be a triplet. However, we can realize the stability of the triplet state based on the VCD theory.

2.4 Summary

We investigated a relation between the vibronic coupling and the ground electronic states of the derivatives of *m*-phenylene diamines. To stabilize the high-spin state, the vibronic coupling of the low-spin state should be reduced. In order to reduce the VCCs, the localization of the electron-density difference on atoms are effective.

Bibliography

[1] J. A. Crayston, J. N. Devine, and J. C. Walton, Tetrahedron **56**, 7829 (2000).

[2] A. Ito, and K. Tanaka, Pure Appl. Chem. **82**, 979 (2010).

[3] H. C. Longuet-Higgins, J. Chem. Phys. **18**, 265 (1950).

[4] A. A. Ovchinnikov, Theoret. Chim. Acta **47**, 297 (1978).

[5] W. T. Borden, and E. R. Davidson, J. Am. Chem. Soc. **99**, 4587 (1976).

[6] I. B. Bersuker, and V. Z. Polinger, *Vibronic Interactions in Molecules and Crystals* (Springer–VerlagBerlin and Heidelberg, 1989).

[7] I. B. Bersuker, *The Jahn–Teller Effect* (Cambridge University PressCambridge, 2006).

[8] T. Sato, K. Tokunaga, and K. Tanaka, J. Phys. Chem. A **112**, 758 (2008).

[9] T. Sato, K. Tokunaga, N. Iwahara, K. Shizu, and K. Tanaka, in *The Jahn–Teller Effect: Fundamentals and Implications for Physics and Chemistry*, edited by H. Köppel, D. R. Yarkony, and H. Barentzen (Springer–VerlagBerlin and Heidelberg, 2009), p. 99.

[10] R. P. Feynman, Phys. Rev. **56**, 340 (1939).

[11] T. Sato, K. Shizu, T. Kuga, K. Tanaka, and H. Kaji, Chem. Phys. Lett. **458**, 152 (2008).

[12] K. Shizu, T. Sato, and K. Tanaka, Chem. Phys. Lett. **491**, 65 (2010).

[13] A. D. Becke, J. Chem. Phys. **98**, 5648 (1993).

[14] M. J. Frisch, G. W. Trucks, H. B. Schlegel, G. E. Scuseria, M. A. Robb, J. R. Cheeseman, J. A. Montgomery, Jr., T. Vreven, K. N. Kudin, J. C. Burant, J. M. Millam, S. S. Iyengar, J. Tomasi, V. Barone, B. Mennucci, M. Cossi, G. Scalmani, N. Rega, G. A. Petersson, H. Nakatsuji, M. Hada, M. Ehara, K. Toyota, R. Fukuda, J. Hasegawa, M. Ishida, T. Nakajima, Y. Honda, O. Kitao, H. Nakai, M. Klene, X. Li, J. E. Knox, H. P. Hratchian, J. B. Cross, V. Bakken, C. Adamo, J. Jaramillo, R. Gomperts, R. E. Stratmann, O. Yazyev, A. J. Austin, R. Cammi, C. Pomelli, J. W. Ochterski, P. Y. Ayala, K. Morokuma, G. A. Voth, P. Salvador, J. J. Dannenberg, V. G. Zakrzewski, S. Dapprich, A. D. Daniels, M. C. Strain, O. Farkas, D. K. Malick, A. D. Rabuck, K. Raghavachari, J. B. Foresman, J. V. Ortiz, Q. Cui, A. G. Baboul, S. Clifford, J. Cioslowski, B. B. Stefanov, G. Liu, A. Liashenko, P. Piskorz, I. Komaromi, R. L. Martin, D. J. Fox, T. Keith, M. A. Al-Laham, C. Y. Peng, A. Nanayakkara, M. Challacombe, P. M. W. Gill, B. Johnson, W. Chen, M. W. Wong, C. Gonzalez, and J. A. Pople, *GAUSSIAN 03, Revision D.02*, Wallingford, CT, 2004.

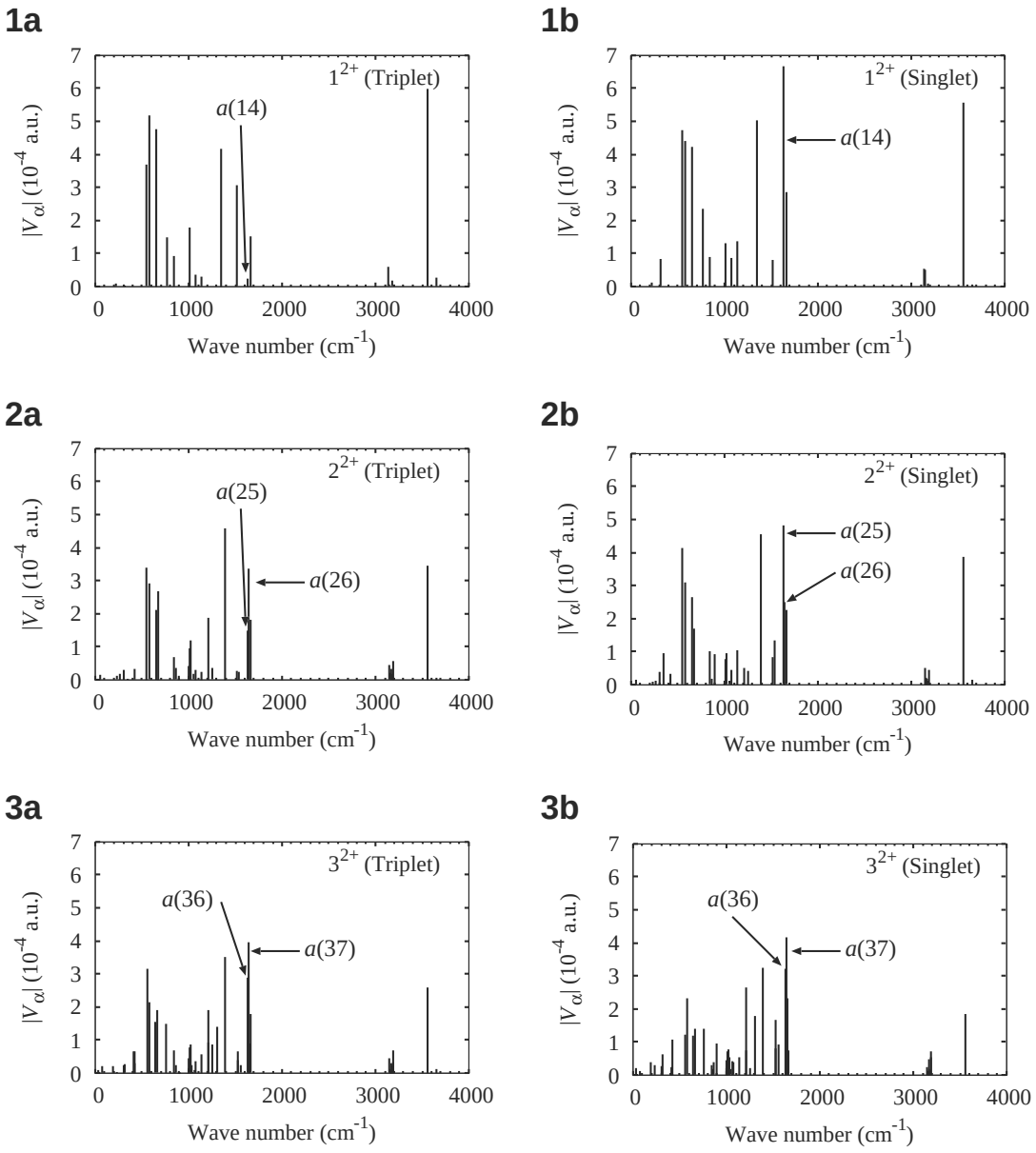

Figure 2.4: Absolute values of VCCs of $\mathbf{1}^{2+}$, $\mathbf{2}^{2+}$, and $\mathbf{3}^{2+}$ (10^{-4} a.u.). **1**, **2**, and **3** in the figure correspond to the numbers of molecules in Figs. 2.1. **1a-3a** are the VCCs of the triplet states. **1b-3b** are the VCCs of the singlet states.

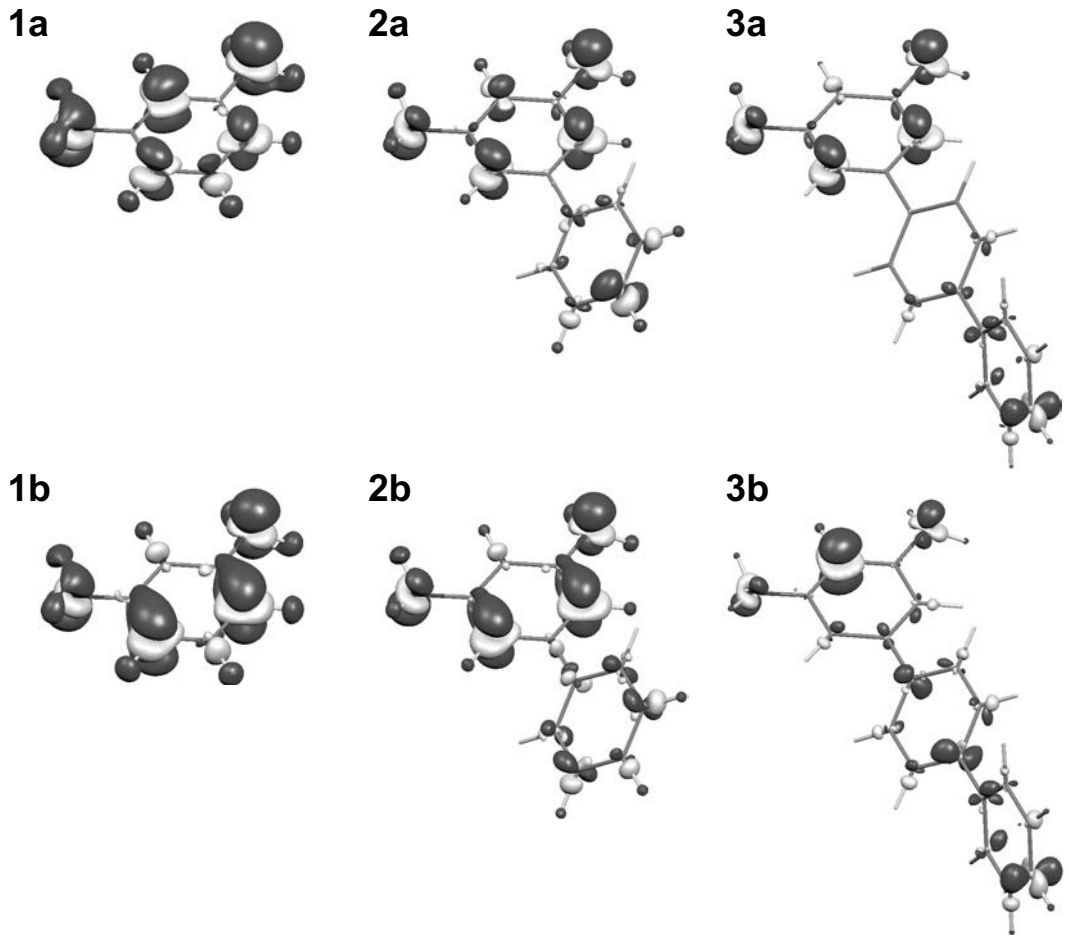

Figure 2.5: Electron-density difference $\Delta\rho$. **1a-3a** are $\Delta\rho$ of the triplet states. **1b-3b** are $\Delta\rho$ of the singlet states. The isosurface value of $\Delta\rho$ is 0.008 a.u..

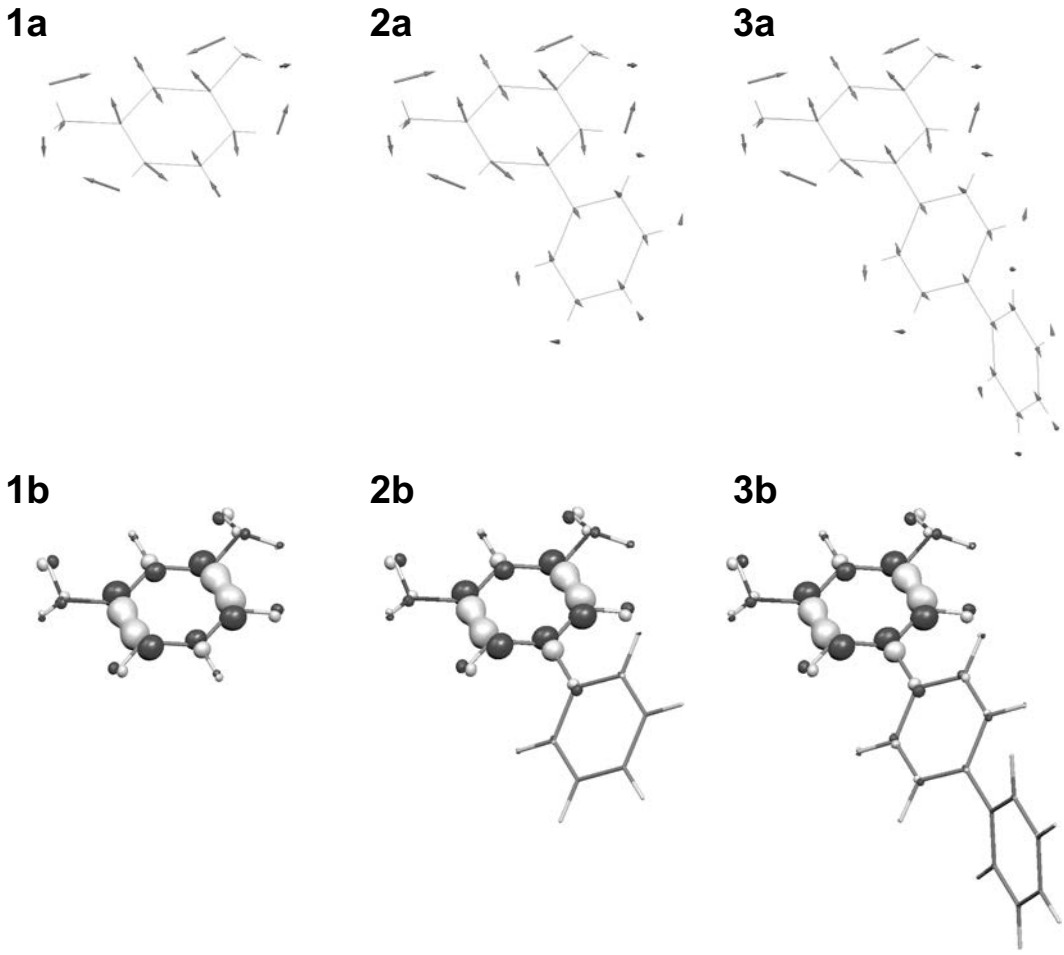

Figure 2.6: **1a**, **2a**, and **3a** correspond to the $a(14)$ of **1**, $a(25)$ of **2**, and $a(36)$ of **3** modes, respectively. **1b**, **2b**, and **3b** are the potential derivatives. The isosurface value of the potential derivative $v_{a(i)}$ is 0.015 a.u..

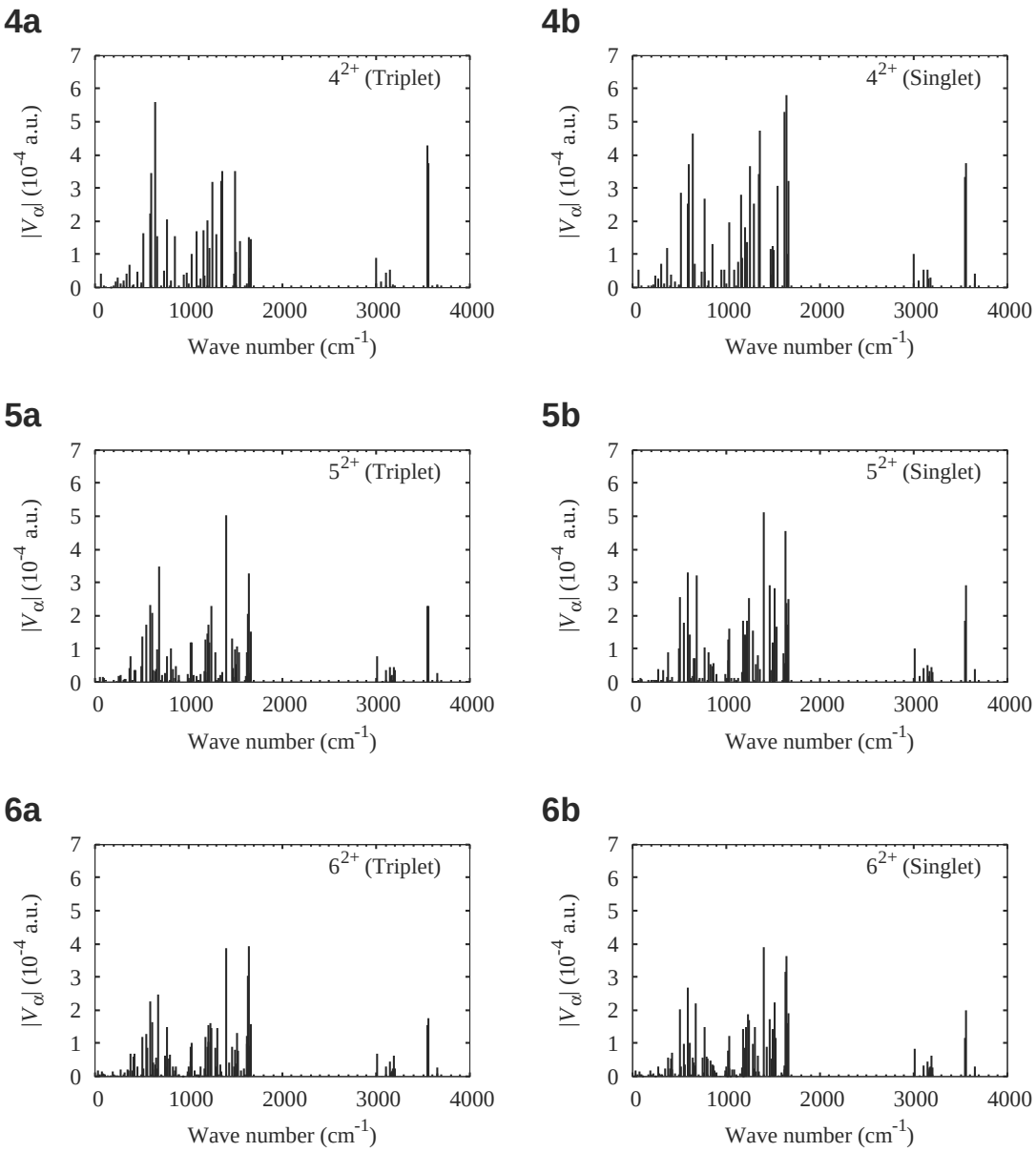

Figure 2.7: Absolute values of VCCs of $\mathbf{4}^{2+}$, $\mathbf{5}^{2+}$, and $\mathbf{6}^{2+}$ (10^{-4} a.u.). **4**, **5**, and **6** in the figure correspond to the numbers of molecules in Figs. 2.1. **4a-6a** are the VCCs of the triplet states. **4b-6b** are the VCCs of the singlet states.

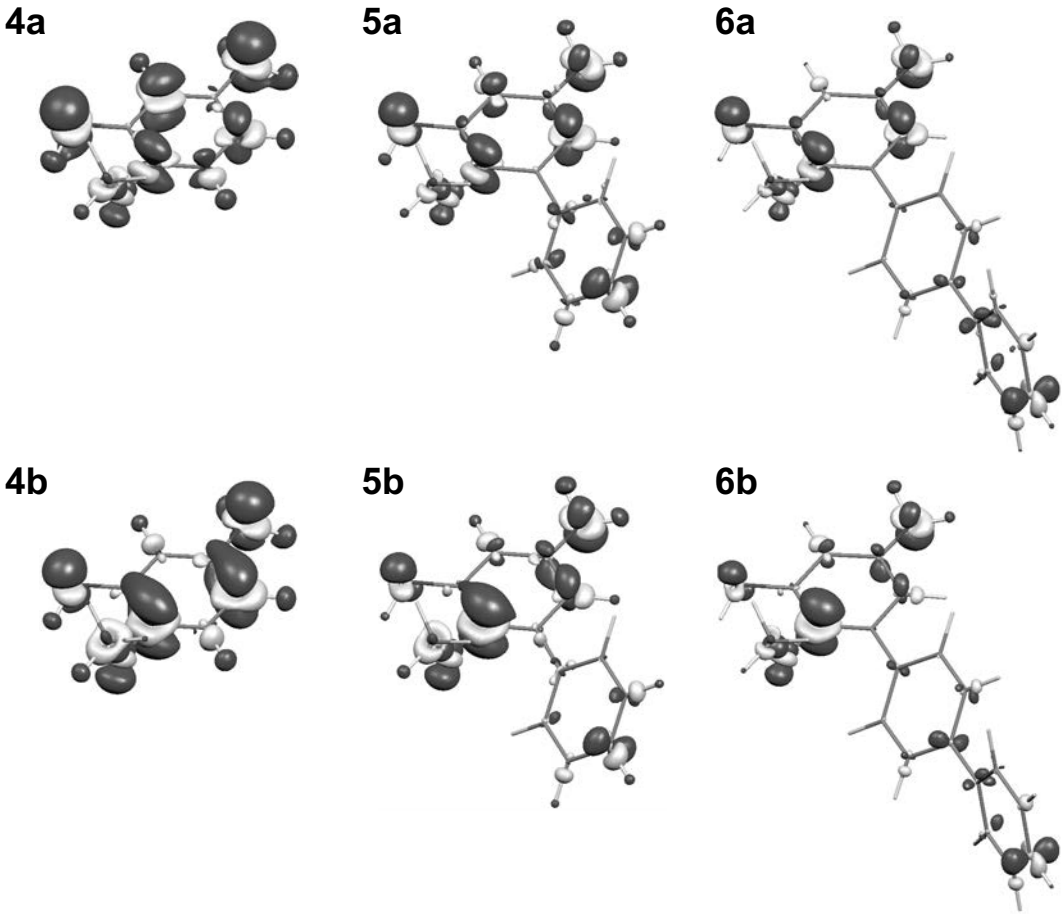

Figure 2.8: Electron-density difference $\Delta\rho$. **4a-6a** are $\Delta\rho$ of the triplet states. **4b-6b** are $\Delta\rho$ of the singlet states. The isosurface value of $\Delta\rho$ is 0.008 a.u..

Chapter 3

Vibronic Couplings in Picene from View of Vibronic Coupling Density Analysis

After the discovery of the superconductivity in alkali-metal (K, Rb) doped picene, [1] experimental and theoretical studies on the electronic structure on the picene have been piled up. [2–14] The vibronic coupling (electron-vibration coupling) [15] is an important interaction in the electronic properties such as superconductivity. Okazaki *et al.* have discussed an importance of the vibronic couplings in doped picene based on their photoelectron spectra (PES) [2]. Therefore, evaluation of the vibronic coupling constants (VCC) is crucial to discuss electronic properties of doped picenes. Some authors have published the VCCs of picene anions [10, 11, 16, 17]. However, some of the calculated VCCs are controversial. Subedi and Boeri have concluded that the electron-phonon coupling of the modes around 1600 cm^{-1} are strong [10], while those calculated by Kato *et al* are weak in this region [11, 16, 17].

Vibronic effects can be experimentally observed in spectra. [15] Roth *et al.* measured electron energy loss spectrum (EELS) of pristine picene at 20 K [5]. They have observed vibronic progressions in the EELS of the intramolecular excitation to $S_2(^1B_2)$ state.

We have recently published calculation of the VCCs in C_{60}^- from the gradients of the total energies [18]. The results are consistent with the experimental observation of the PES by Wang *et al.* [19]. We have proposed a concept, *vibronic coupling density* (VCD) [20,21]. Based on the vibronic coupling density, we can discuss vibronic couplings from view of

electronic and vibrational structures. On the basis of the VCD analysis, we have succeeded in designing carrier-transporting molecules with small vibronic couplings which is required in organic electronics such as organic light-emitting diodes (OLED) [22, 23].

In this chapter, we present the VCCs of the excited, monoanionic, and trianionic states of picene based on the same method of calculation employed in the calculation for C_{60}^{-}. Using the VCCs of the excited $^1B_2$ state, we simulate EELS and compare the spectrum with the experimental one [5]. From the view of the VCD analysis, we critically discuss the previous VCCs in Refs. [11, 16, 17].

We evaluated VCCs of mode α V_α from the gradients of the adiabatic potential energy surface E with respect to a mass-weighted normal coordinates Q_α [18, 22–24]:

$$V_\alpha = \left\langle \Psi \left| \left(\frac{\partial \hat{H}}{\partial Q_\alpha} \right)_{\mathbf{R}_0} \right| \Psi \right\rangle = \left(\frac{\partial E}{\partial Q_\alpha} \right)_{\mathbf{R}_0}, \tag{3.1}$$

where $\hat{H}$ denotes a molecular Hamiltonian, $\mathbf{R}_0$ is the equilibrium geometry of the ground state of the neutral picene, and Ψ is a electronic wavefunction of the excited or anionic state at $\mathbf{R}_0$. The vibronic Hamiltonian is written as

$$\hat{H}_{\text{vibro}} = \sum_\alpha \left[\hat{T}(Q_\alpha) + \frac{1}{2}\omega_\alpha^2 Q_\alpha^2 + V_\alpha Q_\alpha \right], \tag{3.2}$$

where $\hat{T}(Q_\alpha)$ denotes kinetic energy operator of a vibration and ω_α vibrational frequency. We employed Becke's hybrid functional (B3LYP) [25] and Perdew and Wang's one with generalized gradient approximation (PW91) [26] with the triple-zeta 6-311+G(d,p) basis set. The geometries were optimized for the neutral ground state. The optimized structures with C_{2v} symmetry were checked with vibrational analysis to be a minimum. The time-dependent density-functional-theory (TD-DFT) is applied for the excited state calculations. We performed analytical force-calculations for the excited and the anionic states to obtain the VCCs. The electronic and vibrational structures as well as the forces were obtained using Gaussian09. [27]. The VCCs are calculated using our codes.

EELS was simulated employing the same method as described in Ref. [18]. We considered thermal excitation at 20K where Roth *et al.* observed the EELS. The calculated excitation energies are 3.7040 and 3.2520 eV, for the B3LYP and PW91 functionals, respectively. The result using the PW91 functional reproduces the experimental excitation energy 3.25 eV well. Using the calculated VCCs, we simulated the EELS. In the simulations, the 0-0 transition is set to 3.24 eV, and the linewidth σ is assumed to be 270

(a) PW91 **(b)** B3LYP

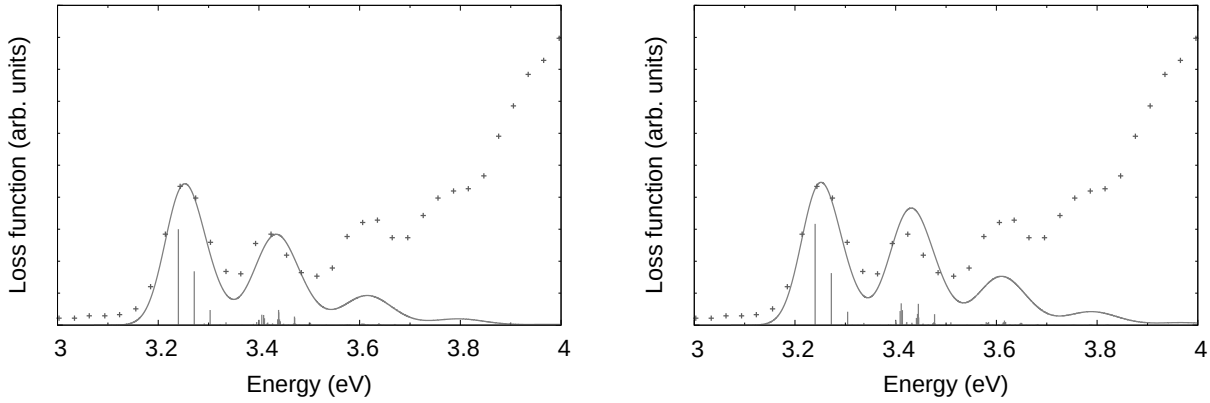

Figure 3.1: Gray lines are simulated electron energy loss spectra (EELS) calculated by (a) the PW91 and (b) the B3LYP functional. Dots indicate the experimental one by Roth *et al.* [5]. The 0-0 transition is set to 3.24 eV. The other parameters employed in the simulations are $T = 20$ K and $\sigma = 270$ cm^{-1}.

cm^{-1} (The FWHM is 39.4 meV). The simulated EELS are shown in Figs. 3.1. The spectrum calculated employing the PW91 functional shows a better fit than that using the B3LYP functional. In the calculation employing the B3LYP, the second strongest vibronic couplings around 1350 cm^{-1} are estimated larger than those in the result using the PW91. Therefore, the relative intensities of EELS in the lower energy are reproduced employing the PW91. [28]. Judging from the calculations of the excitation energies and the simulated spectra, we employ the PW91 functional hereafter for the calculation of the ionic states.

We calculated the VCCs V_α in the monoanion, dianion, and trianion . The authors have calculated orbital vibronic coupling constants (OVCC) of the lowest unoccupied molecular orbitals (LUMO) and next LUMO (NLUMO). Hence we also calculated the OVCCs $V_{i,\alpha}$ from the VCCs V_α for comparison with the ones previously reported. The vibronic Hamiltonian (3.2) is mapped onto a model Hamiltonian. The model Hamiltonian is written as follows:

$$\hat{H}_{\text{vibro}} = \sum_{\alpha,i,\sigma} \hbar\omega_\alpha \left[\hat{b}_\alpha^\dagger \hat{b}_\alpha + \frac{g_{i,\alpha}}{\sqrt{2}} \left(\hat{b}_\alpha^\dagger + \hat{b}_\alpha \right) \hat{c}_{i\sigma}^\dagger \hat{c}_{i\sigma} \right], \tag{3.3}$$

where orbitals i are LUMO (L) and NLUMO (NL), and α runs over all the active a_1 modes. The dimensionless orbital vibronic coupling constant $g_{i,\alpha}$ is defined by $g_{i,\alpha} = V_{i,\alpha}/\sqrt{\hbar\omega_\alpha^3}$.

(a) Monoanion **(b)** Trianion

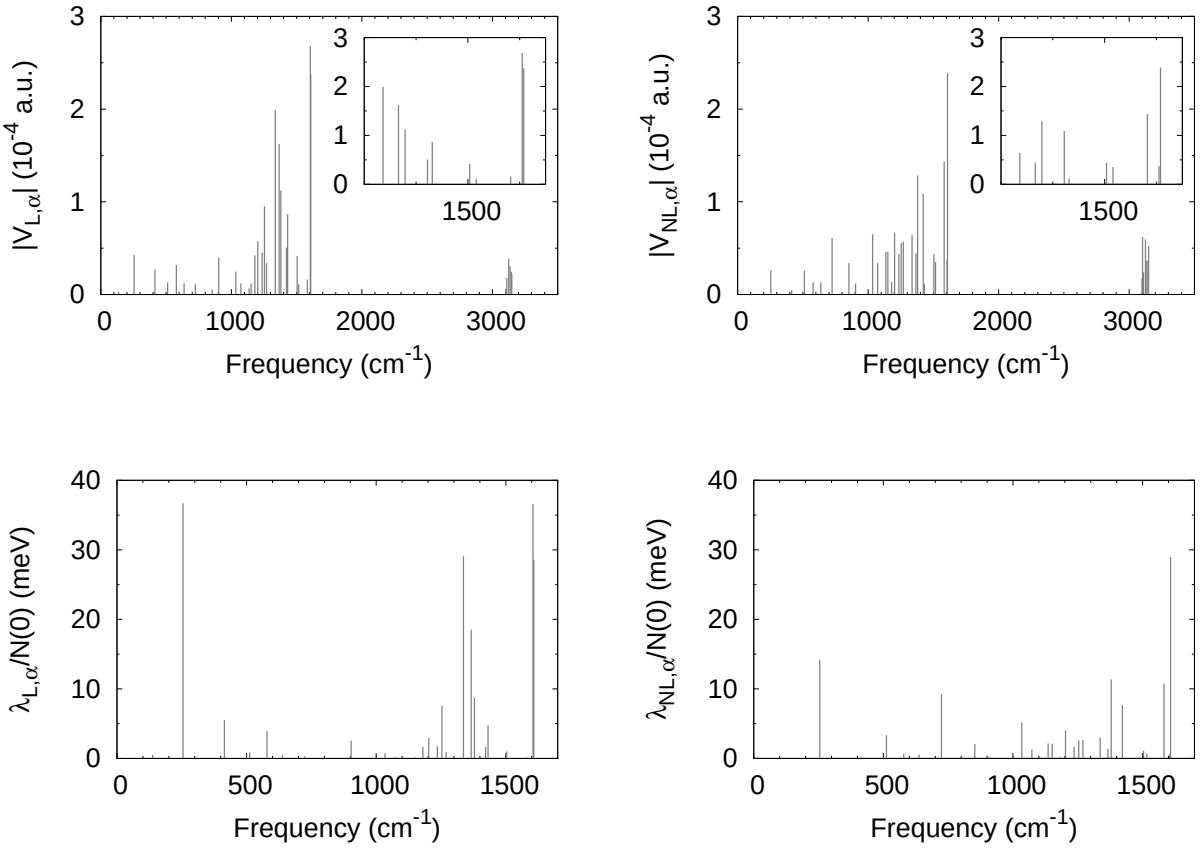

Figure 3.2: Calculated (top) orbital vibronic coupling constants $V_{i,\alpha}$ and (bottom) electron-phonon couplings $\lambda_{i,\alpha}/N(0)$ in the (a) monoanion and the (b) trianion. The subscripts L and NL denote LUMO and NLUMO, respectively. Insets show the orbital vibronic couplings between 1300 to 1650 cm^{-1}.

$\hat{c}^{\dagger}_{i\sigma}(\hat{c}_{i\sigma})$ is the creation (annihilation) operator of orbital i and spin σ, and $\hat{b}^{\dagger}_{\alpha}(\hat{b}_{\alpha})$ is the creation (annihilation) operator of mode α. The OVCCs of LUMO $V_{\mathrm{L},\alpha}$ and NLUMO $V_{\mathrm{NL},\alpha}$ are obtained from the VCCs of monoanion $V_{\mathrm{mono},\alpha}$ and the difference between VCCs of trianion $V_{\mathrm{tri},\alpha}$ and dianion $V_{\mathrm{di},\alpha}$, respectively: $V_{\mathrm{L},\alpha} = V_{\mathrm{mono},\alpha}$ and $V_{\mathrm{NL},\alpha} = V_{\mathrm{tri},\alpha} - V_{\mathrm{di},\alpha}$. It should be noted that the present OVCCs effectively incorporate the contributions from all the occupied orbitals which are important in quantitative arguments [18]. The OVCCs $V_{i,\alpha}$ and intramolecular electron-phonon couplings $\lambda_{i,\alpha}/N(0) = V^2_{i,\alpha}/\omega^2_{\alpha}$ are shown in Figs. 3.2 and tabulated in Tables 3.1 and 3.2. $N(0)$ is the density of states at the Fermi level.

In both the monoanion and trianion, two sets of modes with strong VCCs are observed:

Table 3.1: Vibronic coupling constants in the monoanion $V_{\mathrm{mono},\alpha}$ and the electron-phonon couplings of picene calculated using PW91. They are used as orbital vibronic coupling constants and electron-phonon couplings of LUMO.

Mode	Freq. (cm^{-4})	$V_{\mathrm{mono},\alpha}$ (10^{-4} a.u.)	$\lambda_{\mathrm{L},\alpha}/N(0)$ (meV)	Mode	Freq. (cm^{-4})	$V_{\mathrm{mono},\alpha}$ (10^{-4} a.u.)	$\lambda_{\mathrm{L},\alpha}/N(0)$ (meV)
$a_1(1)$	137.26	-0.027	0.51	$a_1(19)$	1336.39	-1.990	29.07
$a_1(2)$	254.53	-0.426	36.68	$a_1(20)$	1366.13	-1.624	18.52
$a_1(3)$	414.49	-0.269	5.51	$a_1(21)$	1378.84	-1.123	8.69
$a_1(4)$	511.75	-0.131	0.86	$a_1(22)$	1422.08	-0.506	1.66
$a_1(5)$	578.75	-0.318	3.97	$a_1(23)$	1431.36	-0.866	4.80
$a_1(6)$	637.81	-0.121	0.48	$a_1(24)$	1503.69	-0.417	1.01
$a_1(7)$	724.19	-0.109	0.30	$a_1(25)$	1516.13	-0.111	0.07
$a_1(8)$	852.75	-0.055	0.05	$a_1(26)$	1582.56	-0.161	0.14
$a_1(9)$	903.23	-0.397	2.53	$a_1(27)$	1604.85	-2.682	36.61
$a_1(10)$	1033.96	-0.248	0.75	$a_1(28)$	1607.88	-2.374	28.58
$a_1(11)$	1072.59	-0.121	0.17	$a_1(29)$	3098.63	-0.001	0.00
$a_1(12)$	1135.59	-0.066	0.04	$a_1(30)$	3102.42	-0.062	0.01
$a_1(13)$	1151.08	-0.119	0.14	$a_1(31)$	3110.34	-0.179	0.04
$a_1(14)$	1179.90	-0.421	1.67	$a_1(32)$	3125.09	-0.385	0.20
$a_1(15)$	1202.83	-0.575	3.00	$a_1(33)$	3134.88	-0.304	0.12
$a_1(16)$	1235.73	-0.453	1.76	$a_1(34)$	3145.00	-0.246	0.08
$a_1(17)$	1253.59	-0.951	7.55	$a_1(35)$	3148.33	-0.223	0.07
$a_1(18)$	1269.67	-0.337	0.93				

Table 3.2: Orbital vibronic coupling constants $V_{\mathrm{NL},\alpha}$ and electron-phonon couplings $V^2_{\mathrm{NL},\alpha}/\omega^2_\alpha$ of next LUMO (NL) of picene calculated using PW91. The orbital vibronic couplings are calculated from the differences between the vibronic couplings in the trianion and dianion.

Mode	Freq. (cm^{-1})	$V_{\mathrm{NL},\alpha}$ (10^{-4} a.u.)	$\lambda_{\mathrm{NL},\alpha}/N(0)$ (meV)	Mode	Freq. (cm^{-1})	$V_{\mathrm{NL},\alpha}$ (10^{-4} a.u.)	$\lambda_{\mathrm{NL},\alpha}/N(0)$ (meV)
$a_1(1)$	137.26	-0.000	0.00	$a_1(19)$	1336.39	0.641	3.02
$a_1(2)$	254.53	-0.265	14.18	$a_1(20)$	1366.13	-0.444	1.38
$a_1(3)$	414.49	0.049	0.18	$a_1(21)$	1378.84	-1.283	11.34
$a_1(4)$	511.75	-0.258	3.34	$a_1(22)$	1422.08	-1.088	7.68
$a_1(5)$	578.75	-0.131	0.67	$a_1(23)$	1431.36	-0.117	0.09
$a_1(6)$	637.81	0.131	0.55	$a_1(24)$	1503.69	0.436	1.10
$a_1(7)$	724.19	0.608	9.25	$a_1(25)$	1516.13	0.352	0.71
$a_1(8)$	852.75	0.338	2.05	$a_1(26)$	1582.56	-1.435	10.78
$a_1(9)$	903.23	-0.118	0.23	$a_1(27)$	1604.85	0.371	0.70
$a_1(10)$	1033.96	-0.649	5.17	$a_1(28)$	1607.88	2.390	28.95
$a_1(11)$	1072.59	0.339	1.31	$a_1(29)$	3098.63	-0.171	0.04
$a_1(12)$	1135.59	0.460	2.16	$a_1(30)$	3102.42	-0.622	0.53
$a_1(13)$	1151.08	0.462	2.11	$a_1(31)$	3110.34	0.240	0.08
$a_1(14)$	1179.90	-0.134	0.17	$a_1(32)$	3125.09	-0.595	0.47
$a_1(15)$	1202.83	-0.668	4.05	$a_1(33)$	3134.88	-0.367	0.18
$a_1(16)$	1235.73	0.440	1.66	$a_1(34)$	3145.00	-0.359	0.17
$a_1(17)$	1253.59	0.555	2.57	$a_1(35)$	3148.33	-0.522	0.36
$a_1(18)$	1269.67	0.571	2.65				

(1) the maximal coupling modes around 1600 cm^{-1} and (2) the second group of strong modes around 1350 cm^{-1}. This is qualitatively consistent with the calculations by Subedi and Boeri [10,29] . However, in the calculations of Refs. [11,16,17,30], the modes around 1600 cm^{-1} are weak for both the monoanion and trianion. The total electron-phonon couplings $\lambda_{\rm L}/N(0) = \sum_\alpha \lambda_{{\rm L},\alpha}/N(0)$ and $\lambda_{\rm NL}/N(0) = \sum_\alpha \lambda_{{\rm NL},\alpha}/N(0)$ are 196.6 meV and 119.9 meV, respectively. The total coupling of the trianion $\lambda_{\rm NL}/N(0)$ is in line with that of Subedi and Boeri (110 ± 5 meV) [10]. On the other hand, in Ref. [11], $\lambda_{\rm L}/N(0) = 178$ meV and $\lambda_{\rm NL}/N(0) = 206$ meV. They underestimated and overestimated the total couplings for the monoanion and trianion, respectively.

We will discuss the disagreement from view of the electronic and vibrational structures. The calculated VCCs can be rationalized based on the vibronic coupling density. A VCD η_α is defined as

$$\eta_\alpha(\mathbf{r}) = \Delta\rho(\mathbf{r}) \times v_\alpha(\mathbf{r}), \tag{3.4}$$

where $\Delta\rho = \rho(\mathbf{r}) - \rho_0(\mathbf{r})$ is the electron density difference between the electron density of an ionic state ρ and that of a neutral state ρ_0. The potential derivative $v_\alpha(\mathbf{r})$ is the derivative with respect to a mass-weighted normal coordinate Q_α of the potential $u(\mathbf{r})$ acting on one electron at a position $\mathbf{r}$ from all the nuclei. The vibronic coupling constant is equal to the integral of $\eta_\alpha(\mathbf{r})$ over space $\mathbf{r}$:

$$V_\alpha = \int d^3\mathbf{r}\, \eta_\alpha(\mathbf{r}). \tag{3.5}$$

We will concentrate on the $a_1(27)$ mode of the maximal-coupling mode around 1600 cm^{-1} and the $a_1(21)$ mode from the second group around 1350 cm^{-1} because the $a_1(27)$ and $a_1(21)$ modes are close to the mode 5 in Ref. [10] and 21st mode (ν_{21}) in Ref. [11], respectively. Figures 3.3 show the potential derivatives $v_\alpha(\mathbf{r})$ for the $a_1(27)$ and the $a_1(21)$ modes. The distribution of the potential derivative with respect to the $a_1(27)$ mode is located on the armchair-edges of the central three hexagons. On the other hand, that with respect to the $a_1(21)$ mode is on the terminal hexagons.

Fig. 3.4(b) shows the electron density difference of the monoanion. The π density is reflected by the orbital density of the LUMO shown in Fig. 3.4(a). It should be noted that there occurs σ density in the molecular plane with the opposite sign. Such a polarized density originates from the Coulomb interactions between the electron occupied in the LUMO and all σ electrons doubly occupied below the highest occupied molecular orbital

(a) $a_1(27)$ **(1605 cm^{-1})** **(b)** $a_1(21)$ **(1379 cm^{-1})**

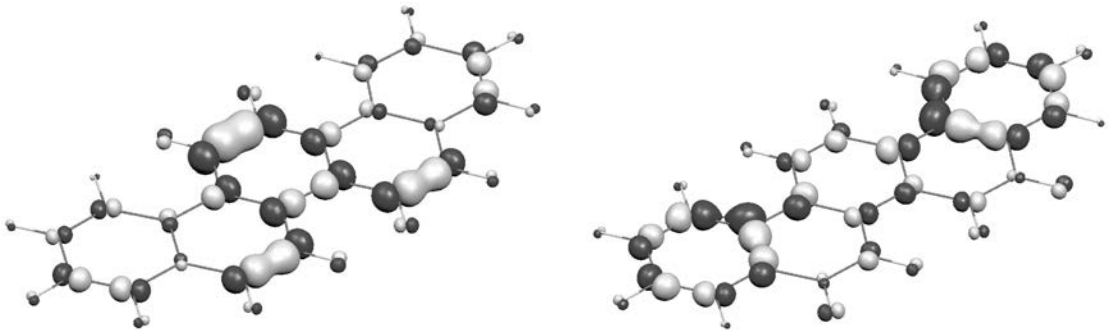

Figure 3.3: Potential derivatives v_α for (a) $a_1(27)$ (1605 cm^{-1}) and (b) $a_1(21)$ (1379 cm^{-1}) modes. Light gray and dark gray areas indicate positive and negative, respectively. The threshold is 1.0×10^{-2} a.u.

(HOMO) [20]. Neglecting such a polarization can give rise to quantitative, or sometimes qualitative, errors in VCC calculations based on the orbital levels [18]. In addition, an electron density difference is usually different from the orbital density of HOMO or LUMO. Many-body effect sometimes plays a crucial role on the electron density difference, and therefore vibronic couplings [24].

Figures 3.5 show the vibronic coupling densities of the monoanion with respect to the $a_1(27)$ and $a_1(21)$ modes. As for the $a_1(27)$, the electron density difference $\Delta\rho(\mathbf{r})$ shows considerable overlap with the potential derivative $v_\alpha(\mathbf{r})$. Accordingly, the VCC of the $a_1(27)$ mode is larger than that of the $a_1(21)$ mode.

The authors have calculated VCCs as the gradients of the orbital levels (orbital gradients) with respect to normal coordinates [16]. We also obtained the orbital gradients of selected modes from the neutral LUMO $\partial\epsilon_{\mathrm{L}}/\partial Q_\alpha$ and from the singly occupied molecular orbital (SOMO) of the monoanion $\partial\epsilon_{\mathrm{S}}/\partial Q_\alpha$ to compare the present VCCs calculated analytically from the total energy gradient as well as numerical gradients. The orbital gradients and the numerical energy gradients were obtained by fitting linear and quadratic polynomials, respectively, in the range from -0.2 a.m.u.$^{1/2}$ a_0 to 0.2 a.m.u.$^{1/2}$ a_0 with a step size 0.05 a.m.u.$^{1/2}$ a_0 where a_0 is the Bohr radius. We summarize the results of the calculations in Table 3.3. All the results indicate that the vibrational modes around 1600 cm^{-1} have the maximal coupling.

Though the gradients of the LUMO level can yield results which are qualitatively consistent with the gradients of the total energy, the results in Refs. [11, 16] are not the

(a) LUMO **(b) $\Delta\rho$**

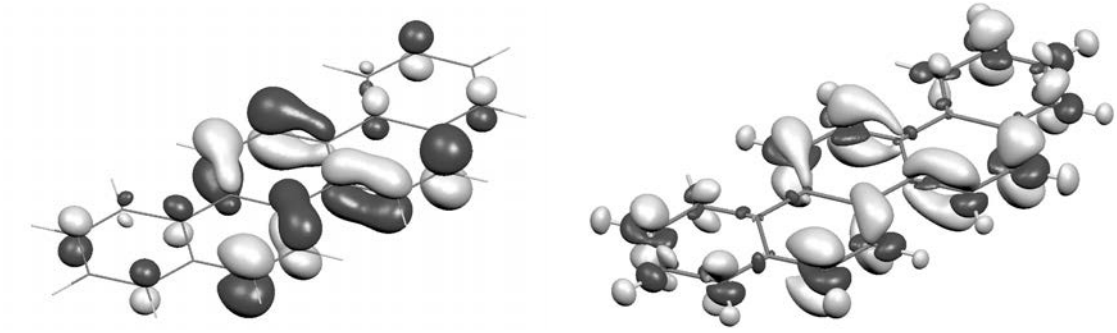

Figure 3.4: (a) Lowest unoccupied molecular orbital (LUMO) and (b)electron density difference $\Delta\rho$ for the monoanion. Light gray and dark gray areas indicate positive and negative, respectively. The threshold is 5.0×10^{-2} a.u. for LUMO and 1.8×10^{-3} a.u. for $\Delta\rho$.

(a) $a_1(27)$ **(1605 cm^{-1})** **(b)** $a_1(21)$ **(1379 cm^{-1})**

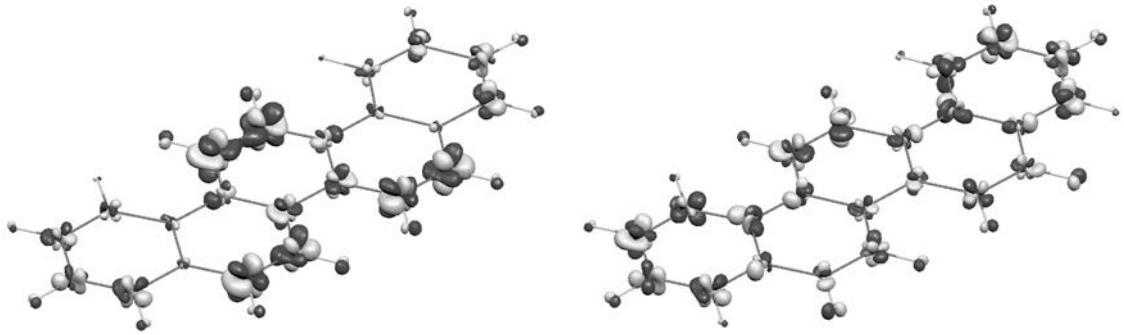

Figure 3.5: Vibronic coupling densities for (a) $a_1(27)$ (1605 cm^{-1}) and (b) $a_1(21)$ (1379 cm^{-1}) modes of the monoanion. Light gray and light gray areas indicate positive and negative, respectively. The threshold is 2.0×10^{-5} a.u.

Table 3.3: Calculated frequencies (cm^{-1}) and orbital gradients $\partial\epsilon/\partial Q$ and total-energy gradients $\partial E/\partial Q$ as vibronic coupling constants (10^{-4} a.u.) for the selected modes of the monoanion. The subscripts L and S denote the neutral LUMO and the SOMO of the anion, respectively.

	Freq.	$\partial\epsilon_{\rm L}/\partial Q$	$\partial\epsilon_{\rm S}/\partial Q$	$\partial E/\partial Q$	
				Num.	Anal.
$a_1(2)$	254.5	0.372	0.475	0.426	0.426
$a_1(19)$	1336.4	2.019	1.889	1.988	1.990
$a_1(20)$	1366.1	1.872	1.365	1.639	1.624
$a_1(21)$	1378.8	0.820	1.335	1.130	1.123
$a_1(27)$	1604.9	3.070	2.281	2.706	2.682
$a_1(28)$	1607.9	2.090	2.580	2.377	2.374

case. In their calculations, the vibrational mode around 1380 cm^{-1} has the maximal coupling, 2.3×10^{-4} a.u. for the monoanion [16]. However, since the $\Delta\rho$ (see Fig.3.4b) is mainly located on the armchair-edges of the central three hexagons, it does not overlap with the potential derivatives of the mode (Fig.3.3b), the VCC of the mode cannot be the maximal. Similar discussion holds for the mode around 1520 cm^{-1} which has the maximal coupling, 2.6×10^{-4} a.u. for the trianion [11].

In summary, we calculated the VCCs of the excited state $^1B_2$, the monoanionic, and the trianionic states of picene from the gradients of the total energies with respect to the normal modes. Employing the VCCs of the excited state, we simulated the EELS. The spectrum agrees well with the experimental one by Roth *et al.* The VCD analysis can provide an insight on the VCCs based on the relations between an electronic and a vibrational structures.

Bibliography

[1] R. Mitsuhashi, Y. Suzuki, Y. Yamanari, H. Mitamura, T. Kambe, N. Ikebe, H. Okamoto, A. Fujiwara, M. Yamaji, N. Kawasaki, Y. Maniwa, and Y. Kubozono, Nature **464**, 76 (2010).

[2] H. Okazaki, T. Wakita, T. Muro, Y. Kaji, X. Lee, H. Mitamura, N. Kawasaki, Y. Kubozono, Y. Yamanari, T. Kambe, T. Kato, M. Hirai, Y. Muraoka, and T. Yokoya, Phys. Rev. B **82**, 195114 (2010).

[3] F. Roth, M. Gatti, P. Cudazzo, M. Grobosch, B. Mahns, B. Büchner, A. Rubio, and M. Knupfer, New. J. Phys. **12**, 103036 (2010).

[4] F. Roth, B. Mahns, B. Büchner, and M. Knupfer, Phys. Rev. B **83**, 144501 (2011).

[5] F. Roth, B. Mahns, B. Büchner, and M. Knupfer, Phys. Rev. B **83**, 165436 (2011).

[6] T. Kosugi, T. Miyake, S. Ishibashi, R. Arita, and H. Aoki, J. Phys. Soc. Jpn. **78**, 113704 (2009).

[7] G. Giovannetti, and M. Capone, Phys. Rev. B **83**, 134508 (2011).

[8] M. Kim, B. I. Min, G. Lee, H. J. Kwon, Y. M. Rhee, and J. H. Shim, Phys. Rev. B **83**, 214510 (2011).

[9] P. L. de Andres, A. Guijarro, and J. A. Vergés, Phys. Rev. B **83**, 245113 (2011).

[10] A. Subedi, and L. Boeri, Phys. Rev. B **84**, 020508(R) (2011).

[11] T. Kato, T. Kambe, and Y. Kubozono, Phys. Rev. Lett. **107**, 077001 (2011).

[12] M. Casula, M. Calandra, G. Profeta, and F. Mauri, Phys. Rev. Lett. **107**, 137006 1 (2011).

[13] Y. Kubozono, H. Mitamura, X. Lee, X. He, Y. Yamanari, Y. Takahashi, Y. Suzuki, Y. Kaji, R. Eguchi, K. Akaike, T. Kambe, H. Okamoto, A. Fujiwara, T. Kato, T. Kosugi, and H. Aoki, Phys. Chem. Chem. Phys. **13**, 16476 (2011).

[14] T. Kosugi, T. Miyake, S. Ishibashi, R. Arita, and H. Aoki, Phys. Rev. B **214506**, 84 (2011).

[15] I. B. Bersuker, and V. Z. Polinger, *Vibronic Interactions in Molecules and Crystals* (Springer–VerlagBerlin and Heidelberg, 1989).

[16] T. Kato, K. Yoshizawa, and K. Hirao, J. Chem. Phys. **116**, 3420 (2002).

[17] T. Kato, and K. Hirao, in *Advances in Quantum Chemistry*, edited by J. R. Sabin, and E. Brändas (Elsevier Academic PressSan Diego, 2003), Vol. 44, p. 257.

[18] N. Iwahara, T. Sato, K. Tanaka, and L. F. Chibotaru, Phys. Rev. B **82**, 245409 (2010).

[19] X. B. Wang, H. K. Woo, and L. S. Wang, J. Chem. Phys. **123**, 051106 (2005).

[20] T. Sato, K. Tokunaga, and K. Tanaka, J. Phys. Chem. A **112**, 758 (2008).

[21] T. Sato, K. Tokunaga, N. Iwahara, K. Shizu, and K. Tanaka, in *The Jahn–Teller Effect: Fundamentals and Implications for Physics and Chemistry*, edited by H. Köppel, D. R. Yarkony, and H. Barentzen (Springer–VerlagBerlin and Heidelberg, 2009), p. 99.

[22] K. Shizu, T. Sato, K. Tanaka, and H. Kaji, Appl. Phys. Lett. **97**, 142111 (2010).

[23] K. Shizu, T. Sato, A. Ito, K. Tanaka, and H. Kaji, J. Mater. Chem. **21**, 6375 (2011).

[24] T. Sato, K. Shizu, K. Uegaito, N. Iwahara, K. Tanaka, and H. Kaji, Chem. Phys. Lett. **507**, 151 (2011).

[25] A. D. Becke, J. Chem. Phys. **98**, 5648 (1993).

[26] J. P. Perdew, J. A. Chevary, S. H. Vosko, K. A. Jackson, M. R. Pederson, D. J. Singh, and C. Fiolhais, Phys. Rev. B **46**, 6671 (1992).

[27] M. J. Frisch, G. W. Trucks, H. B. Schlegel, G. E. Scuseria, M. A. Robb, J. R. Cheeseman, G. Scalmani, V. Barone, B. Mennucci, G. A. Petersson, H. Nakatsuji, M. Caricato, X. Li, H. P. Hratchian, A. F. Izmaylov, J. Bloino, G. Zheng, J. L. Sonnenberg, M. Hada, M. Ehara, K. Toyota, R. Fukuda, J. Hasegawa, M. Ishida, T. Nakajima, Y. Honda, O. Kitao, H. Nakai, T. Vreven, J. J. A. Montgomery, J. E. Peralta, F. Ogliaro, M. Bearpark, J. J. Heyd, E. Brothers, K. N. Kudin, V. N. Staroverov, T. Keith, R. Kobayashi, J. Normand, K. Raghavachari, A. Rendell, J. C. Burant, S. S. Iyengar, J. Tomasi, M. Cossi, N. Rega, J. M. Millam, M. Klene, J. E. Knox, J. B. Cross, V. Bakken, C. Adamo, J. Jaramillo, R. Gomperts, R. E. Stratmann, O. Yazyev, A. J. Austin, R. Cammi, C. Pomelli, J. W. Ochterski, R. L. Martin, K. Morokuma, V. G. Zakrzewski, G. A. Voth, P. Salvador, J. J. Dannenberg, S. Dapprich, A. D. Daniels,

O. Farkas, J. B. Foresman, J. V. Ortiz, J. Cioslowski, and D. J. Fox, *Gaussian 09, Revision B.01*, Wallingford CT, 2010.

[28] The peaks in the higher energy than 3.6 eV include another excitation [5], while we do not consider it in our simulation. Thus the simulated spectrum does not agree with experimental one in the energy range.

[29] Subedi and Boeri calculated the electron-phonon couplings using the density functional perturbation theory [31] within the local density approximation.

[30] Kato *et al.* calculated the electron-phonon couplings from the gradients of orbital level using the B3LYP functional.

[31] S. Baroni, S. de Gironcoli, A. D. Corso, and P. Giannozzi, Rev. Mod. Phys. **73**, 515 (2001).

General Conclusion

In this thesis, the author studied theory of the vibronic couplings in molecules.

Part I dealt with two fundamental problems on the Jahn–Teller effect, that is, the origin of the Jahn–Teller distortion and the isotope effect on the $E \otimes e$ Jahn–Teller system.

In chapter 1 was discussed the origin of the Jahn–Teller distortion of Li_3 and Li_8^+ in terms of the VCD analysis. The VCCs of Li_3 and Li_8^+ were calculated. To explain the vibronic couplings for the Jahn–Teller modes, the VCD analysis was performed. The overlap electron density $\rho_{\gamma\gamma'}$ of Li_8^+ distributes on the atoms and bonds. For the couplings for the t_{2g} modes, $\rho_{\gamma\gamma'}$ on the bonds was proved to contribute significantly. The electron density difference $\Delta\rho$ of Li_8^+ has large distribution on the faces of the cube. The on-face $\Delta\rho$ significantly overlaps the potential derivative v for the e_g mode, and hence the on-face density has a large contribution to the VCC of the e_g mode. The electron density difference $\Delta\rho$ of Li_3 has large distribution on a Li-Li bond. The overlap between the on-bond $\Delta\rho$ and v is important for the vibronic coupling to the e' mode. $\Delta\rho$ and $\rho_{\gamma\gamma'}$ also have symmetric on-site density, while the VCD is almost asymmetric around the atoms. Thus on-site VCDs will not give significant contribution to the VCCs. Present analysis thus clarifies that the Jahn–Teller distortion is not explained based only on the on-site density, while that the on-bonds or on-face densities must be taken into account. The concept of the VCD could be useful for analysis of the vibronic couplings in general Jahn–Teller systems.

In chapter 2 was analyzed the isotope effect on the linear $E \otimes e$ Jahn–Teller system. For this purpose, we employed a triangular molecule X_3 (X = H, D, Li, etc.). Substituting one of the three atoms with the isotope Y, we obtained an isotopomer X_2Y. The isotopic substitution changes the mass in the kinetic energy term, while it does not change the electronic state and potential term. Therefore, the potential energy surface of X_2Y retains the original one-dimensional trough. The isotope effect on the Jahn–Teller system was

analyzed in the strong coupling limit. It was found that the potential energy surface for the pseudorotation is warped due to the change of mass. The potential has two minima and two saddles. The structure of the potential is different from that of the quadratic Jahn–Teller system because the latter has three minima. The vibronic wavefunction is localized around the two minima. Since the change of the kinetic energy term gives rise to the localization, the concentration of the wavefunction ought to be called kinetic localization. We found that the Hamiltonian has a parity symmetry, and hence each vibronic level is doubly degenerate. This parity symmetry is lost by removal of the conical intersection. The dynamic Jahn–Teller Hamiltonian of X_2Y was numerically diagonalized. The distribution of the analytical vibronic wavefunction obtained qualitatively agrees with the numerical one. The DFT calculations were performed to estimate the VCCs of H_3 and Li_3. The VCCs of these molecules are rather strong, which supports the possibility of observation of the kinetic localization.

In part II, the vibronic coupling constants of C_{60}^- were determined and analyzed in terms of the VCD. The VCD of C_{60}^- was used as a chemical reactivity index in the Diels–Alder reaction. Lastly, the VCCs of electron-transporting C_{60} derivatives were calculated and compared with the couplings of C_{60}^-.

In chapter 1 were evaluated the VCCs of C_{60}^- from both the experimental photoelectron spectrum (PES) measured by Wang *et al.* and the DFT calculations. The vibronic states of C_{60}^- were obtained by diagonalizing the linear $T_{1u}\otimes(2a_g\oplus 8h_g)$ Jahn–Teller Hamiltonian. The thermal excitations are further taken into account assuming that each C_{60}^- is in the thermal equilibrium state. For the calculation of the intensities of the PES, the sudden approximation is used. The simulated spectrum at 70 K agrees well with the experimental data. The VCCs for the stretching $h_g(7)$ and $h_g(8)$ modes are strong. On the other hand, the VCCs for the bending $h_g(2)$ mode is weak. Contrary to Gunnarsson's result, the electron-phonon coupling to the $h_g(7)$ as well as the $h_g(8)$ are stronger than that to the $h_g(2)$. The total reorganization energy of the active a_g and h_g modes eventually becomes 74 meV. This stabilization energy is smaller than Gunnarsson's experimental value of 105 meV by 30 %. The DFT calculations were performed to derive the VCCs of C_{60}^-, which agrees well with the present experimental constants. Present theoretical method will give reliable VCCs of alkali-doped fullerides, C_{60} derivatives, and so on.

In chapter 2 was performed the VCD analysis of the vibronic couplings of C_{60}^-. The

electron density difference $\Delta\rho$ is close to the density of the LUMO of a neutral C_{60}. However, negative polarized density is also seen in $\Delta\rho$. This negative density appears due to the Coulomb repulsion between an electron occupying the SOMO and the other electron in the occupied orbitals. The VCD for the bending $h_g(2)$ mode is localized on atoms. Thus the integral of the VCD around the atom is canceled out, and the VCC for the $h_g(2)$ mode is small. On the other hand, the VCD for the stretching $h_g(8)$ mode has density on the both atoms and 6:6 C=C bonds. Although the density on the atoms is canceled out, the delocalized density on the bond contributes to the VCC considerably. In fact, with the use of the LUMO density of a neutral C_{60} to neglect the polarized density, the coupling for the $h_g(8)$ mode is significantly small. In this chapter, a physical explanation on the order of the vibronic couplings in C_{60}^- was given. The physical picture of the vibronic couplings in C_{60}^- is a base to discuss the couplings in other fullerenes, C_{60} complexes, and so on.

In chapter 3, the concept of the VCD was applied to the chemical reactivity index in the Diels–Alder reaction of C_{60}. The VCD of C_{60}^- for the reaction coordinates were calculated. We found that the VCD is similar to that of ethylene monoanion. Therefore, we concluded that C_{60} has ethylene moieties in its cage. Consideration of the degeneracy of the electronic state of C_{60}^- could conclude that there are six ethylene moieties. This result is supported by the existence of the hexakis adduct. It would be possible to use the VCD as a chemical reactivity index.

In chapter 4 were calculated the VCCs of several electron-transporting C_{60} derivatives of organic photovoltaic cells. The theoretical method is the same as that for C_{60}^-. It was found that the VCCs and the reorganization energies of C_{60} and the C_{60} derivatives are close to each other. The VCDs for the effective modes of the C_{60} derivatives are similar to that of C_{60}^-. The electronic structures of the derivatives were analyzed by using the fragment MO analysis (FMO). Although one of the LUMOs of the C_{60} fragment mixes with the orbitals of the substituent group, two of them do not. Therefore, the LUMOs of the derivatives originates from one of the t_{1u} LUMOs of C_{60} which does not mix with the orbitals of the substituent groups. To design the C_{60} derivative with a small reorganization energy, the LUMO should originate from C_{60}.

Part III dealt with miscellaneous applications of the theory of the vibronic couplings to several molecules.

In chapter 1, the initial process of the photoactivation of dispersed V_2O_5/SiO_2 in the excited state was studied. The active species VO_4 has C_{3v} symmetry. The a_2 HOMO and the e LUMO do not have large coefficients on the active center in the ground state. In particular, the a_2 HOMO does not have finite coefficients at the terminal oxygen due to the symmetry. However, the Jahn–Teller distortion occurs in the excited state because the LUMO of the active species is doubly degenerate. Accompanied by the Jahn–Teller distortion, the a_2 HOMO mixes with the e HOMO-1 which has finite coefficients on the terminal oxygen. This mixing occurs due to the off-diagonal orbital vibronic couplings between the HOMO and the HOMO-1. As a result, the HOMO has finite coefficients on the terminal oxygen. A molecular design to control the VCCs could lead to improvement of photocatalysis.

In chapter 2 was studied the relationship between the vibronic couplings and the spin states of the *m*-phenylene diamine derivatives. The ground state of *m*-phenylene diamine dication is triplet. However, the ground state of the *m*-phenylene diamine derivative with a methoxy group is closed-shell singlet. To recover the high-spin state, the vibronic coupling of the singlet state should be reduced. Introducing a biphenyl group, the vibronic coupling in the closed-shell singlet state is in fact reduced, and the high-spin ground state is recovered. Substitution of the biphenyl group reduces the VCD on the *m*-phenylene diamine unit. Moreover, $\Delta\rho$ on the *m*-phenylene diamine is localized and the VCD is canceled out. Present molecular design cannot be performed on the basis of the organic chemistry.

In chapter 3 were calculated the vibronic coupling constants of picene which is the first hydrocarbon superconductor. The experimental EELS of the pristine picene is simulated using the theoretical VCCs developed in this thesis at 20 K. The Franck–Condon approximation was used for calculation of the intensities. The simulated EELS agrees with the experimental one. A similar theoretical method was used to evaluate the VCCs of the mono and trianions of picene. The VCCs of monoanion are the strongest for the C=C stretching mode. Based on the VCD analysis for the monoanion, the electron density difference $\Delta\rho$ and potential derivative v for the stretching mode were clarified to localize around the central three rings. Therefore, $\Delta\rho$ significantly overlaps with v, and the VCC is strong. The insight into the vibronic couplings in picene anions obtained here should be a key to reveal the solid state properties of alkali-doped picene.

In this thesis, we investigated the vibronic couplings in molecules. The vibronic coupling gives a clear picture on the properties of molecules. In addition, in terms of the vibronic coupling density, the vibronic couplings can be controled. Therefore, the concept of the vibronic coupling will enable us to understand and predict new phenomena in molecules and solids. The author hopes that the present thesis will contribute to further development of the theory of the vibronic coupling.